

Selection Map for PV Module Installation Based on Shading Tolerability and Temperature Coefficient

Sandeep Mishra

Selection Map for PV Module Installation Based on Shading Tolerability and Temperature Coefficient

by

Sandeep Mishra

to obtain the degree of Master of Science
at the Delft University of Technology,
to be defended publicly on Wednesday May 09, 2018 at 01:00 PM.

Student number: 4617607
Supervisor: Dr. Olindo Isabella
Dr. Hesam Ziar
Thesis committee: Dr. Miro Zeman, TU Delft
Dr. Olindo Isabella, TU Delft
Dr. Hesam Ziar, TU Delft
Dr. Laura Ramirez Elizondo, TU Delft

This thesis is confidential and cannot be made public until May 08, 2019.

An electronic version of this thesis is available at <http://repository.tudelft.nl/>.

Abstract

Photovoltaic (PV) systems have provided the world with a renewable and environment friendly energy solution. However, PV systems face various loss mechanisms at the module level as well as power electronics level which need to be addressed for further growth of the technology. Power generation from PV modules suffer from heat losses that are a function of the temperature coefficient of maximum power (γ) of the PV module. Another loss mechanism is the shading of PV module where the power output of a module and ultimately the system can be severely compromised. Although various approaches such as bypass diodes and module level power electronics have been employed to minimize the effects of shading on a PV module, so far, the performance of a PV module under shading had only been addressed vaguely and was generally described qualitatively. Therefore, a parameter called Shading Tolerability (ST) was recently developed to quantify the behavior of PV modules under all kinds of shade. However, the observations pertaining to Shading Tolerability were only carried out under Standard Test Conditions (STC). Hence, this thesis aims to investigate whether ST is an innate property of a PV module by formulating a correlation, if there's any, between ST and ambient temperature, classify various PV technologies based on ST and γ and develop a selection map so that an optimal selection of PV modules can be made for the design of PV systems simply by knowing the specifications of the module along with the meteorological conditions of the installation location. Furthermore, different interpolation techniques were evaluated to achieve a comprehensive picture of the meteorological conditions of The Netherlands to determine the most optimal PV technology for The Netherlands using the PV selection map. Finally, Performance Ratios of various existing PV systems were calculated using suitable irradiation decomposition and transposition models as a proof for the validity of the selection map. The obtained results showed that PV systems using CIGS technologies exhibited higher performance ratios on average as was suggested by the selection map.

Acknowledgements

First of all, I would like to thank Dr. Olindo Isabella for providing me with the opportunity to work on this research project. I would also like to thank Dr. Hesan Ziar for his invaluable guidance throughout the course of this thesis. This work would not have been possible without his insights and suggestions. I am indebted to Mr. Jaap Donker from Solar Monkey B.V. for supplying me with data that were crucial for the development of this project as well as for answering numerous of my questions with the utmost of patience. I would also like to extend my deepest gratitude to Mr. Stefaan Heirman for helping me with the logistics of the project.

I consider myself fortunate to have had the direct/indirect support of several individuals especially Pramod Nepal, Andrés Calcabrini, Veikko Schepel, Thomas Loef, Radha Krishnan, Michel Tamarzians and Arogya Koirala. I am also grateful to my institution for providing me with an environment conducive for creative challenges. Lastly, and most importantly, I want to thank my family for their constant support and encouragement throughout my life.

Sandeep Mishra
Delft, The Netherlands
May, 2018

Contents

List of Figures	ix
List of Tables	xi
1 Introduction	1
1.1 Loss mechanisms in PV modules.	2
1.1.1 Temperature loss	2
1.1.2 Transmission loss due to soiling	4
1.1.3 Loss due to partial shading	4
1.2 The shading problem	9
1.3 Thesis motivation and research questions	10
1.4 Thesis outline	10
2 Shading Tolerability	11
2.1 Mathematical modeling of ST	11
2.1.1 Practicality of measurement of ST.	12
2.2 Indoor measurement	13
2.3 Applicability and inference.	15
3 Selection Map for PV Module Installation	17
3.1 Influence of temperature on ST	17
3.2 Experimental validation	18
3.3 Boundaries for temperature class	19
3.4 Selection map	20
4 Interpolation Techniques for Meteorological Data	23
4.1 Meteorological data.	23
4.2 Interpolation of meteorological data.	24
4.2.1 Interpolation techniques	25
4.2.2 Selection of interpolation method	27
4.3 Computational details	28
4.3.1 Calculation of the Sun's altitude.	28
4.4 Meteorological maps of The Netherlands	29
4.4.1 Annual mean daytime temperature	29
4.4.2 Annual mean daytime cloud fraction	30
4.4.3 Annual mean GHI	30
4.5 Spatial cross validation.	31
5 Irradiation Decomposition Models	33
5.1 Solar irradiance	33
5.2 Data process	34
5.3 Decomposition models	35
5.4 BRL model	37
5.5 Assessment of models.	38
5.5.1 Statistical indicators	38
5.5.2 Model comparison	39
6 Validation of Selection Map	45
6.1 Performance parameters	45
6.2 PV systems data description	46
6.3 Modeling of irradiance on a tilted surface.	49
6.3.1 Direct beam component	49

6.3.2	Diffuse component	50
6.3.3	Ground reflected component	52
6.4	Evaluation of PV systems	52
6.5	Coherence of selection map	53
7	Conclusions & Recommendations	55
7.1	Conclusions	55
7.2	Recommendations	56
	Bibliography	57
A	General Equation for Shading Tolerability	63
B	Decomposition Models	65
C	Glossary	67
C.1	Acronyms	67
C.2	List of Symbols	68

List of Figures

1.1	Global cumulative PV installation by 2016.	1
1.2	Influence of temperature on the characteristic curves of a PV cell.	2
1.3	Soiling and accumulation of dust on a PV module.	4
1.4	Partial shading caused by various sources.	5
1.5	I-V and P-V curves for a PV module at different shaded conditions.	5
1.6	Effect on the thermal stability of a PV module due to partial shading.	6
1.7	Schematic diagram for working of bypass diodes.	6
1.8	Reduction in PV module's performance over its lifetime.	7
1.9	Different configurations of bypass diodes.	8
1.10	Overcurrent in overlapped bypass diode configuration.	8
1.11	Example datasheet of a commercial PV module.	9
2.1	Probability distribution function $p(s)$ of shading of PV module for different levels of irradiance i	12
2.2	Change in %ST with increasing c	13
2.3	Experimental setup for indoor measurement of Shading Tolerability.	14
2.4	Suggested boundaries for shading class of PV modules based on %ST.	15
3.1	Influence of temperature on power output at shaded and unshaded scenarios.	18
3.2	Experimental results for measurement of ST at different ambient temperatures.	19
3.3	Percentage share of PV technologies on global PV production in 2016.	20
3.4	Suggested boundaries for temperature class of PV modules based on γ	20
3.5	Selection map for PV module installation based on Shading Tolerability and Temperature Coefficient.	21
4.1	Weather stations used to derive meteorological data.	24
4.2	Example plot for RMSE with different values of β	25
4.3	General map of The Netherlands.	27
4.4	Map for annual average daytime temperature for The Netherlands.	29
4.5	Map for annual average daytime cloud fraction for The Netherlands.	30
4.6	Map for annual average GHI for The Netherlands.	30
4.7	Observed and predicted values of the three different parameters for different weather stations.	31
5.1	The three components of solar irradiance.	33
5.2	Map for meteorological stations maintained by KNMI in The Netherlands.	34
5.3	Clearness index and diffuse fraction based on measured values (CESAR, 2011-2016).	35
5.4	Hourly diffuse fraction modelled as a function of clearness index for different solar elevations using the Skartveit model.	36
5.5	Annual variation of the equation of time (E_t).	38
5.6	Measured data overlaid with results of BRL model for Adelaide, Australia.	38
5.7	Measured and modeled DHI for a week in May 2012.	39
5.8	Clearness index and DHI for summer and winter days in 2012.	40
5.9	Comparison of clearness index and diffuse fraction for different decomposition models.	41
5.10	Model comparison based on %RMSE and CRSS.	42
5.11	Comparison of decomposition models based on %RD.	42
6.1	Location of PV systems.	46
6.2	Decomposed DNI and DHI along with interpolated GHI values.	48

6.3	Skyline profile for the PV system installed in Eindhoven, The Netherlands.	48
6.4	Calculation of hourly \mathbf{SF} for the PV system installed in Eindhoven, The Netherlands. . .	49
6.5	The three components of irradiance on a tilted surface.	49
6.6	Sub-components of diffuse irradiance.	50
6.7	Estimated hourly POA irradiance.	52
6.8	Performance ratio of PV systems.	53
A.1	Demonstration of formulation of ST.	63

List of Tables

2.1	Results for indoor measurements of ST.	16
3.1	Deviation from %ST at 25 °C.	19
4.1	Characteristics of different interpolation techniques.	27
4.2	Cross validation of interpolation results.	32
5.1	List of decomposition models.	36
6.1	Detailed specification along with measured annual AC yield of the PV systems.	47
B.1	List of coefficients for Dutch I model.	66
B.2	List of coefficients for Dutch II model.	66

Introduction

Energy generation has been dominated by fossil fuel based technologies ever since the dawn of industrialization. However, with depleting energy resources as well as the increase in global carbon emissions that pose a major threat to the environment, a need for a shift towards clean and renewable energy sources has been felt. In pursuit of such a shift, renewable energy sources such as solar energy have proved to be vital to attain a sustainable future. Moreover, increase in public awareness has helped remove the barriers to uptake renewable energy and has led to a brisk growth of various sustainable energy technologies.

Continuous innovations and advancements have helped Photovoltaic (PV) technology gain economies of scale and have made them cost competitive and affordable. The prices of PV modules have plummeted by about 80-85% between 2009 and 2016 [1]. This has led to an exponential growth in PV deployment with the global installed capacity reaching 320 GW_p in 2016 [2]. The Levelized Cost Of Electricity (LCOE) for utility scale PV projects declined by 67% between 2010 and 2016 [1]. Moreover, rooftop PV systems have been bringing the benefits for households to not only reduce their electricity costs but also enable them to generate their own electricity.

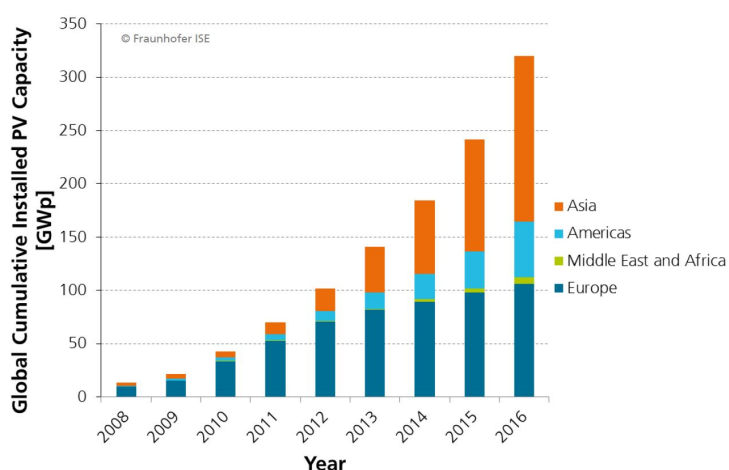


Figure 1.1: Global cumulative PV installation by 2016 [2].

However, in spite of the rapid increase in the application of PV technologies, losses in a PV module remain to be quite significant. Hence, along with further innovations, designers also require as much information as possible regarding the system's components to minimize the losses and achieve the highest possible energy output from a PV system.

1.1. Loss mechanisms in PV modules

The Performance Ratio (PR) of PV systems has increased greatly with time. From 70-80% in the 1990s, performance ratios of about 90% have been achieved in the present time [3]. However, PV modules suffer from reduced performance due to a number of environmental factors such as temperature, transmission losses due to soiling, partial shading, etc. Hence, in order to achieve even greater performance ratios which can lead to quicker energy payback time (EPBT) and energy return on energy invested (EROI), it is essential to address these factors which can be useful for careful design of PV installations [4].

1.1.1. Temperature loss

The influence of temperature on the power output of a PV cell and ultimately its electrical efficiency is well documented. An increase in temperature displaces the I-V and P-V curve and reduces the maximum power. Generally, the effect on the decrease in maximum power is linear and is represented by the Temperature Coefficient for maximum power, γ (%/°C). The temperature dependence of the power output of the PV cell can be discerned from the I-V and P-V curve shown in 1.2.

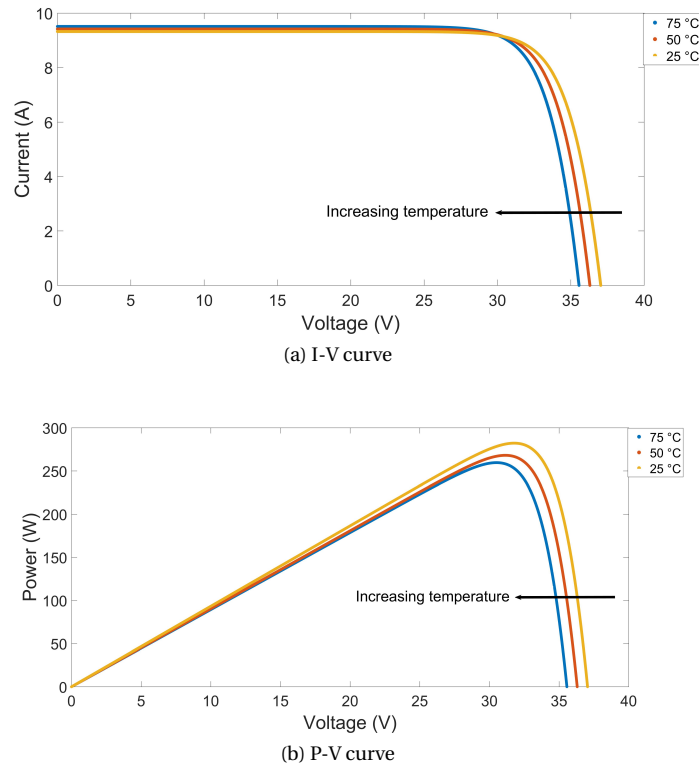


Figure 1.2: Influence of temperature on the characteristic curves of a PV cell.

The reduction in the maximum power of a PV cell due to increase in temperature can be attributed to the effect of temperature on the voltage (V), current (I), and Fill Factor (FF) of the cell as the maximum power is given by,

$$P_{MPP} = V_{MPP} \times I_{MPP} = FF \times V_{OC} \times I_{SC} \quad (1.1)$$

where the subscripts MPP, OC and SC denote Maximum Power Point, Open Circuit and Short Circuit, respectively. About 80-90% of the temperature coefficient of efficiency of PV cells is due to the temperature dependence of the V_{OC} [5]. The V_{OC} of a PV cell decreases linearly with temperature which is largely caused due to the exponential relation of saturation current density (J_0) with temperature as can be seen from the following equations [5, 6].

$$E_{g0} = E_g - T \frac{dE_g}{dT} \quad (1.2)$$

$$J_0 = AT^\zeta \exp\left(-\frac{E_{g0}}{kT}\right) \quad (1.3)$$

$$V_{OC} = \frac{kT}{q} \ln\left(\frac{J_{SC}}{J_0}\right) \quad (1.4)$$

where E_g is the bandgap of the semiconductor at cell temperature T and E_{g0} is the bandgap linearly extrapolated to 0 K. k is the Boltzmann constant and is approximately equal to 1.381×10^{-23} J/K whereas q is equal to one elementary charge i.e. 1.602×10^{-19} C. The parameter ζ includes the temperature dependence of various conditions such as the total available states in the conduction and valence bands, carrier mobility and lifetime [7].

The short-circuit current density (J_{SC}) of a PV cell generally increases with temperature albeit slightly. This is because the semiconductor bandgap decreases as the temperature rises resulting to more electron-hole pairs that can be photogenerated [7]. However, the scant increase in short-circuit current is totally overshadowed by the reduction in open-circuit voltage leading to an overall effect of linear reduction in the maximum achievable power output of the PV cell. This leads to a reduced fill factor as well as cell efficiency.

The characteristic of a PV cell or a PV module with respect to temperature is defined by its temperature coefficients. The temperature coefficient of a certain parameter can be easily estimated as,

$$\alpha(STC) = \frac{I_{SC}(T_M, G_{STC}) - I_{SC}(STC)}{T_M - T_{STC}} \quad (1.5)$$

$$\beta(STC) = \frac{V_{OC}(T_M, G_{STC}) - V_{OC}(STC)}{T_M - T_{STC}} \quad (1.6)$$

$$\gamma(STC) = \frac{P_{MPP}(T_M, G_{STC}) - P_{MPP}(STC)}{T_M - T_{STC}} \quad (1.7)$$

where α (mA/°C), β (V/°C) and γ (W/°C) are the temperature coefficients of short-circuit current, open-circuit voltage and maximum power, respectively. Generally, they are expressed as the percentage of the respective individual parameter with the unit %/°C. T_M is the temperature of the PV module and T_{STC} is equal to 25 °C. G_{STC} is the incident irradiance at STC and is equal to 1000 W/m².

Applying the concepts explained above to equations 1.5-1.7, it can be easily comprehended that β and γ are negative entities while α is positive. High voltage PV modules such as thin films generally exhibit lower β (less negative) than crystalline silicon PV modules since it decreases as V_{OC} increases which can be seen below [7].

$$\beta = -\frac{\frac{E_{g0}}{q} - V_{OC} + \zeta \frac{kT}{q}}{T} \quad (1.8)$$

Moreover, the temperature coefficient for efficiency ($\delta\eta/\delta T$) can be obtained by [6],

$$\eta(T_M, G_{STC}) = \frac{P_{MPP}(T_M, G_{STC})}{G_{STC} \times A_M} \quad (1.9)$$

$$\frac{\delta\eta}{\delta T} = \frac{\eta(T_M, G_{STC}) - \eta(STC)}{T_M - 25^\circ\text{C}} \quad (1.10)$$

where A_M is the area of the PV module.

It can be perceived that the performance of a PV module is significantly affected by temperature and therefore, it is essential to know the characteristic parameters regarding the influence of temperature on a PV module's performance. Hence, the temperature coefficients for short-circuit current (α), open-circuit voltage (β) and maximum power (γ) are normally listed in a PV module's datasheet which makes it easier to compare the thermal behavior of different PV modules while designing a PV system.

1.1.2. Transmission loss due to soiling

Although less acknowledged, soiling reduces the power production of a PV module significantly. It acts as a barrier for effective irradiance received by the module. The deposition of dust, soil, and micro fibers resulting from the surroundings as well as minute pollens like growth of bacteria, fungi, etc. contributes towards the soiling of a PV module. Any particulate matter below $500\ \mu\text{m}$ is termed as a dust and it is estimated to be about the size of an optical fibre used in communication purposes or a size which is 10 times a human hair [8].

The deposition of dust on a PV module majorly depends on two conditions [9],

- Location of the PV module.
- The local outdoor conditions.

The location could be residential, rural, and industrial which directly relates with the natural accumulation of atmospheric particles (aerosols) in the PV module. The major dust types which significantly degrades the PV power production are ash, calcium, limestone, soil, sand and silica [10]. The estimated loss in irradiance and power is defined with the help of Soiling Ratio (SR) as [11],

$$T_{loss} = 1 - SR_{Isc} = 1 - \frac{G_2}{G_1} = 1 - \frac{I_{SC,S}}{I_{SC,C}} \quad (1.11)$$

The Soiling Ratio is the ratio of incident irradiance of the soiled module (G_2) to the clean module (G_1) or short circuit current generated from the soiled module ($I_{SC,S}$) to the clean module ($I_{SC,C}$). However, the value of SR may vary depending on the type of soiling i.e. uniform or non-uniform soiling. Generally, the loss due to non-uniform soiling is more profound than that due to uniform soiling of the PV module with the same amount of dust. The accumulation of dust on the PV module may occur due to inadequate rainfall, wind or dew where strong wind conditions mainly result to non-uniformities in soiling patterns [12]. As we move further away from the equator, PV modules need to be installed with a certain tilt angle to receive maximum amount of sunlight. However, due to the tilt of the module, dust particles are carried to the bottom edge of the PV module and are trapped near the frame or are accumulated in patches.

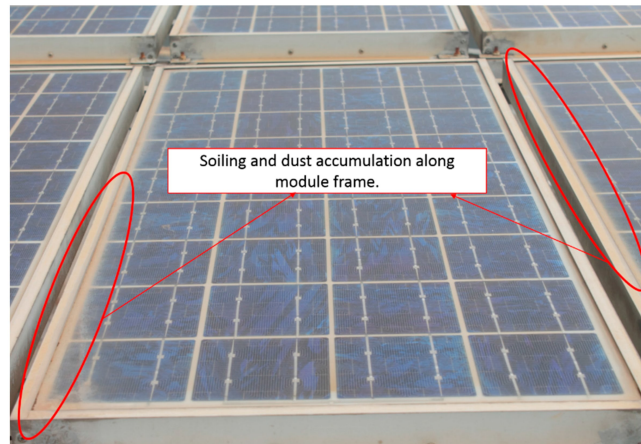


Figure 1.3: Soiling and accumulation of dust on a PV module [13].

1.1.3. Loss due to partial shading

PV cells generate a small amount of voltage (slightly more than 0.5V) and current (several Amperes) when illuminated with standard solar irradiance. Therefore, several PV cells are interconnected, normally in series among many other configurations, and encapsulated to form a PV module. PV cells in a PV module have identical electrical characteristics. However, since PV cells are essentially current sources, mismatch of these cells can occur if they are exposed to non-uniform irradiance. Hence, shading of a certain part of the PV module compared to another, known as partial shading, is a major source of electrical mismatch. This mismatch could lead to a number of consequences that are described below.

Shading of a PV module can be divided into static and dynamic shading. Static sources such as tree shadow, shadow from surrounding buildings, snow or bird droppings can cause static shading. Dynamic shading is more common in large PV parks where moving clouds cause differences in irradiance between adjacent PV modules. The change in irradiance could be over 300 W/m^2 over a short time of about 0.1 seconds during irradiance transition [14]. Moreover, PV modules installed in Building Integrated PV (BIPV) systems with different orientations are prone to receiving dissimilar amount of irradiance creating a situation similar to partial shading [15]. Likewise, flexible PV modules installed on curved surfaces are susceptible to non-uniform irradiance incident over the entire module resulting in electrical mismatch.

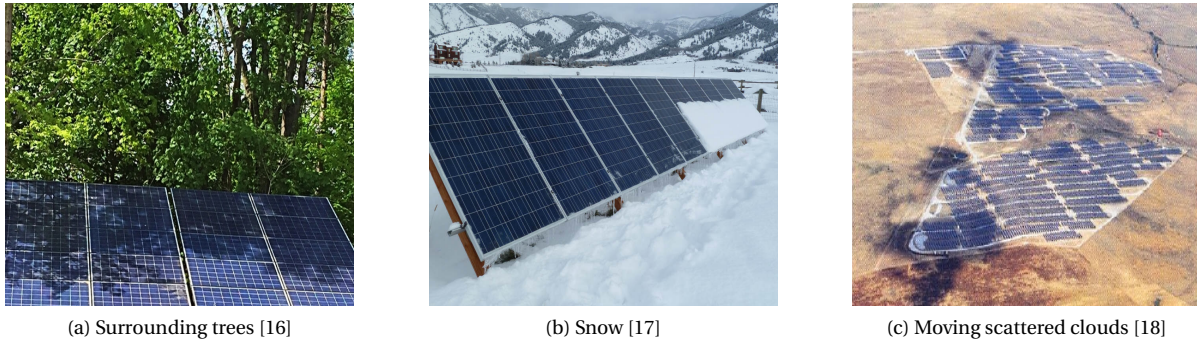
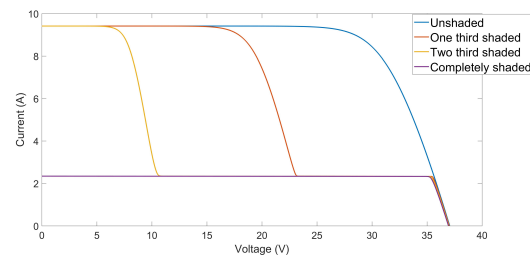


Figure 1.4: Partial shading caused by various sources.

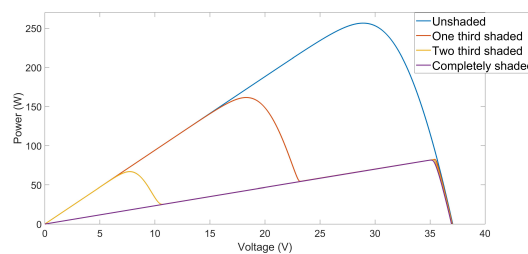
Partial shading can severely compromise the performance of a PV module and ultimately the system efficiency. Some of the major effects of partial shading are described below:

a) Non-optimal power output:

As mentioned earlier, the cells in a PV module are normally connected in series. When a single cell in the PV module is shaded, the current generated by it is significantly reduced. Thus, the current flowing throughout the module is limited by the shaded cell due to the series connection. This results to a notable reduction in the power output of the PV module. Figure 1.5 shows the I-V and P-V curve for a 60 cell poly c-Si module under different conditions of shading of the PV cell array. It should be noted that the following result was obtained with a shading object that transmitted 25% of the incident irradiance.



(a) I-V curve



(b) P-V curve

Figure 1.5: I-V and P-V curves for a PV module at different shaded conditions.

Bypass diodes are therefore integrated in a PV module to augment its performance under shading. Commercial series-connected 60 or 72 cell crystalline silicon modules have three bypass diodes with each connected to one third of the solar cell array. Normally, for these PV module, the power lost when a single cell is shaded is equal to one third of the PV module's maximum power output [19].

b) Hotspot and thermal instability:

When a cell in a PV module is shaded, all the rest of the series connected unshaded cells are compelled to carry the lower current generated by the shaded cell. Thus, the unshaded cells are forced to produce high voltages acting as a reverse bias source whereas the shaded cell acts as a load consuming the power generated from the unshaded cells. This results to dissipation of energy from the unshaded cell leading to high temperatures that ultimately results to formation of hotspots in the PV module [6]. The temperature can rise to dangerously high levels that may crack the encapsulant material or even damage the PV module irreversibly [20].

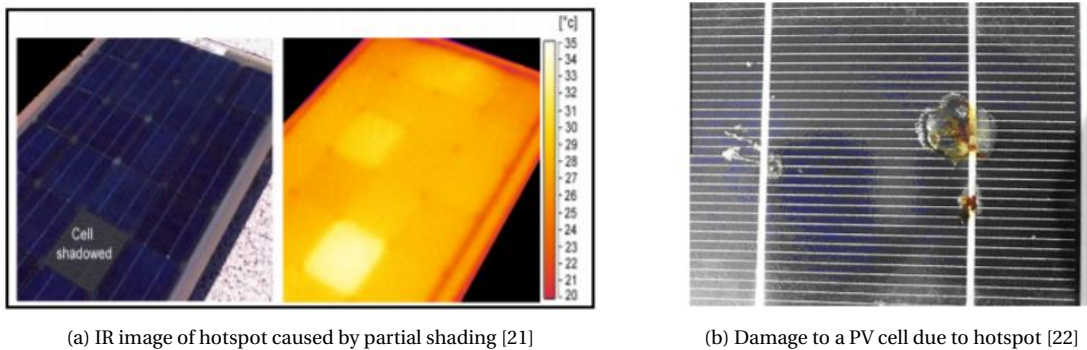
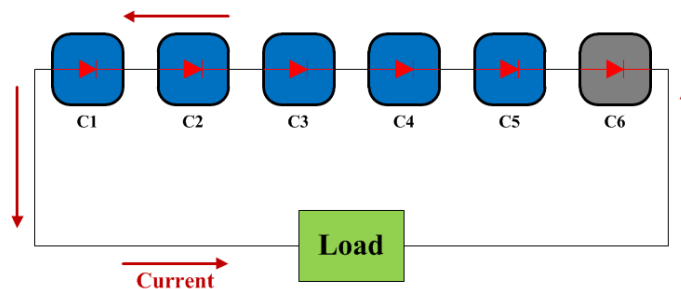
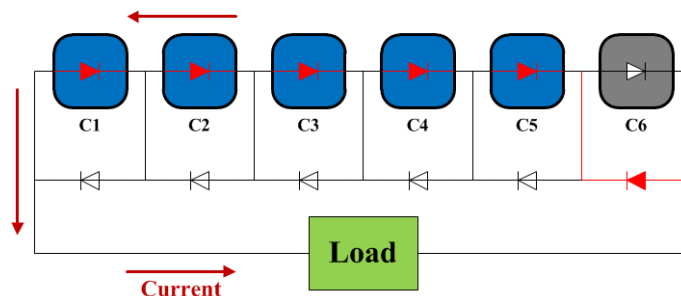


Figure 1.6: Effect on the thermal stability of a PV module due to partial shading.

Therefore, to prevent the localized overheating of the shaded cell, bypass diodes are included in a PV module. Bypass diodes conduct current only when under positive voltage. A simple illustration of the working of bypass diodes in a PV module is shown in the figure below.



(a) String of six PV cells with one cell shaded



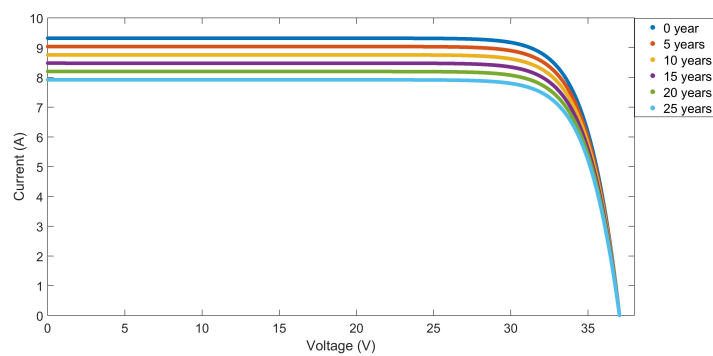
(b) String of six PV cells with one cell shaded including bypass diodes

Figure 1.7: Schematic diagram for working of bypass diodes.

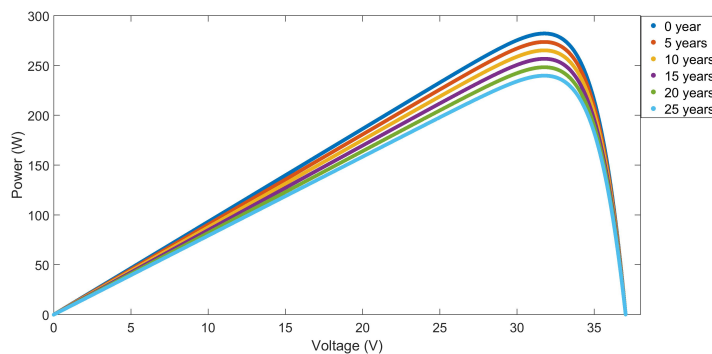
As illustrated in figure 1.7, considering a string of six PV cells in series where five of the cells receive uniform irradiance whereas the sixth cell is shaded, it can be clearly observed that the shaded cell limits the current through the circuit in the first case. However, when a bypass diode is connected in parallel with each cell, the diode passes the current due to the biasing of other cells when a cell is shaded as shown in figure 1.7(b). Hence, the current in the module is no longer restricted by the shaded cell thereby reducing thermal overload and formation of hotspots.

c) Ageing:

The efficiency of a PV module declines with time. However, as discussed earlier, partial shading can lead to formation of hotspots in a PV module which can lead to extremely high temperatures in the module. Therefore, continuous exposure of a PV module to partial shading, especially for ones without bypass diode or in case of diode failure, can induce quicker ageing of the PV module. It was found that the reverse bias voltage contributes the most to power loss from partial shade [23]. Especially, cells conducting current at -15V reverse bias suffer with rapid decline in the maximum power at STC leading to reduced daily energy yield [23]. Moreover, monolithic thin film modules are extremely vulnerable to partial shade. Even a partial shade event of about 20 seconds can reduce the maximum power of these modules by up to 14% [24].



(a) I-V curve



(b) P-V curve

Figure 1.8: Reduction in PV module's performance over its lifetime.

The decline in performance of a PV module with time can be seen in the I-V and P-V curve presented in figure 1.8. Crystalline silicon PV modules may suffer from continuous degradation of up to 0.7% per annum [25]. There are a number of factors that contribute to the degradation in continuous operation such as cracking of encapsulant material, discoloration, delamination, splitting of back-sheets, junction box failure and wiring degradation [25]. This deterioration of the PV module over time can further be accelerated and worsened by partial shading.

d) Overcurrent or nuisance trip:

The performance of PV modules under partial shading depends on the arrangement of the bypass diodes. Usually, there are two different configurations of bypass diodes in a PV module, namely, overlapped and non-overlapped configurations. These configurations are shown in the figure 1.9,

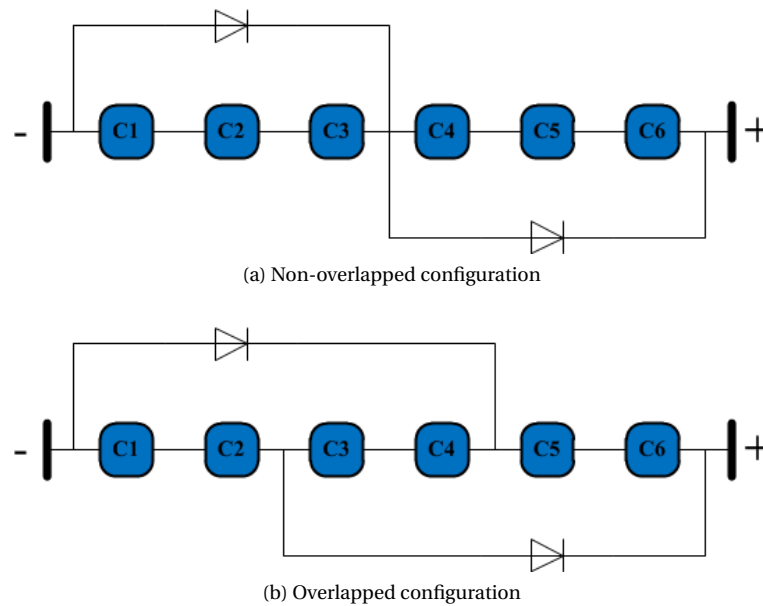


Figure 1.9: Different configurations of bypass diodes.

The overlapped configuration of bypass diode is not that common in commercial PV modules. Nevertheless, PV modules using such layout of bypass diodes are known to produce overcurrent at certain shading profiles [26]. The reason for the occurrence of such overcurrent is that at certain shading conditions, the configuration of bypass diodes provides an alternative path for the current to flow. Figure 1.10 presents a schematic illustration of the overcurrent phenomenon.

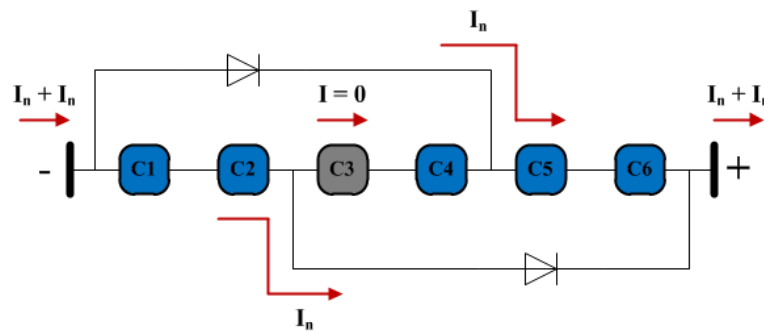


Figure 1.10: Overcurrent in overlapped bypass diode configuration.

Here, when the cell C3 is shaded, there is no current produced by it. The rest of the cells receive uniform irradiance and generate nominal current. As a result, both of the bypass diodes begin to conduct. Therefore, the current from the unshaded cells flows into the external circuit resulting to an output current that is twice than the nominal current of each PV cell. Thus, it can be concluded that overcurrent occurs whenever shading of only the overlapped cells (C3 and C4) takes place [26]. Such large amount of current can lead to the system suffer from nuisance tripping.

1.2. The shading problem

In the previous section, the detrimental effects of partial shading on PV modules was discussed. However, as the PV industry has been attaining its unprecedented growth, PV modules are being installed progressively around the world. Increasing efficiency, reducing costs along with better aesthetics and greater flexibility has made it possible to employ PV technologies not only in rooftops and large PV parks but also in novel applications such as BIPV, solar roads, etc. [27, 28]. On the other hand, it also means that PV systems are further vulnerable to shading as it is almost impossible to remove sources for dynamic shading as well as obstacles that lead to static shading. Therefore, it is of utmost importance to investigate the shading tolerance of a PV module to extract the maximum possible output from it.

Since the dawn of Photovoltaic technology, several researches have tried to address the problem of partial shading and have suggested methods to limit the impact of it. *Rauschenbach* exhibited that the module performance under shading can be significantly improved by shunting each row of parallel cells with a silicon p-n or Schottky bypass diode [29]. This has been heavily utilized in the PV industry today. *Feldman et al.* suggested that a substantially higher average output power can be achieved by electrically distributing the impact of a shade using quasi-random cell interconnection scheme [30]. Instead of commercial PV modules, this approach has been applied in satellite applications where its cost-benefit ratio is lower [30]. PV systems also make use of DC-DC power optimizers integrated with every PV module that enable the inverter to maintain a constant string voltage regardless of the individual module performance [31]. Furthermore, several other approaches such as cell-integrated bypass diode, Cool Bypass Switch (CBS), IntegraBus technology, etc. have been investigated to tackle the problem of shading [32–34].

As can be understood from above, PV modules come up with different mechanisms to cope with shading. Hence, different modules behave differently when shaded depending on the technology, cell interconnection as well as the mechanism adopted. However, when it comes to selecting a suitable PV module for a PV system design, especially for locations that are prone to shading, not much information about the module's ability to withstand shading can be found. The unpredictability of shading profiles on PV systems makes it difficult to quantify a PV module's shading tolerability. Generally, datasheets of PV modules include the number of bypass diodes used along with subjective statements such as "*shade tolerant*", "*superior shading behavior*", "*excellent performance even when partially shaded*", "*excellent shade and debris tolerance*", etc. [35–38].

UNISOLAR
PowerBond ePVL

TECHNICAL DATA SHEET
ePVL 144 | 136 | 68

It Pays To Be Flexible
Building on 25 years of solar experience, the new, enhanced version of our proven efficiency, packing density and ease of installation, resulting in a lower cost of elect.

Key Attributes

- Lightweight and flexible
- Roof-friendly solution requiring no penetrations
- BIPV & BAPV
- Superior performance at high temperatures
- Excellent performance even when partially shaded
- Built-in strain relief reduces installation labor and improves reliability
- Polarized, latching connectors
- Lead-free RoHS compliant design

Performance Characteristics

Rated Power (P _{max}):	144, 136 or 68 Wp
Tolerance of P _{max} :	±5 %

Mechanical Characteristics

- Junction Box: IP66 terminal housing with integrated strain relief
- Connectors: Protected, weatherproof latching connectors with 4 mm² (12 AWG) halogen-free cables
- Bypass Diodes: Connected across every solar cell
- Front Surface: Durable ETFE high light transmittance polymer
- Adhesive: Peel and stick pressure sensitive adhesive (PSA)
- Cell Type: Multijunction amorphous silicon solar cells 256 mm x 239 mm (14" x 9.4")

Certifications and Warranty

- UL 1703 Listed by Underwriters Laboratories® for electrical and fire safety (Class A Max. Slope 2/12, Class B Max. Slope 3/12, Class C Unlimited Slope fire ratings) for use in systems up to 600 VDC
- IEC 61840 and IEC 61730 certified by TÜV Rheinland for use in Class A PV systems up to 1000 VDC
- CEC Listing
- 5-Year Limited Product Warranty
- Limited Power Output Warranty: 92% at 10 years, 84% at 20 years, 80% at 25 years (of minimum power)

Application Criteria*
Suitable for installation on clean, dry approved substrates (refer to uni-solar.com for full details) at ambient temperatures above 10°C

Roof Requirements
Maximum slope of 60°
Install in areas free of water pooling

Refer to UniSolar's installation manual for further application criteria.

Global Contact Information

World Headquarters	European Headquarters	German Sales Office	Italian Sales Office
Albion Hills, MA USA info@uni-solar.com +1 248 200 0440	Paris, France france@uni-solar.com +33 1 74 70 49 24	Milano espresso@uni-solar.com +39 02 240 40 400	Varese italy@uni-solar.com +39 045 8920982

EN60335-1-21

Lightweight
Flexible
No Penetrations
Shade Tolerant
Durable
Easy to Install

Figure 1.11: Example datasheet of a commercial PV module [37].

Therefore, a glaring need for a parameter that classifies PV modules on the basis of their tolerance to shading has been felt. To address this issue, *Ziar et al.* have introduced a quantifiable parameter called Shading Tolerability (ST) based on probability laws that can prove to be more meaningful to PV system designers [39]. A detailed description of this parameter is presented in chapter 2.

1.3. Thesis motivation and research questions

This thesis is motivated by the fact that in spite of PV systems being influenced by a number of environmental factors, while designing a PV system, designers generally have a trove of data regarding the location's climatic conditions, dust intensity, temperature dependence of a PV module's output, etc. but are often provided with no information related to a PV module's ability to cope with shading. General qualitative statements do not help to properly compare different PV modules. The parameter Shading Tolerability (ST) instigated by *Ziar et al.* to characterize a PV module's shading property is a convincing approach to quantify the behavior at shading scenarios. Therefore, the main goal of this thesis is to introduce a map that may help designers to make an optimal choice based on the meteorological conditions, thermal behavior of a PV module and Shading Tolerability by answering the following research questions:

1. Is the parameter Shading Tolerability an intrinsic property of a PV module?
2. Can PV modules be categorized for certain climatic conditions based on their Shading Tolerability and temperature coefficient for maximum power (γ)?
3. Among the existing interpolation techniques, which is the best suited method to get detailed information of the meteorological conditions of The Netherlands?
4. What are the most suitable irradiance decomposition and transposition models to accurately calculate the Plane of Array (POA) irradiance for The Netherlands?
5. Does the established selection map help improve the energy yield and performance ratio of a PV system?

1.4. Thesis outline

This thesis comprises of seven chapters where the proposed research questions will be answered in chapters 3-6. Chapter 7 provides the conclusion based on the results obtained. A brief description of each chapter can be found below:

Chapter 2 - Shading Tolerability: This chapter provides an in-depth explanation of the parameter Shading Tolerability (ST) along with the results for indoor measurement of PV modules for ST.

Chapter 3 - Selection map for PV module installation: In this chapter, the influence of temperature on ST is investigated. The findings are utilized to introduce a preliminary selection map based on the results obtained for ST, technical specifications of the PV module along with meteorological conditions.

Chapter 4 - Interpolation techniques for meteorological data: In this chapter, literature study about different existing interpolation techniques for meteorological data is presented. Finally, a visual map of The Netherlands for temperature, cloud fraction and Global Horizontal Irradiance (GHI) is presented using the most suitable model. These maps are then used to determine the optimal PV technology for The Netherlands based on the selection map.

Chapter 5 - Irradiation Decomposition Models: This chapter deals with the evaluation of commonly used decomposition models to determine the most accurate method for decomposing irradiation components for The Netherlands.

Chapter 6 - Validation of Selection Map: In this chapter, corroboration of the selection map with the performance ratio of several PV systems installed in The Netherlands is carried out using a suitable irradiation transposition model.

Chapter 7 - Conclusion and Recommendations: Answers to the research questions posed above is summarized based on the results of the above mentioned chapters. Finally, recommendations for future work is presented.

2

Shading Tolerability

Shading Tolerability (ST) is a probabilistic analysis of the behavior of a PV module at shading. It is the mathematical expectation of power production of the PV module under all possible scenarios of shading [39]. Hence, ST provides designers with a number which makes it easier to interpret and distinguish the performance of different PV modules under shading and helps make an optimum selection based on the conditions of the installation location. For an instance, for a shade prone location, a higher value of ST for a given PV module can influence designers to select that module. The following sections offer a deeper insight into the parameter ST where we look into the mathematical modeling of the parameter followed by experimental validation of the model.

2.1. Mathematical modeling of ST

To perform a probability analysis, it is important to create a sample space that includes all possible occurring events. However, there are infinite profiles for a PV module to be shaded which leads to an infinitely large sample space. Therefore, two major assumptions are made to simplify the analysis [39]:

- Every cell of the PV module is uniformly irradiated and the value for the incident irradiance is between 0 - 1000 W/m². The probability of occurrence for all the values of irradiance is equal.
- Similarly, the probability of shading of each cell of the PV module is equal. It is not a function of the position of the cells in the PV module or that of the PV module in an array.

Thus, the total number of shading profiles for a PV module would be i^c where i is the possible levels of irradiance and c is the total number of cells. It should be noted that since there are infinite levels of irradiance between 0 - 1000 W/m², the probability of occurrence of each shading profile is $\lim_{x \rightarrow \infty} (1/i^c)$.

Now, for a random variable x that has a probability of occurrence of $p(x)$, the expected value of x is given by [40],

$$E(x) = \sum_k^{\infty} x_k p(x_k) \quad (2.1)$$

Hence, using equation 2.1, the ST of a PV module can be expressed as [39],

$$ST_{(i,c)} = \frac{1}{P_{MPP}} \sum_{k=1}^{i^c} P_k \left(\frac{1}{i^c} \right) \quad (2.2)$$

where $ST_{(i,c)}$ is the Shading Tolerability of the PV module, c is the total number of cells and i is the levels of irradiance. P_k (W) represents the MPP of the PV module at each shading profile whereas P_{MPP} (W) is the maximum power of the PV module. Here, P_{MPP} enables us to compare PV Modules with different power ratings by normalizing the value of mathematical expectation.

2.1.1. Practicality of measurement of ST

It can be seen that ST is not practically measurable from equation 2.2 as $i \rightarrow \infty$. However, according to Ziar *et al.*, the value of ST for $i = 2$ can be used instead of ST for $i \rightarrow \infty$ [39]. This can be explained using the general equation for $ST_{(i,c)}$ as shown below.

$$ST_{(i,c)} = \left(\frac{m}{c}\right) \left(\frac{1}{i^n}\right) \left[\sum_{k=1}^j \binom{n}{j} k + \sum_{a=1}^{j-1} n \left(\frac{j-a}{j}\right) \sum_{b=1}^{n-1} \binom{n}{b} a^{n-b} \right] \quad (2.3)$$

where n is the number of PV cells connected in series, m is the number of cell strings in a module and therefore, $c = n \times m$. The term j is equal to $(i-1)$. Equation 2.3 is derived by obtaining $ST_{(i=2,c)}$, $ST_{(i=3,c)}$ and continuing the procedure to obtain $ST_{(i,c)}$. A detailed description of the derivation can be found in Appendix A.

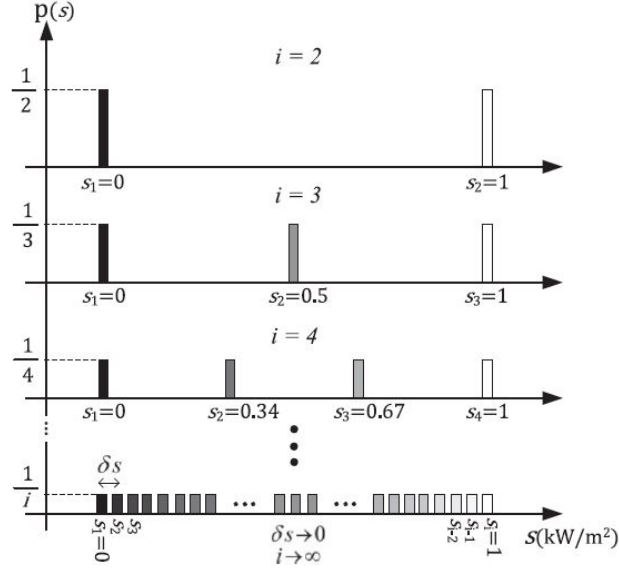


Figure 2.1: Probability distribution function $p(s)$ of shading of PV module for different levels of irradiance i [39].

In equation 2.3, the first term of the series stands for the condition of uniform irradiance of all the PV cells whereas the second term corresponds to shading profiles where the irradiance on the cells is not the same. It can also be observed that the number of strings of PV cells (m) does not influence the ST of a PV module. Moreover, as $i \rightarrow \infty$, equation 2.3 converges to $1/(n+1)$. Therefore, it can be deduced that the ST of a module is inversely proportional to a factor of $(n+1)$.

If we substitute $i = 2$ in equation 2.3, we get,

$$ST_{(i=2,c)} = \left(\frac{1}{2^n}\right) \quad (2.4)$$

From equations 2.3 and 2.4, it can be easily seen that, for two different PV modules, if $ST_{(i=2,c)_1} > ST_{(i=2,c)_2}$ then $n_1 < n_2$ which ultimately results to $ST_{(i \rightarrow \infty, c)_1} > ST_{(i \rightarrow \infty, c)_2}$. Thus, as mentioned above, ST can be measured for $i = 2$ and used instead of ST for $i \rightarrow \infty$.

However, it needs to be investigated further whether testing PV modules for ST at $i = 2$ in a laboratory stands correct for real-time outdoor conditions where $i \rightarrow \infty$. This is due to the fact that PV modules are designed with various approaches to withstand shading such as bypass diodes, power optimizers, etc. that ameliorate the performance of the PV module at shading [31, 41]. Hence, to model the approach adopted by the manufacturer, a coefficient $\lambda_{(i,c)}$ is established. λ is a function of i and c and the general equation of ST of a PV module can again be written as [39],

$$ST_{(i \rightarrow \infty, c)} = \lambda_{(i \rightarrow \infty, c)} \left(\frac{1}{n+1}\right) \quad (2.5)$$

It is not in the scope of this thesis to develop a mathematical model for λ since there are various approaches that manufacturers adopt to cope with shading. However, *Ziar et al.* have defined the boundaries for $\lambda_{(i,c)}$ [39]. The minimum value for $\lambda_{(i,c)}$ is 1 which implies that the adopted approach does not affect the PV module's ST at all. The maximum value for $\lambda_{(i,c)}$ would insist that the shaded cells do not restrict the performance of the unshaded cells and that the PV module's output would be the sum of each cell's individual generation.

From figure 2.1, it can be seen that at any uniform probability function, for a single cell, the maximum value for $ST_{(i \rightarrow \infty, c)}$ is $(1/2)$ as the average incident irradiance on a cell is 500 W/m^2 . For an instance, when $i = 3$, the maximum value of ST for a single cell can be found as, $ST_{(i=3, c=1)} = (1/P_{cell}) \times (1/3^1) \times (0 + 0.5 + 1) \times (P_{cell}) = 0.5$. Therefore, the boundaries of $\lambda_{(i,c)}$ can be defined by substituting $ST_{(i \rightarrow \infty, c)} = 1/2$ in equation 2.5 as,

$$1 \leq \lambda_{(i \rightarrow \infty, c)} \leq \frac{n+1}{2} \quad (2.6)$$

Since the mathematical model for λ is not readily available, *Ziar et al.* have investigated the use of the condition of $i = 2$ instead of $i \rightarrow \infty$ experimentally [39]. It was found that the ranking of PV modules based on the measurements of ST in a laboratory ($i = 2$) was the same as the ranking of the modules based on their Performance Ratio (PR) under real-time outdoor conditions ($i \rightarrow \infty$) [39]. Therefore, it can be concluded that the value of $ST_{(i=2, c)}$ can be used instead of $ST_{(i \rightarrow \infty, c)}$. The following section presents a brief description of the measurement of ST at indoor conditions.

2.2. Indoor measurement

The purpose of indoor measurement of ST is to extract $ST_{(i=2, c)}$ for different PV modules. The results obtained can be used as an indicator of the PV module's performance under shading and rank them. A wide range of PV modules of different technologies, number of cells and bypass diodes were tested. During this experiment, the value of c was fixed at 6 which means that the active area of the PV module was divided into 6 equal parts. Surely, a higher value of c would lead to more accurate results. However, as can be seen from figure 2.2, the change in the value of $\%ST$ gets smaller with increase in c and would converge to be negligible after a certain value. The curve for a crystalline silicon module is hyperbolic whereas that for a CIGS module oscillates about a value where increasing c has a dampening effect on it. Furthermore, increasing the value of c would also mean that the number of measurements, and ultimately the measurement time, required for every single PV module would be higher as it increases exponentially with c (number of measurements = 2^c). Therefore, to limit the measurement time to a reasonable number for industrial purposes as well as achieve a rational level of accuracy, the value of c as six was found to be the best fit. Moreover, since six is an even number, it is straightforward to divide the module's length and width into sections of three times two.

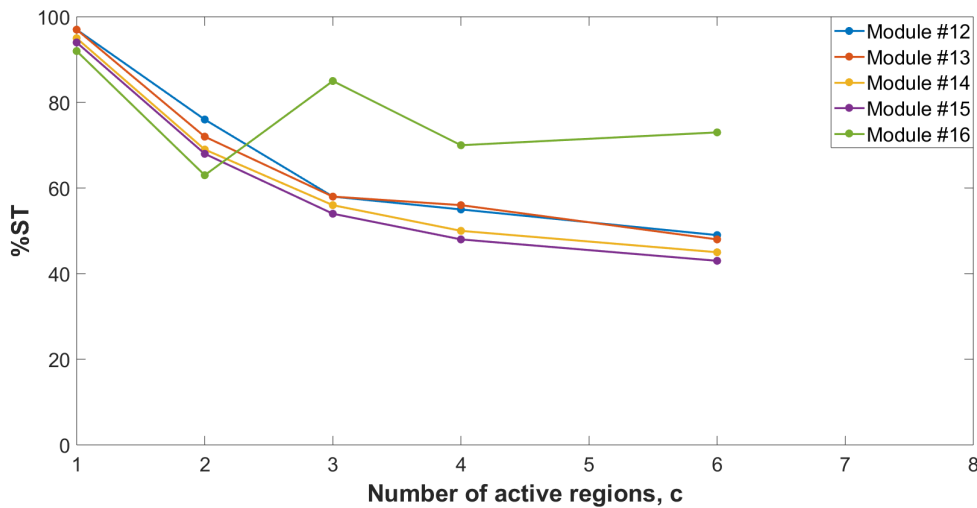


Figure 2.2: Change in $\%ST$ with increasing c . The module numbers refer to the serial number of PV modules presented in Table 2.1.

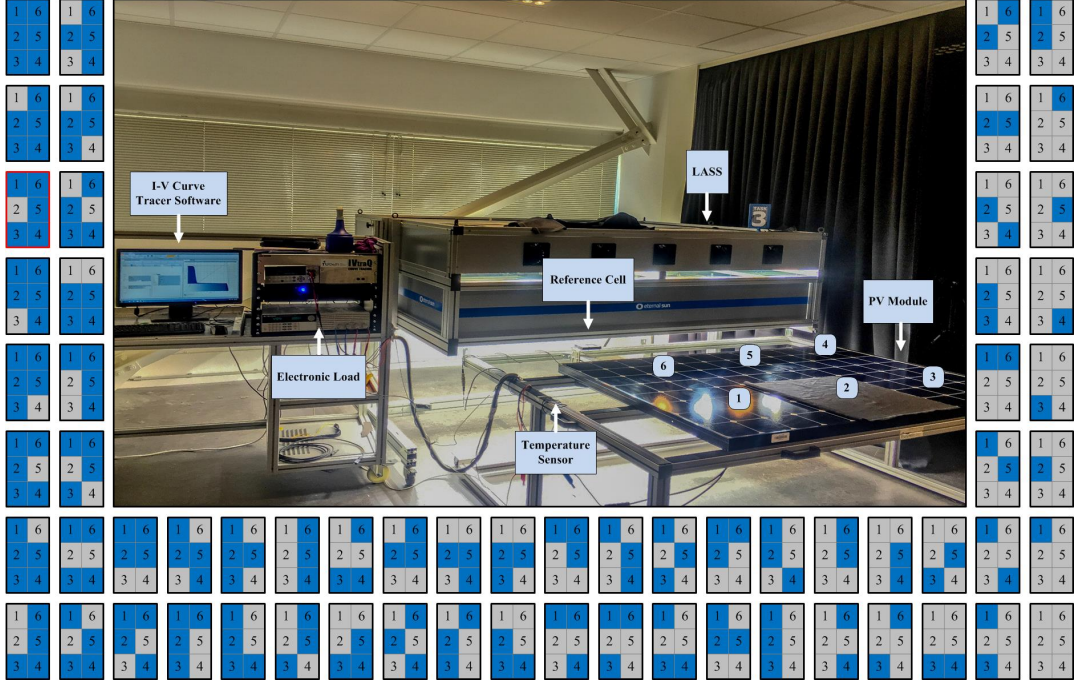


Figure 2.3: Experimental setup for indoor measurement of Shading Tolerability including 64 different shading profiles from 000000 to 111111. The profile shown in the image is 010000 and is marked in red.

As shown in figure 2.3, 64 (2^6) different shading profiles were applied to the PV modules at 1000 W/m^2 , AM 1.5 and 25°C , and their I - V characteristics were measured using an EternalSun Large Area Steady State Solar Simulator (LASS). It should be noted that 25°C is not the temperature of the PV module but instead the ambient temperature. This is due to the fact that there are formations of hotspots in a PV module during shading which would lead to non-uniform temperature distribution in the module. Therefore, keeping the module temperature fixed would lead to inaccuracies. Furthermore, this experiment tends to emulate shadows in real conditions and since, they are not perfectly dark, the shading object was chosen such that it would transmit 25% of the incident irradiance. Hence, the unshaded cells receive 1000 W/m^2 whereas the shaded cells receive 250 W/m^2 . Ziar *et al.* have stated that the average time for the measurement of each PV module was 5.73h whereas the average time for testing the PV modules during this thesis was 4.18h [39].

Table 2.1 presents the results obtained for PV modules tested during this thesis as well as that carried out by Ziar *et al.* in the Photovoltaics Lab at TU Delft. The parameter $\%ST$ was calculated using equation 2.7,

$$\%ST = \left(\frac{ST}{ST_{max}} \right) \times 100\% \quad (2.7)$$

It should be noted that, here, the maximum value of ST (ST_{max}) is 0.625 instead of 0.5 since the simulated shade is not perfectly dark as the shading object passes 25% of the incident irradiance.

$$ST_{max} = 0.5 + \frac{I_{SO}}{2} \quad (2.8)$$

where I_{SO} is the percentage of irradiance transmitted by the shading object. Furthermore, based on the results obtained for $\%ST$, three shading classes/symbols; sunny ($\%ST < 50\%$), partly cloudy ($50\% \leq \%ST < 80\%$) and cloudy ($\%ST \geq 80\%$) were introduced using Linear Support Vector Machine (LSVM) algorithm. As can be seen from figure 2.4, the calculated hyperplanes have been re-positioned slightly to achieve more effective boundaries that can be useful for industrial application.

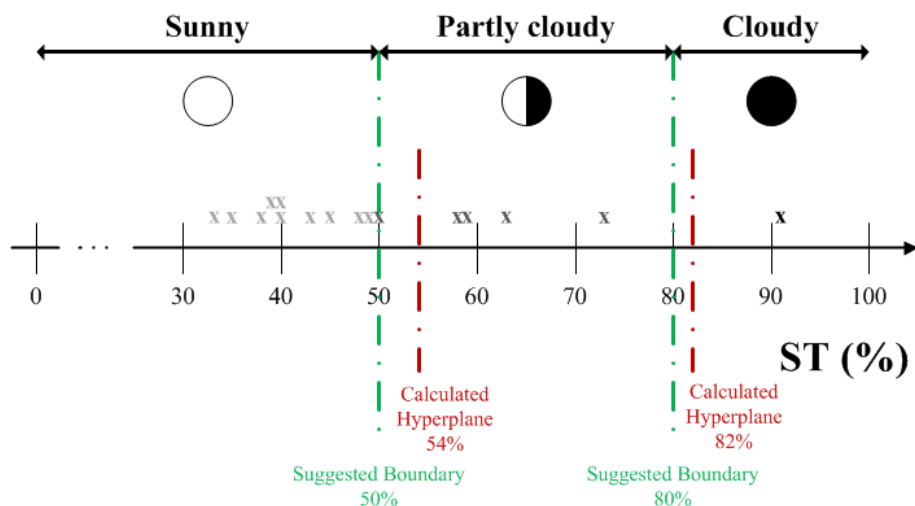


Figure 2.4: Suggested boundaries for shading class of PV modules based on %ST.

The boundaries introduced above describe the suitability of a PV module for a given climatic condition based on its shade tolerance. From a marketing point of view, these values can be translated to the specific symbol for PV modules datasheet, indicating optimal usage of a certain PV module technology for different climate. Thus, it is an essential aspect for the selection of PV modules since designers can make decisions solely by knowing the ST of a PV module and the climatic conditions of the installation location. Therefore, the proposed boundaries will be an important feature of our selection map.

2.3. Applicability and inference

From the results obtained, it can be concluded that the performance of a PV module can be signified by the measurable parameter ST which can be used as a benchmark to rate PV modules. Moreover, as presented in Table 2.1, it can be clearly discerned that thin film modules generally fare better than crystalline silicon modules at shading. Furthermore, it is also worth pointing out that a greater number of bypass diodes used in a PV module does not necessarily signify that the module performs better at shading. Module #3 and #5 perform better than module #10 and #11 even though the latter modules make use of one bypass diode per cell. Hence, instead of the number or type of bypass diodes employed in a PV module, ST gives a better picture of the module's performance under shading and therefore, can be defined as a valid standard to distinguish and compare PV modules.

This provides a meaningful step towards the characterization of PV modules based on their performance under shading and shall be used in the following chapters to conceptualize a preliminary selection map for PV modules. However, it is yet to be seen whether ST is a characteristic parameter of a PV module or a varying entity. A thorough analysis of it is presented in the next chapter where the influence of external conditions on ST along with the selection map is presented.

Table 2.1: Results for indoor measurements of ST along with elaborate specification of the tested PV modules. ST and %ST values were rounded to the closest integer.

S.No.	PV module	Technology	Electrical specification	γ (%/°C)	Mechanical size, weight and flexibility	Notes on module's datasheet regarding shade tolerance	ST	%ST	Suggested shade class/symbol
1	Neste Module PV A12	a-Si	MPP = 7.5 W $V_{OC} = 22.5$ V, $I_{SC} = 0.6$ A $V_{MPP} = 15$ V, $I_{MPP} = 0.5$ A Bypass Diodes: None 29 cells (29 × 1)	-0.20	614 × 309 × 22 mm ³ 3.0 kg Rigid	None	0.36	58%	Partly cloudy 
2	Victron Energy SPM30-12	Mono c-Si	MPP = 30 W $V_{OC} = 22.5$ V, $I_{SC} = 2$ A $V_{MPP} = 18$ V, $I_{MPP} = 1.67$ A Bypass Diodes: One 36 cells (36 × 1)	-0.48	450 × 540 × 25 mm ³ 2.5 kg Rigid	None	0.24	38%	Sunny 
3	Würth Solar GeneCIS module 80W	CIS	MPP = 80 W $V_{OC} = 44$ V, $I_{SC} = 2.5$ A $V_{MPP} = 35$ V, $I_{MPP} = 2.29$ A Bypass Diodes: One 132 cells (66 × 2)	-0.36	605 × 1205 × 35 mm ³ 12.7 kg Rigid	<i>Optimum energy yield through outstanding temperature and low light behavior.</i>	0.57	91%	Cloudy 
4	Scheuten Multisol P6-54 series 200	Poly c-Si	MPP = 200 W $V_{OC} = 33$ V, $I_{SC} = 8.22$ A $V_{MPP} = 25.9$ V, $I_{MPP} = 7.71$ A Bypass Diodes: Three 54 cells (54 × 1)	-0.48	1500 × 1000 × 42 mm ³ 20.0 kg Rigid	<i>Junction box with patented connection system and 3 bypass diodes.</i>	0.22	35%	Sunny 
5	Calyxo Thin film solar module	CdTe/CdS	MPP = 77.5 W $V_{OC} = 59.6$ V, $I_{SC} = 2.16$ $V_{MPP} = 43.0$ V, $I_{MPP} = 1.83$ A Bypass Diodes: None 156 cells (78 × 2)	-0.25	1200 × 600 × 6.9 mm ³ 12.0 kg Rigid	None	0.39	63%	Partly cloudy 
6	SunPower SPR X20 327-BLK	Mono c-Si	MPP = 327 W $V_{OC} = 67.6$ V, $I_{SC} = 6.07$ A $V_{MPP} = 57.3$ V, $I_{MPP} = 5.71$ A Bypass Diodes: Three 96 cells (96 × 1)	-0.29	1559 × 1046 × 46 mm ³ 18.6 kg Rigid	<i>Designed to deliver the most energy in partial shade and hot rooftop temperatures.</i>	0.21	33%	Sunny 
7	Masdar PV MPV-T	Tandem a-Si/a-Si	MPP = 109.81 W $V_{OC} = 137.54$ V, $I_{SC} = 1.21$ A $V_{MPP} = 107.03$ V, $I_{MPP} = 1.02$ A Bypass Diodes: One 636 cells (212 × 3)	-0.30	1300 × 1100 × 7 mm ³ 29.5 kg Rigid	<i>Excellent energy output even during diffuse or low light conditions.</i>	0.25	40%	Sunny 
8	IKS Photovoltaik STA14 10W SolarTrainer	Poly c-Si	MPP = 10 W $V_{OC} = 22$ V, $I_{SC} = 0.72$ A $V_{MPP} = 17$ V, $I_{MPP} = 0.52$ A Bypass Diodes: One 36 cells (36 × 1)	-0.50	345 × 294 × 23 mm ³ Unspecified Rigid	None	0.25	40%	Sunny 
9	Solland SunWeb module 235W _p	Poly c-Si	MPP = 235 W $V_{OC} = 36.97$ V, $I_{SC} = 8.44$ A $V_{MPP} = 30.05$ V, $I_{MPP} = 7.82$ A Bypass Diodes: Three 60 cells (60 × 1)	-0.43	1613 × 984 × 35 mm ³ 22.0 kg Rigid	None	0.24	39%	Sunny 
10	Hanergy PowerFlex 90W	CIGS	MPP = 90 W $V_{OC} = 22$ V, $I_{SC} = 6.3$ A $V_{MPP} = 16.5$ V, $I_{MPP} = 5.4$ A Bypass Diodes: Thirty seven 36 cells (36 × 1)	-0.43	2017 × 494 × 3 mm ³ 1.8 kg Flexible	<i>Shade tolerant.</i>	0.31	50%	Partly cloudy 
11	Uni-Solar PowerBond ePVL	Multi-junction a-Si	MPP = 27.4 W $V_{OC} = 10.44$ V, $I_{SC} = 4.28$ A $V_{MPP} = 7.8$ V, $I_{MPP} = 3.52$ A Bypass Diodes: Five 5 cells (5 × 1)	-0.20	1325 × 373 × 3 mm ³ 1.8 kg Flexible	<i>Excellent performance even when partially shaded.</i>	0.37	59%	Partly cloudy 
12	BenQ SunForte PM096B00-335	Mono c-Si	MPP = 335 W $V_{OC} = 64.9$ V, $I_{SC} = 6.62$ A $V_{MPP} = 54.7$ V, $I_{MPP} = 6.13$ A Bypass Diodes: Three 96 cells (96 × 1)	-0.33	1559 × 1046 × 46 mm ³ 18.6 kg Rigid	None	0.30	49%	Sunny 
13	AERspire Deluxe 60	Mono c-Si	MPP = 250 W $V_{OC} = 38.3$ V, $I_{SC} = 8.62$ A $V_{MPP} = 30.8$ V, $I_{MPP} = 8.08$ A Bypass Diodes: Three 60 cells (60 × 1)	-0.41	1720 × 1035 × 8 mm ³ 24.0 kg Rigid	None	0.30	48%	Sunny 
14	BISOL Premium Series BMU-260	Poly c-Si	MPP = 260 W $V_{OC} = 39.0$ V, $I_{SC} = 8.90$ A $V_{MPP} = 30.9$ V, $I_{MPP} = 8.40$ A Bypass Diodes: Three 60 cells (60 × 1)	-0.35	1649 × 991 × 40 mm ³ 18.5 kg Rigid	<i>High efficiency at low irradiation.</i>	0.28	45%	Sunny 
15	JA Solar JAM6-60-270 (BK)	Mono c-Si	MPP = 270 W $V_{OC} = 38.46$ V, $I_{SC} = 9.09$ A $V_{MPP} = 31.33$ V, $I_{MPP} = 8.62$ A Bypass Diodes: Three 60 cells (60 × 1)	-0.41	1650 × 991 × 40 mm ³ 18.2 kg Rigid	None	0.27	43%	Sunny 
16	Solar Frontier SF170-S	CIS	MPP = 170 W $V_{OC} = 112$ V, $I_{SC} = 2.20$ A $V_{MPP} = 87.5$ V, $I_{MPP} = 1.95$ A Bypass Diodes: One 170 cells (170 × 1)	-0.31	1257 × 977 × 35 mm ³ 20.0 kg Rigid	<i>Efficiency reduction of maximum power from an irradiance of 1000 W/m² to 200 W/m² at 25°C is typically 2.0%.</i>	0.46	73%	Partly cloudy 

3

Selection Map for PV Module Installation

As discussed previously, energy yield of a PV system is impacted by several environmental factors of which temperature and shading are of dominant importance. Therefore, this chapter presents a selection map based on the two parameters, γ and ST , that determine the PV module's output with respect to temperature and shading. But first, it is necessary to investigate whether ST of a PV module is a constant entity or not. A detailed analysis of it is presented below.

3.1. Influence of temperature on ST

Any variable that defines the behavior of a certain entity can be called as its characteristic property. For a PV module, the rated power (P_{max}), open-circuit voltage (V_{OC}), short-circuit current (I_{SC}) along with its temperature coefficients (α , β and γ) are its characteristic parameters. These parameters describe the characteristic trait of a PV module. Similarly, since the ST of a PV module represents its behavior at shading, it could also be a characteristic property of a PV module. This section aims to investigate whether the ST of a PV module is a constant value or if it is influenced by external condition such as ambient temperature.

In the previous chapter, we observed that the ST of a PV module is a direct function of its power output at different shading conditions. However, it is a well established fact that the output of a PV module is sensitive to the temperature of the PV module. As explained in section 1.1.1, the output of a PV module is influenced negatively by the module temperature. Re-arranging equation 1.7, the power output of a PV module at higher module temperature can be written as,

$$P_{MPP}(T_M, G_{STC}) = P_{MPP}(STC)(1 + \gamma(T_M - T_{STC})) \quad (3.1)$$

where γ is in $\%/^{\circ}C$. Assuming that the temperature coefficient for maximum power does not vary even when the module is partially shaded, the effect of the module temperature on its ST can be understood by inserting the expression for power at higher module temperature in equation 2.2 as,

$$ST_{(i,c)}(T_M, G_{STC}) = \frac{1}{P_{MPP}(STC)(1 + \gamma(T_M - T_{STC}))} \sum_{k=1}^{i^c} P_k(1 + \gamma(T_M - T_{STC})) \left(\frac{1}{i^c} \right) \quad (3.2)$$

It can be seen that the term containing the temperature coefficient in the numerator and the denominator cancels out resulting to,

$$ST_{(i,c)}(T_M, G_{STC}) = \frac{1}{P_{MPP}} \sum_{k=1}^{i^c} P_k \left(\frac{1}{i^c} \right) \quad (3.3)$$

which is the same as equation 2.2. Therefore, ideally, the ST of a PV module is not a function of the module temperature. However, this cannot be said in reality since the temperature of the module is not uniform during partial shading which makes it quite difficult to fix the module temperature to a certain value during the measurement of ST . Furthermore, at higher temperatures and under shaded condition, PV modules might not behave according to the temperature coefficient for power specified in their datasheet.

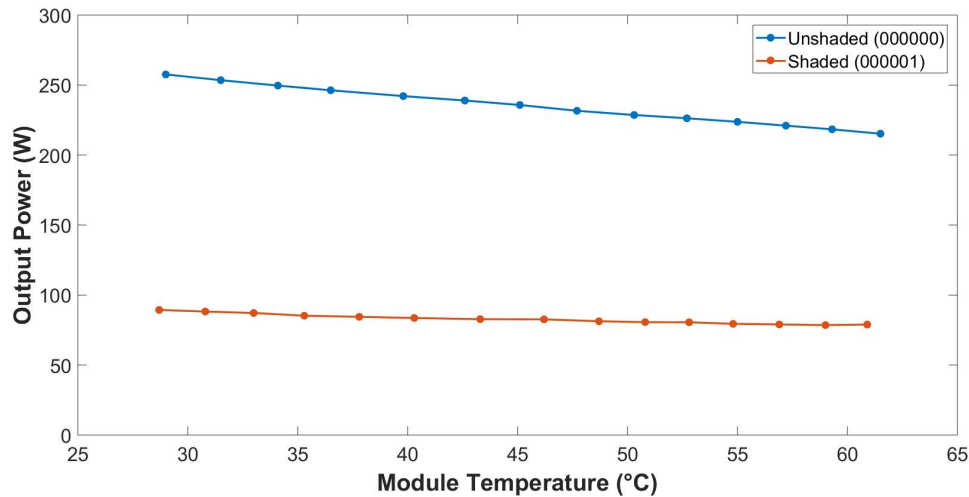


Figure 3.1: Influence of temperature on power output at shaded and unshaded scenarios. The above result pertains to module #14 from Table 2.1.

Here, the module was kept under the LASS for ~ 5 minutes and I-V measurements were carried out repetitively as the module was heated. The module temperature was measured by attaching the DTU6022 at disc USB Positive Temperature Coefficient (PTC) temperature sensor by QTI Sensing Solutions at the middle of the backsheet of the module. Although it is not possible to accurately determine the module temperature during partial shading, from the above figure, it can be observed that as the PV module heats up, the reduction in power output due to temperature is much lower when partially shaded compared to that when the module is uniformly irradiated. This implies that the temperature coefficient of the module is much higher at partial shading. It could be due to the non-uniform temperature and irradiance distribution over the cells throughout the PV module. Hence, assuming a constant temperature coefficient for all the shading profiles (i^c) might lead to inaccuracies. Therefore, equation 3.2 does not hold true in reality. Thus, instead of studying the change in ST with the module temperature, it was analyzed by varying the ambient temperature.

3.2. Experimental validation

Four different PV modules (2 mono c-Si, 1 poly c-Si and 1 CIS) were tested for their ST at three different ambient temperatures. The experimental setup was almost the same as the indoor measurement of ST where 64 different shading profiles were applied to the PV modules. However, in addition to the STC measurement at 25 °C, here, $\%ST$ was also measured at ambient temperatures of 30 °C and 35 °C, respectively. The deviation in the air temperature under the LASS was about ± 1 °C. Again, the shading object transmitted 25% of the incident irradiance which would mean that the shaded region received 250 W/m² whereas the unshaded region received 1000 W/m². I-V measurements were taken at 1000 W/m² and AM 1.5 using the EternalSun LASS and ReRa I-V Curve Tracer 3 software and the output power at each shading profile for a given ambient temperature was recorded.

The average time taken for each set of measurement was about 8.11h. This was mainly due to the fact that at higher temperature, the module gets heated quickly under the LASS and a significant amount of time was required to cool down the PV modules and bring the module temperature back to the same value as the previous measurement. However, the measurement time can be reduced by automation of the shading and cooling processes. Figure 3.2 presents the $\%ST$ measured at three different ambient temperatures for the four PV modules. The module numbers in the figure correspond to the serial number of the PV modules as shown in Table 2.1.

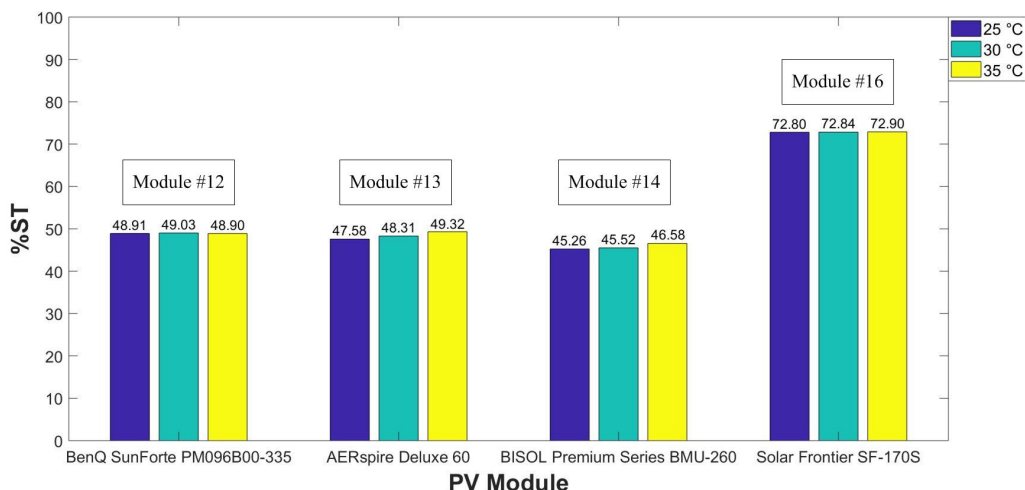


Figure 3.2: Experimental results for measurement of ST at different ambient temperatures.

It can be seen that the ST of a PV module shows a slightly increasing trend with ambient temperature. This is mainly due to the reason that the module exhibits higher temperature coefficient when partially shaded due to which there is not much effect on the module output due to temperature. However, the module output when unshaded (000000) declines rather sharply. Hence, as the ambient temperature is increased, if we look back to equation 2.2, we can see that the reduction in the numerator is lesser when compared to the denominator which leads to a slightly higher value of ST . Besides, in addition to the error due to the equipment, there will always be some differences in the cell temperatures of the PV module during the measurements which can also affect the results.

Table 3.1: Deviation from % ST at 25 °C.

PV Module	% Error	
	30 °C	35 °C
Module #12	0.25	-0.02
Module #13	1.53	3.66
Module #14	0.57	2.92
Module #16	0.05	0.14

In the above table, the % error for 30 °C and 35 °C represents the deviation of % ST at the respective temperatures from the % ST at 25 °C. On an average, the percentage error was 1.14%. The average change in % ST with temperature was 0.07 % ST /°C. It can be observed that the change in ST with temperature is not much significant and therefore, it can firmly be concluded that the ST of a PV module is almost independent of the ambient temperature. Hence, the Shading Tolerability of a PV module can be treated as its characteristic parameter.

3.3. Boundaries for temperature class

Now that ST has been established as a fundamental property of a PV module, it can be used as a quintessential aspect of our selection map. However, similar to shading classes based on ST , it is also necessary to classify PV modules based on their γ to determine their suitability for a given temperature condition. Currently, c-Si based PV modules dominate the PV industry where it accounted for 94% of the total production in 2016 whereas thin film technologies had a meagre share of 6% [2]. Since, γ differs with technology, there is a wide range of temperature coefficients currently available in the PV market.

tion map is suggested.

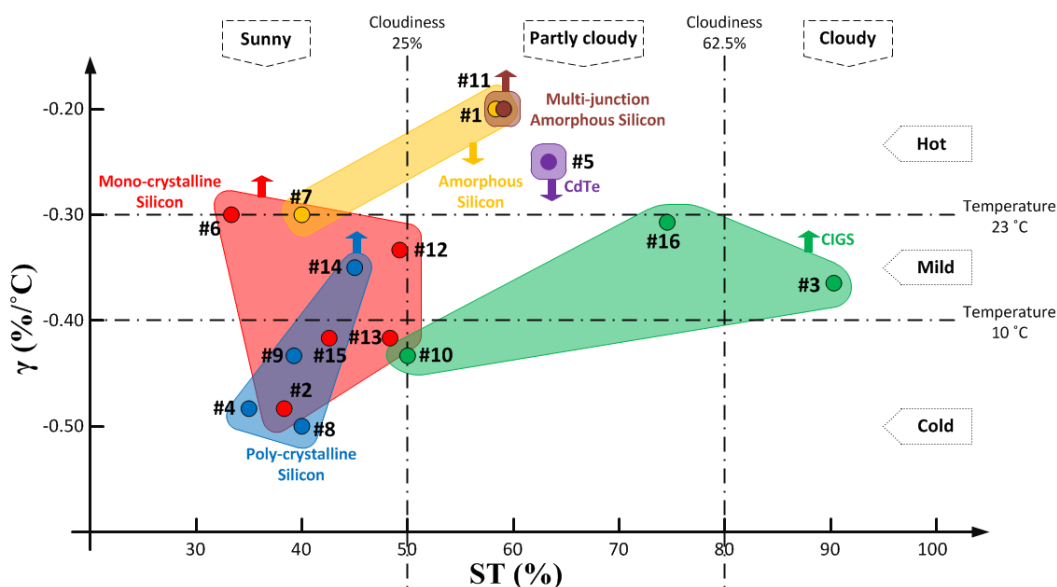


Figure 3.5: Selection map for PV module installation based on Shading Tolerability and Temperature Coefficient.

Since PV modules operate only during the daytime, the cloudiness and temperature parameters refer to the average annual daytime values in the above figure. The vertical dotted lines correlate cloudiness with ST values. The cloudiness values were inspired from meteorology where cloud cover is classified as; sunny ($CC < 25\%$), partly cloudy ($25\% \leq CC < 62.5\%$) and cloudy ($CC \geq 62.5\%$) [45]. Similarly, the horizontal dotted lines suggest the boundaries compatible with PV module's temperature coefficient values and the location's mean daytime temperature. The classification is a concise modification of the Universal Thermal Scale (UTS) used in Trewartha Climate Classification [46]. Here, it is expressed as hot ($T > 23^\circ\text{C}$), mild ($10^\circ\text{C} < T \leq 23^\circ\text{C}$) and cold ($T \leq 10^\circ\text{C}$). Based on the distribution of every point for respective PV technologies, a suitable geometric shape was created for each technology. Since, the map is derived from measured values, a tolerance of $\pm 5\%$ was maintained around the vertices. The arrows in the diagram suggest the response of the respective PV technology to red-shifted spectrum [47–49]. The numbers in the figure correspond to the serial number of the PV modules as shown in Table 2.1.

According to the selection map, crystalline silicon PV modules have much lower ST and γ values than thin film modules. Therefore, they are more suitable for locations that are sunny with cold or mild temperature conditions. On the other hand, thin film technologies are optimal for partly cloudy or cloudy locations with hot or mild temperature conditions. Normally, one would always want to select a PV module with higher ST and temperature coefficient values. However, the deployment of PV module can be significantly influenced by the meteorological conditions. For example, for a location that is mostly cloudy with mild temperatures, one would want to focus more on the ST values than the temperature coefficient. From the above map, CIGS technology would be a suitable choice for such a case. Therefore, the map gives a good indication for the module to be chosen depending on the climatic condition. However, it should be noted that the above selection map is a preliminary version that only includes data for PV modules that were tested during this thesis. Injection of more data may result to an even more detailed map. Also, with continuous innovations, temperature coefficients and shade tolerances of PV technologies have been improving steadily. This may subject the map to further changes. Moreover, similar to temperature coefficient values, inclusion of ST in a PV module's datasheet can lead to further improvement of the map since readily available values can help to create a selection map with greater detail.

In the next chapter, study of various meteorological parameters and different interpolation techniques are carried out to accurately estimate the climatic scenario of The Netherlands. The results are then applied to the selection map to determine the most suitable PV technology for The Netherlands by studying the annual temperature and cloudiness conditions of the country.

4

Interpolation Techniques for Meteorological Data

Meteorological data are vital to analyze the performance of any PV system. Since, the goal here is to study the coherence of the selection map by comparing performance ratio of different PV systems, it is essential to collect solar irradiance data for the installation location of these systems. Moreover, as we aim to determine the most suitable PV technology for The Netherlands, it is important to visualize the climatic conditions such as annual average temperature and cloudiness for every region of the country. However, these parameters are generally recorded only at specific locations. Therefore, to generate a map based on the above mentioned parameters, interpolation of measured local information is required to create a continuous set of data.

In this chapter, we first look into the measured data derived from different weather stations followed by a brief discussion about existing interpolation techniques. Next, visual maps of The Netherlands based on parameters such as air temperature, cloud fraction and GHI is shown using a suitable interpolation method. Finally, error calculation for the model used is presented.

4.1. Meteorological data

To determine the most suitable PV technology for The Netherlands, it is crucial to understand the climatic conditions of the country first so that one can have a proper reference for the temperature and cloudiness conditions in the PV selection map. Hence, measured data for different meteorological parameters were extracted from the database of weather stations situated in The Netherlands as well as neighbouring stations in Germany and Belgium. These weather stations are overseen by meteorological institutions such as *Koninklijk Nederlands Meteorologisch Instituut* (KNMI), *Deutscher Wetterdienst* (DWD) and *Koninklijk Meteorologisch Instituut van België* (KMI), respectively. The data extracted were from the period 2011-2016. The extracted parameters are as follows:

a) Atmospheric temperature:

Atmospheric temperature is a physical quantity expressing hotness or coldness at different levels of the Earth's atmosphere. Hourly air temperature measurements from 2011-2016 were gathered. According to the meteorological institutes, these observations were taken at a height of 1.50 m from the ground level [50–52]. The data from the Dutch weather stations were in 0.1 °C and therefore, converted to °C by multiplying them with 0.1 for ease of calculation.

b) Cloud cover:

The term cloud cover refers to the portion of the sky obscured by clouds when observed from a specific location on Earth [53]. It is measured in Oktas where the number of eighths of the sky covered by clouds describe the sky conditions. Hourly measurements of this parameter for all the weather stations was taken.

c) Global Horizontal Irradiation (GHI):

The term 'irradiance' refers to the instantaneous solar power incident on a surface of 1 m^2 and is measured in W/m^2 whereas 'irradiation' is the integral of the solar irradiance over time and is expressed in Wh/m^2 . In this work, hourly value of Global Horizontal Irradiation (GHI) i.e., solar irradiance incident on a flat surface over a period of time, measured in Wh/m^2 were used. The Dutch weather stations provide hourly GHI values in J/cm^2 that were changed to Wh/m^2 by multiplying the values with 2.78 ($1 \text{ J}/\text{cm}^2 = 2.78 \text{ Wh}/\text{m}^2$).

These parameters are generally widely measured since the measuring equipment are straightforward and easy to maintain. However, instrumental time series are always affected by missing values which could be due to interruptions in automatic stations, equipment malfunction or network re-organizations [54]. In this thesis, since the number of missing data was relatively low (2.24%), it was assumed that the set of data represented one continuous series and therefore, the missing values were ignored. On the contrary, if the total number of missing data constitute a significant amount of measurements, this approach reduces the period of recording and may lead to overestimation of the occurrence of extreme events [55, 56]. Figure below presents the locations of all the weather stations that were considered along with the parameters measured by the respective stations.



Figure 4.1: Weather stations used to derive meteorological data.

4.2. Interpolation of meteorological data

Interpolation is a method of generating continuous fields from a set of variables measured at specific point locations [57]. This is not a straightforward process, especially, for study areas that are spatially heterogeneous in nature. For an instance, regions where plains and mountains lie adjacently can be complicated to interpolate. However, since climate data are spatially irregular, they need to be interpolated to create a uniform field of data. There are a number of methods described in literature to carry out such operations. This thesis restricts itself into detailed analysis of five most used techniques to select the method that provides the best estimate.

4.2.1. Interpolation techniques

In this section, details of different interpolation techniques along with their advantages and disadvantages are briefly discussed.

a) Inverse Distance Weighted (IDW) Method:

The IDW method is a simple and straightforward deterministic interpolation technique. This method assumes that objects that are close to one another are more similar than the ones that are farther apart [58]. For a given unmeasured point location, IDW uses measured data from neighboring locations to estimate a value. The neighboring location that is nearest to the prediction location will have more influence than the ones that are farther away. Hence, the weight of the measured locations diminishes with its distance from the prediction location. This method can be expressed by the following equation [59],

$$Z_{IDW} = \frac{\sum_{i=1}^n \frac{Z_i}{c_i^\beta}}{\sum_{i=1}^n \frac{1}{c_i^\beta}} \quad (4.1)$$

where Z_{IDW} is the estimated value, Z_i is the measured value at i^{th} location and c_i is the distance between the i^{th} location and the prediction location. β is the power value which is determined by minimizing the Root Mean Square Error (RMSE). A higher value of β indicates that the influence of the measured locations decays faster with distance.

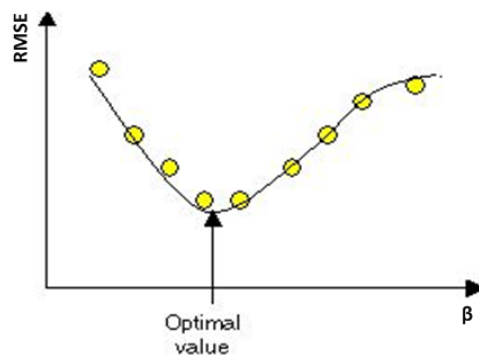


Figure 4.2: Example plot for RMSE with different values of β [58].

It can be seen that this method does not take any topographical information into consideration and is therefore, prone to inaccuracies for spatially heterogeneous locations. IDW also results in higher values near observed locations known as boundary effect or "bull's-eye effect". Moreover, this method interpolates only between the boundaries of the measured values and cannot create ridges or valleys if these extremes are not already included in the sample data [59]. However, it is a fast method that is extremely easy to apply.

b) Ordinary Kriging (OK):

Ordinary Kriging is a stochastic method that is based on statistical models. These models include the statistical relationships between the measured points which is known as autocorrelation [60]. This method is suitable when the spatial autocorrelation between variables is high. For example, it generates consistent thermal gradients for gentle topographies when used for temperature [57].

Interpolation with OK is carried out in multiple steps where first statistical analysis of the data is required. Next, an empirical semivariogram needs to be created.¹ The spatial autocorrelation for the measured locations is described by this semivariogram. It is then fitted with a suitable variogram model. Each model is designed to fit different types of phenomena more accurately. Once a suitable variogram model is identified, one can make estimations based on the fitted model [60]. Similar to IDW, Kriging specifies weights to measured data. However, these weights come from the semivariogram developed on the basis of the spatial distribution of the measured data.

¹Semivariograms are functions that depict the change in the spatial dependency between two observation points with change in distance.

The general formula for OK is [60],

$$\hat{Z}(s_0) = \sum_{i=1}^n \lambda_i Z(s_i) \quad (4.2)$$

where $\hat{Z}(s_0)$ is the predicted value, $Z(s_i)$ is the measured value at i^{th} location and λ_i is the weight for the measured value at i^{th} location. The value of the weight λ_i depends on the fitted model used, the distance between the measured and prediction location, and the spatial relationships among the measured values around the prediction location. OK is generally more accurate than IDW, however, it requires more experience regarding the selection of semivariogram and the amount of calculations make it a slower process [61].

c) Multiple Linear Regression (MLR):

The MLR model expresses linear relationships between the response and exploratory variables also known as dependent and independent variables, respectively. This method, when used for interpolating temperatures, is more suited when the spatial variation is dominated by prominent relief [57].² MLR is defined by the following equation [62],

$$Z(s) = \beta_0 + \sum_{k=1}^p \beta_k X_k(s) + \varepsilon(s) \quad (4.3)$$

where $Z(s)$ is the dependent variable at location s , β_0 is the intercept, β_1 to β_p are the regression coefficients of the independent variables X_1 to X_p . The residual term at location s is assumed to be normally distributed and uncorrelated, and is denoted by $\varepsilon(s)$. Estimation of the regression model is done by least squares such that the sum of squares of the differences between the observed and predicted values is lessened [62]. This method does not take the distance between stations into account and is therefore, more effective for heterogeneous topography where large differences can arise over short distances [57]. However, homogeneous sectors are greatly influenced by the distance due to the regular gradient between the dependent and independent variables. In such cases, IDW or OK should be preferred [57].

d) Regression Kriging (RK):

Regression and Kriging are two complementary methods. To utilize the advantages of both the methods, the RK model was introduced where regression is followed by kriging of residuals [57]. In the regression part, MLR is applied. Then, the residual is no longer treated as uncorrelated but modeled as spatially correlated [62]. Due to this fact, OK cannot be applied since it assumes that the constant mean is unknown. Instead, Simple Kriging (SK) is used since it can be assumed that the residual has a known mean (zero) in this method [62]. Finally, the results pertaining to the kriged residual is included with the regression result. The equation for RK is written as,

$$Z(s) = \beta_0 + \sum_{k=1}^p \beta_k X_k(s) + \sum_{i=1}^n \lambda_i \varepsilon(s_i) \quad (4.4)$$

The terms in the above expression refer to the same parameters as in OK and MLR. Hence, RK can be viewed as an extension of the MLR model. The addition of residual kriging to regression helps to include more information and gain more accurate estimates [62]. However, the disadvantage of this model is that calculations can end up to be extremely complex making it to be a time consuming method.

e) Temperature Lapse Rate (TLR) Method :

As suggested by the name of the model, TLR is used to interpolate temperatures. It assumes that temperature decreases with increase in elevation. The difference in altitude of the weather stations is calculated first and an average lapse rate in °C/m is adopted. These two parameters are then used to predict the unmeasured temperature values [61]. TLR is a complex method that is suitable for mountainous regions, however, it is not preferred for plain areas [61].

²In geography, relief is defined as the difference between the highest and the lowest elevations in an area.

The table below lists the strengths and weaknesses of the different interpolation techniques discussed above.

Table 4.1: Characteristics of different interpolation techniques.

Methods	Characteristics
IDW	Advantages: Fast, accurate, ease of application, suitable for plains, no special requirements. Disadvantages: Extremely simple, prone to boundary effect, unable to predict extreme events, unsuitable for heterogeneous sectors.
OK	Advantages: Considers statistical relation between measured values, no boundary effect, suitable for gentle topographies. Disadvantages: Slower, larger calculations, experience required to select correct variogram, unsuitable for mountainous regions.
MLR	Advantages: Can make overall estimate of error, suitable for heterogeneous topography. Disadvantages: Complex, does not take distance into account, unsuitable for plains.
RK	Advantages: Combines regression and kriging, leads to additional information in the interpolation, accurate. Disadvantages: Complex to apply, large amount of calculations.
TLR	Advantages: Considers the lapse rate of temperature, suitable for mountainous area. Disadvantages: Large amount of calculations, unsuitable for plains.

4.2.2. Selection of interpolation method

The Netherlands is a small country with an area of 41,543 m² [63]. The latitude of the country ranges from 50.7°N to 53.6°N whereas the longitude ranges from 3.3°E to 7.2°E. Moreover, the country is almost entirely flat with only a small portion where the altitude is higher than 100 m. The elevation in the country ranges from -7 m to 350 m [64]. Therefore, since there is no significant difference in the latitude, longitude or the topography, it is safe to assume that the entire country experiences almost similar climatic conditions.

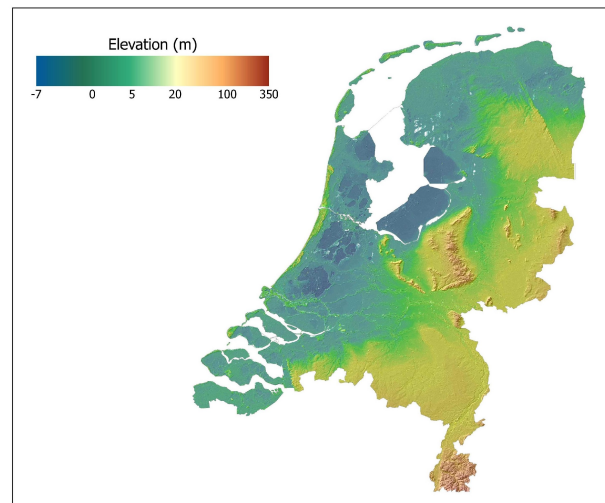


Figure 4.3: General map of The Netherlands. A significant part of the country lies below sea level whereas almost the rest of it are lowlands. There are small hills at the southernmost region of the country [64].

From the previous section, it can be deduced that the interpolation techniques that are suitable for plain areas are IDW, OK and RK methods. Among them, RK is the most accurate method. However, since The Netherlands is a flat country coupled with the fact that here, the interpolation is only carried out for annual average values, the level of accuracy gained with OK or RK methods is not much significant compared to the amount of calculations that need to be carried out. Moreover, the density of weather stations was high enough to achieve rational amount of accuracy even with the simplest of method. Hence, the IDW method

was selected to create a map of The Netherlands for the annual average daytime temperature, annual average daytime cloud fraction and annual GHI.

4.3. Computational details

For the interpolation using IDW method, equation 4.1 was applied. β was taken as 1 since the RMSE errors were least for this value. The results for the error analysis can be found in Table 4.2. The neighborhoods for the prediction location was defined by considering stations within a fixed distance. In this case, the distance was fixed at 50 kms for the interpolation of all three parameters since the number of stations taken into consideration by each point ranged from 3-9 which ensures sufficient statistical basis for the representation of local climatic conditions [65]. The distance between the prediction location and the weather stations was calculated using the Haversine formula which can be expressed by the following three equations [66],

$$a = \sin^2\left(\frac{\phi_1 - \phi_2}{2}\right) + \cos\phi_1 \cdot \cos\phi_2 \cdot \sin^2\left(\frac{\lambda_1 - \lambda_2}{2}\right) \quad (4.5)$$

$$c = 2 \cdot \text{atan2}(\sqrt{a}, \sqrt{1-a}) \quad (4.6)$$

$$d = R \cdot c \quad (4.7)$$

where d is the distance between the two points, ϕ_1 and ϕ_2 are the respective latitudes while λ_1 and λ_2 are the longitudes of the two locations, respectively. R is the radius of the Earth which was taken to be as 6371 km. To interpolate GHI, if the hourly measurements were in J/cm^2 , they were first converted to Wh/m^2 . The hourly values in Wh/m^2 for each year in 2011-2016 were summed. The average of these six yearly values in kWh/m^2 was taken as the annual average GHI of each weather station. Then, the annual mean GHI values were interpolated using IDW for every unmeasured point. Finally, the value determined for every point was used to create the GHI map.

To create the map for annual average daytime temperature and cloud fraction, the values corresponding to daytime was differentiated first. This was done by calculating the altitude of the Sun for every hour at every weather station in the period 2011-2016. This is briefly explained in 4.3.1. Now, only the hourly values with positive value of altitude of the Sun were taken into account. An average value for both, daytime temperature and cloud cover was calculated for every year. Again, the yearly values of daytime temperature and daytime cloud cover for 2011-2016 were averaged to get the annual mean daytime temperature and the annual mean daytime cloud cover for each weather station. Finally, these values were interpolated for every unmeasured point using IDW. The cloud cover values were converted to cloud fraction by dividing them by 8. These values were then used to generate the maps using QGIS.

4.3.1. Calculation of the Sun's altitude

As explained by *Smets et al.*, the position of the Sun can be described by first expressing the time (D) elapsed since Greenwich noon, terrestrial time, on 1 January 2000, in days [6]. The time D can be associated to Julian Date (JD), the number of days since 1 January 4713 BC in a proleptic Julian Calendar as [6],

$$D = JD - 2451545.0 \quad (4.8)$$

Next, the mean longitude (q) and the mean anomaly (g) of the Sun can be calculated. However, they need to be corrected to the aberration of the light and the elliptic orbit of the Earth, respectively.

$$q = 280.459^\circ + 0.98564736^\circ \times D \quad (4.9)$$

$$g = 357.529^\circ + 0.98560028^\circ \times D \quad (4.10)$$

The values of q and g were normalized from 0° - 360° . Now, the ecliptic longitude of the Sun can be found using equation 4.11 [6].

$$\lambda_S = q + 1.915^\circ \sin(g) + 0.020^\circ \sin(2g) \quad (4.11)$$

It is important to transform from ecliptic to horizontal coordinates and the angle ϵ by which the fundamental plane of these coordinates is tilted to the ecliptic plane is given by [6],

$$\epsilon = 23.429^\circ - 0.00000036^\circ \times D \quad (4.12)$$

Now, to calculate the local mean sidereal time θ_L , which is the angle between the vernal equinox and the meridian, we first have to determine the Greenwich Mean Sidereal Time (GMST) which is approximated by [6],

$$GMST = 18.697374558 + (24.06570982441907 \times D) + (0.000026 \times T^2) \quad (4.13)$$

where T is the number of centuries past since Greenwich noon, terrestrial time, on 1 January 2000 and is given by [6],

$$T = \frac{D}{36525} \quad (4.14)$$

$GMST$ is calculated in hours and needs to be normalized from 0-24 h. We can now obtain the local mean sidereal time in degrees as [6],

$$\theta_L = (GMST \times \frac{15^\circ}{hour}) + \lambda_0 \quad (4.15)$$

where λ_0 is the longitude of the observer. Now, the final expression for the exact elevation of the Sun can be calculated using the equation below [6],

$$\sin(a_S) = \cos(\phi_0) \cdot \cos(\theta_L) \cdot \cos(\lambda_S) + [\cos(\phi_0) \cdot \sin(\theta_L) \cdot \cos(\epsilon) + \sin(\phi_0) \cdot \sin(\epsilon)] \cdot \sin(\lambda_S) \quad (4.16)$$

where a_S is the altitude angle of the Sun. ϕ_0 is the latitude of the observer.

4.4. Meteorological maps of The Netherlands

Based on the approach explained above, the following maps were created. The maps use increments of 0.1 °N and 0.1 °E of latitude and longitude, respectively. Each point in the map represents the latitude and longitude of point locations. Therefore, each grid is a combination of four points and illustrates the average value of the respective four points. The maps were created using World Geodetic System 1984 (WGS84) projection.

4.4.1. Annual mean daytime temperature

From the map, it was observed that the mean daytime temperature in a year was nearly the same throughout the country. The northern region was found to be colder than the south, albeit only slightly. The range of annual mean daytime temperature for the entire country was found to be 12.0-13.6 °C. According to the temperature classification boundaries introduced in section 3.4, the daytime temperature conditions in the country can be classified as mild based on the results obtained.

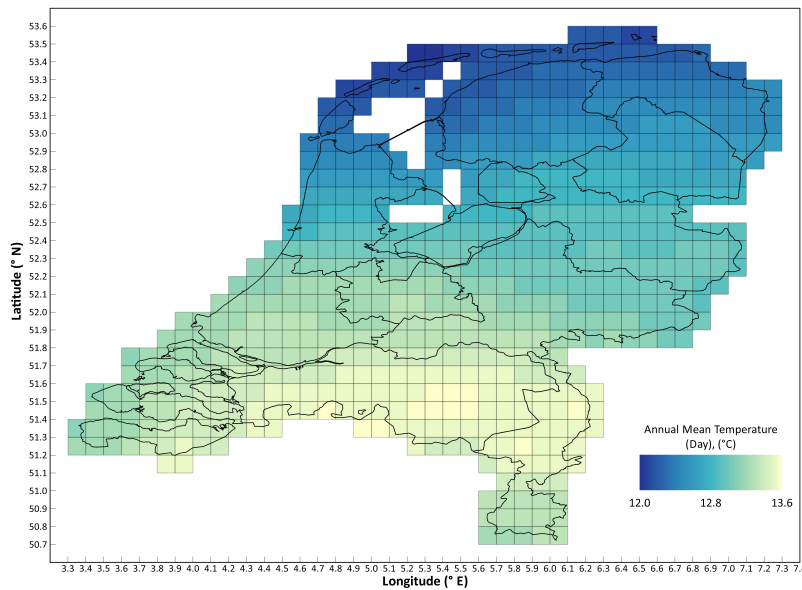


Figure 4.4: Map for annual average daytime temperature for The Netherlands.

4.4.2. Annual mean daytime cloud fraction

The map for cloud fraction again revealed that there was not significant change in mean daytime cloud fraction throughout the country. A gentle increasing pattern from west to east was observed. This could be due to the higher wind speeds at the coastal regions in the west leading to faster movement of clouds. The range of annual mean daytime cloud fraction was found to be 64-71%. Therefore, based on the meteorological classification established in section 3.4, the daytime cloudiness conditions of The Netherlands can be classified as cloudy. Hence, applying the classes thus found for annual mean daytime temperature and cloud fraction for The Netherlands in figure 3.5, it can be said that CIGS technology suits best for the country.

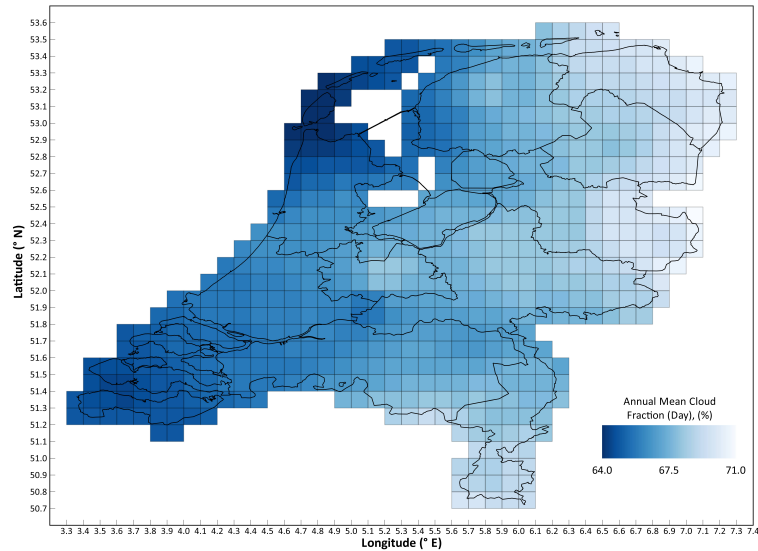


Figure 4.5: Map for annual average daytime cloud fraction for The Netherlands.

4.4.3. Annual mean GHI

Furthermore, to understand the irradiance conditions in the country, a map for annual mean GHI was also created. As suggested by the cloud fraction map, it was found that the western part of the country received more GHI than the east on an average. This is obviously due to the variation in the presence of clouds over the two regions. The range for mean annual GHI was determined to be 1018-1118 kWh/m²/year.

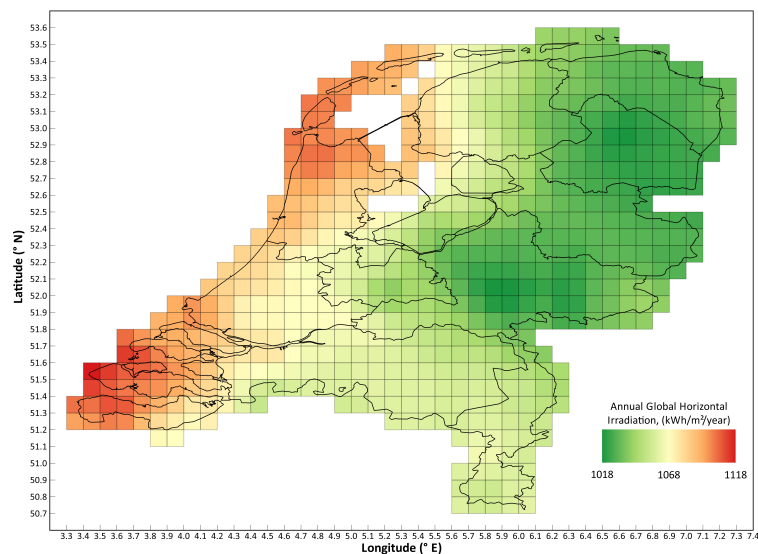
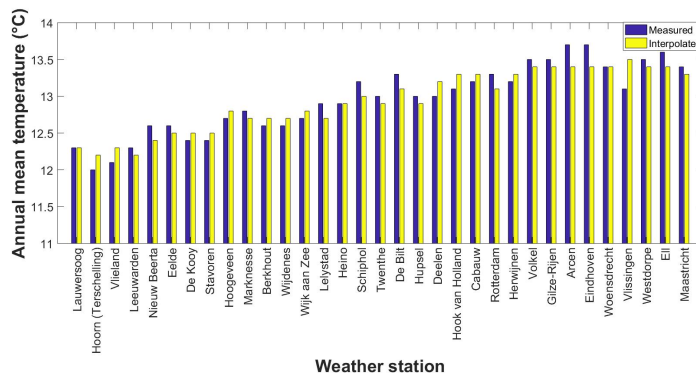


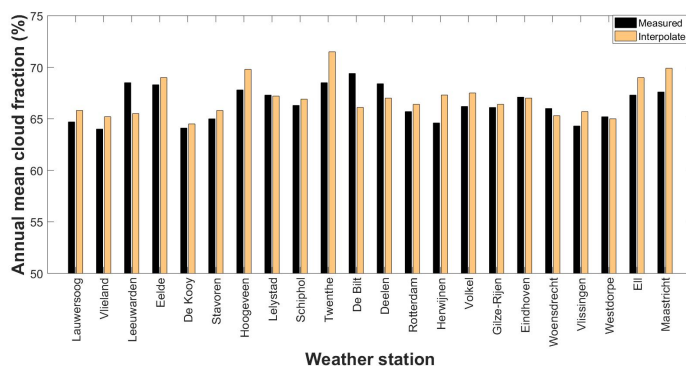
Figure 4.6: Map for annual average GHI for The Netherlands.

4.5. Spatial cross validation

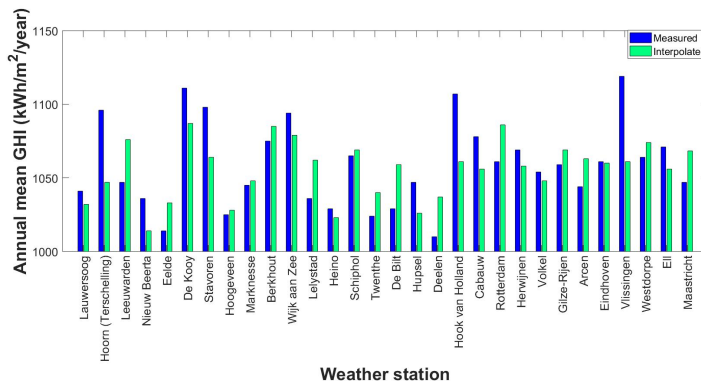
To estimate the error for the interpolation of the three parameters, a 'leave-one-out' approach was adopted. For each case, the measured parameter for weather stations was assigned as zero one at a time and the interpolation was carried out again to predict the respective value for the given measured location. As mentioned earlier, since the IDW method only interpolates between the boundaries, the error was higher for stations that corresponded to the extreme values. For example, the error was higher for the coldest and the warmest weather stations for the interpolation of mean daytime temperature. However, since there was not much significant difference in the range of temperature, cloud fraction or GHI for the entire country, the difference in the measured and predicted values for these extreme points was still relatively low. The deviations ranged between -0.3 °C to 0.4 °C, -3.3% to 3% and -58 kWh/m²/year to 30 kWh/m²/year for annual mean daytime temperature, cloud fraction and annual mean GHI, respectively. It should be noted that the figures below refer to the estimations carried out using β as 1.



(a) Annual mean daytime temperature.



(b) Annual mean daytime cloud fraction.



(c) Annual mean GHI.

Figure 4.7: Observed and predicted values of the three different parameters for different weather stations.

To compare the results, two statistical indicators namely, Root Mean Square Error (RMSE) and Mean Absolute Percentage Error (MAPE) were calculated. These indicators are given by the following equations [67],

$$RMSE = \sqrt{\frac{\sum_{i=1}^n (P_i - O_i)^2}{n}} \quad (4.17)$$

$$MAPE = \frac{1}{n} \sum_{i=1}^n \left| \frac{P_i - O_i}{O_i} \right| \times 100\% \quad (4.18)$$

where P_i and O_i are the predicted and observed values, respectively. n is the total number of samples. The indicator RMSE generally has a unit associated with it. It can be normalized by the average of the observed values and expressed in percentage as,

$$\%RMSE = \frac{RMSE}{\frac{1}{n} \sum_{i=1}^n O_i} \times 100\% \quad (4.19)$$

Based on the above equations, the error calculations pertaining to the interpolation of the three parameters are presented in the table below,

Table 4.2: Cross validation of interpolation results.

Parameter	%RMSE		MAPE (%)	
	$\beta = 1$	$\beta = 2$	$\beta = 1$	$\beta = 2$
Annual mean daytime temperature	1.32	1.37	1.10	1.12
Annual mean daytime cloud fraction	2.48	2.59	1.97	2.00
Annual mean GHI	2.26	2.31	1.84	1.89

The results obtained for %RMSE were well within the accepted value of 5% for the prediction of mean values for meteorological parameters [68]. However, it can be seen that the deviation of predicted values from observed data for annual mean daytime cloud fraction and annual mean GHI were relatively higher than that for annual mean daytime temperature. This was mainly due to the fact that the number of weather stations that measured these two parameters were much lower when compared to the weather stations that measured air temperature. Moreover, cloud cover is random in nature which makes it extremely difficult to predict it. This further contributes to error in the predictions.

Hence, based on the maps of The Netherlands generated using the IDW method and the selection map for PV module installation (figure 3.5), an immediate interpretation can be that the CIGS technology is the optimal choice of PV technology for The Netherlands. However, the practical relevance of this result needs to be investigated. Therefore, the performance of PV systems installed at locations with different temperature and shading conditions needs to be analyzed. To do so, it is first necessary to model the meteorological conditions of the locations accurately. Thus, the study of different irradiance decomposition models is presented in the next chapter.

5

Irradiation Decomposition Models

To study the performance of any PV system, it is important to obtain necessary information regarding the solar irradiance at the given location. Generally, these information pertain to the Global Horizontal Irradiance (GHI) and its two components namely, Direct Normal Irradiance (DNI) and Diffuse Horizontal Irradiance (DHI). However, most of the weather stations around the world are limited to the measurement of the GHI only. Due to this reason, various irradiance decomposition models that are based on empirical relations have been developed to decompose the global component into the direct and diffuse components.

In this chapter, a brief introduction about the different components of solar irradiance and their measurement is presented first. Following a brief discussion about the measured weather data, six different decomposition models have been implemented and evaluated to determine the most suitable model for The Netherlands. Finally, these models are evaluated based on the results obtained.

5.1. Solar irradiance

The intensity of direct beam component of solar irradiation weakens due to absorption and scattering as sunlight penetrates through the atmosphere. Moreover, the scattered light also partially reaches the surface of the Earth. Hence, the global component of solar irradiance incident on the Earth's surface is composed of these two components.

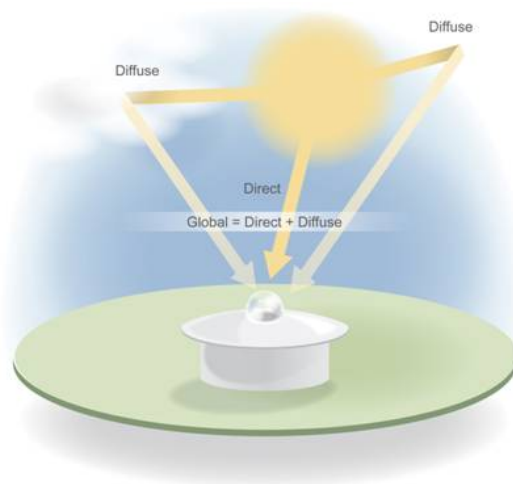


Figure 5.1: The three components of solar irradiance [69].

a) Direct Normal Irradiance (DNI):

It is the component of the sunlight that is unaffected by scattering and reflection due to the atmosphere. As can be seen in figure 5.1, it traverses in a straight line and can be received by a surface by tracking the Sun's position in the sky. It is measured by an instrument called pyrheliometer that has a small opening angle and is pointed directly towards the Sun's rays so that only the direct component is captured by it [70].

b) Diffuse Horizontal Irradiance (DHI):

It is the diffused or scattered component of sunlight received by a flat surface on the Earth's surface. This component is measured using a pyranometer and a shading disk that shades the dome of the pyranometer to block the direct component [70].

c) Global Horizontal Irradiance (GHI):

As discussed earlier in section 4.1, GHI is the total solar irradiance received by a flat surface on the Earth's surface. It is measured using a pyranometer where the irradiance is estimated by converting the voltage generated across the thermopile detector [70]. The pyranometer is normally mounted horizontally so that the field of view consists of the entire celestial hemisphere.¹ GHI is composed of both, direct and diffuse components and can be expressed mathematically as [71],

$$GHI = DNI \times \cos(\theta_z) + DHI \quad (5.1)$$

where θ_z is the solar zenith angle. Hence, if any two of these parameters are known, the third can be easily estimated using equation 5.1. However, measured values for DNI and DHI are rarely available due to the high maintenance costs involved with the measuring equipment [72]. Thus, normally only GHI values are recorded that need to be decomposed to estimate DNI and DHI.

5.2. Data process

To determine the most suitable irradiance decomposition model for The Netherlands, irradiation data along with other weather parameters from the Cabauw Experimental Site for Atmospheric Research (CESAR) was extracted. CESAR is maintained by KNMI and provides high quality irradiation measurements [50]. It is a part of the Baseline Surface Radiation Network (BSRN), a project that is aimed at detecting important changes in the Earth's radiation field at the Earth's surface which may be related to climate changes under the umbrella of World Climate Research Programme (WCRP) [73].



Figure 5.2: Map for meteorological stations maintained by KNMI in The Netherlands [50].

To study the various decomposition models, data from the period 2011-2016 was used. The data obtained from CESAR database had a resolution of 10 minutes and was aggregated to hourly values for ease of

¹Field of view is the extent of the surrounding observable from a point at any given time.

calculation. Based on different methods described in literature, various data checks were performed to remove erroneous values and maintain the quality of data [74–76]. Firstly, GHI, DHI and DNI measurements that were less than 0 W/m^2 or greater than 1300 W/m^2 were removed. Similarly, for cases where DHI values exceeded GHI, the corresponding measurements of DHI were set equal to the GHI. Finally, inaccurate data points based on the combinations of diffuse fraction and clearness index were eliminated [74, 77]. To do so, the following conditions were used,

$$\text{i. } k_d < 0.90 \text{ and } k_t < 0.20$$

$$\text{ii. } k_d > 0.80 \text{ and } k_t > 0.60$$

Here, k_d and k_t refer to diffuse fraction and clearness index, respectively. The diffuse fraction signifies the ratio of diffuse component with respect to the global component whereas the clearness index is a measure of cloudiness that signifies the proportion of extraterrestrial irradiation incident at a given location. Calculation of these parameters is explained in section 5.3. In the first case, spurious measurements pertaining to overcast conditions is removed since for a low clearness index, it is rational to assume that the diffuse fraction must be higher. Again, in the second case, measurements that result to unreasonably high diffuse fraction for a clear sky conditions are eliminated. The corresponding clearness index and diffuse fraction of the final dataset obtained is shown in figure 5.3.

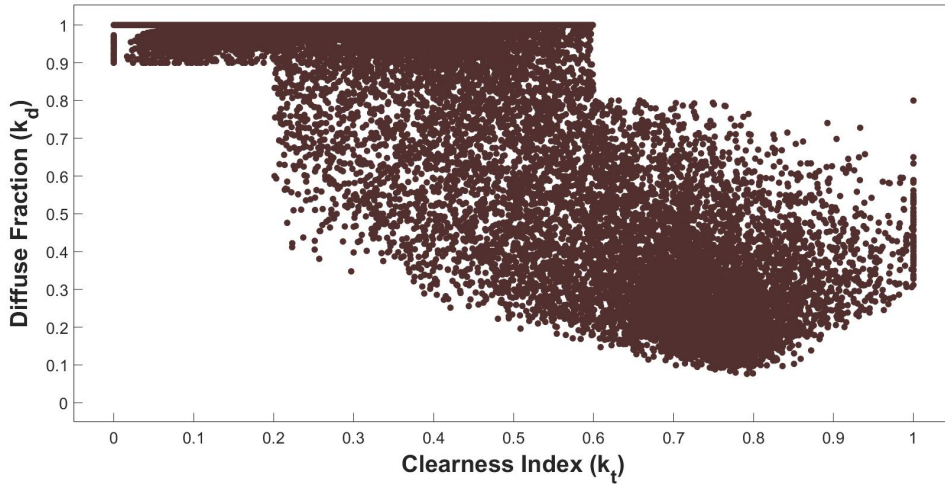


Figure 5.3: Clearness index and diffuse fraction based on measured values (CESAR, 2011-2016).

5.3. Decomposition models

Decomposition models are used to predict DNI and DHI values from measured GHI. Since the 1960s, a number of such models have been developed. One of the first decomposition models to be introduced was that by Liu and Jordan where interrelationship between GHI, DNI and DHI was established to determine the statistical distribution of the daily total radiation [78]. Further extension of Liu and Jordan's work was carried out by Erbs and, Orgill and Hollands where prediction of hourly diffuse fraction (k_d) was carried out using the clearness index (k_t) [77, 79].

$$k_t = \frac{GHI}{E_a} \quad (5.2)$$

$$k_d = \frac{DHI}{GHI} \quad (5.3)$$

where E_a is the extraterrestrial irradiance outside the Earth's atmosphere. It can be calculated using the following two equations [71],

$$E_0 = \left(\frac{r_0}{r} \right)^2 = 1 + 0.033 \cos \left[\frac{2\pi d_n}{365} \right] \quad (5.4)$$

$$E_a = E_{SC} \times (r_0/r)^2 \times \cos(\theta_z) \quad (5.5)$$

where,

E_0 = Eccentricity correction factor of the Earth's orbit

r_0 = Mean Sun-Earth distance = 149,597,890 \pm 500 km

r = The Sun-Earth distance at any day of the year (km)

d_n = Day number of the year

E_{SC} = Solar Constant = 1367 W/m²

In the late 1980s, several authors developed correlations between diffuse fraction and clearness index based on environmental predictors such as the Sun's altitude, temperature, relative humidity, etc [74, 80]. Maxwell introduced a model known as Direct Insolation Simulation Code (DISC) that was based on a modified clearness index derived from clear sky irradiation instead of extraterrestrial irradiation [81].

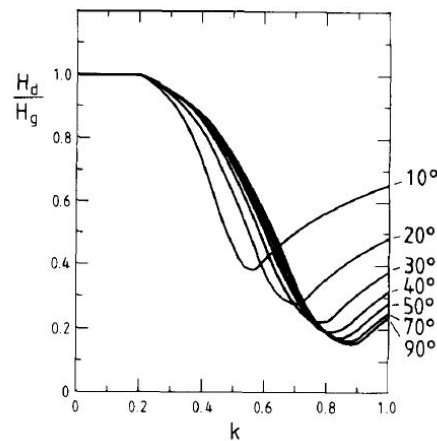


Figure 5.4: Hourly diffuse fraction modelled as a function of clearness index for different solar elevations using the Skartveit model [80].

Furthermore, Boland, Ridley and Lauret established the BRL model using multiple predictor variables and requiring as less recorded data as possible [82]. Finally, Jamodkar had proposed two new models called Dutch-I and Dutch-II to predict DHI and DNI that took the fluctuations in irradiance due to moving clouds into account [83].

In this thesis, six different decomposition models were studied. Although the Dutch-I and Dutch-II models were introduced using per minute data, here, the models are applied for hourly values. An in-depth description of five different models namely, Erbs, Reindl-2, Reindl-3, Dutch-I and Dutch-II is presented in Appendix B whereas the BRL model is explained in the following section. Table 5.1 lists the decomposition models considered in this work along with their input and output variables. In the given table, a_S refers to the solar elevation, T_a is the ambient temperature, RH is the Relative Humidity, AST is the Apparent Solar Time, K_t is the daily clearness index and ψ is the persistence. Each of these parameters is introduced and discussed in the next section.

Table 5.1: List of decomposition models.

Model	Input	Output
Erbs	k_t [77]	k_d
Reindl-2	k_t, a_S [74]	k_d
Reindl-3	k_t, a_S, T_a, RH [74]	k_d
BRL	k_t, a_S, AST, K_t, ψ [82]	k_d
Dutch-I	k_t, a_S [83]	k_d
Dutch-II	k_t, a_S [83]	k_d

5.4. BRL model

For the modelling of the diffuse component of solar irradiation, *Reindl et al.* had presented thorough statistical analysis of 28 different predictor variables where four of them, namely, clearness index (k_t), solar elevation (a_s), ambient temperature (T_a) and relative humidity (RH) gave the best results [74]. However, T_a and RH are measured variables that might not be recorded at sub-diurnal time scales for every location. Therefore, *Ridley et al.* developed the BRL model by studying measured data at seven different locations in both hemispheres of the world [82]. The model utilizes multiple predictor variables with minimum measured parameters to accurately predict the diffuse fraction [82].

Most of the decomposition models employ piecewise linear or simple non-linear equations. On the contrary, the BRL model is an extension of the single predictor generic model developed by *Boland et al.* which uses a logistic function where the hourly clearness index is applied as the sole predictor for the diffuse fraction [84]. The general equation for the single predictor model is [84],

$$k_d = \frac{1}{1 + e^{-5.0033 + 8.6025k_t}} \quad (5.6)$$

In the BRL model, four additional predictors are considered to develop the multiple predictor model. They are the solar elevation (a_s), Apparent Solar Time (AST), daily clearness index (K_t) and persistence (ψ) [82]. The general equation for the model is again a logistic function expressed as follows [82],

$$k_d = \frac{1}{1 + e^{-5.38 + 6.63k_t + 0.006AST - 0.007a_s + 1.75K_t + 1.31\psi}} \quad (5.7)$$

To implement the above equation, hourly values for k_t can be easily calculated by applying the measured hourly GHI in equation 5.2. Similarly, hourly a_s can be estimated using the method previously discussed in section 4.3.1. K_t signifies the cloudiness characteristic of the entire day and can be calculated as [82],

$$K_t = \frac{\sum_{i=1}^{24} GHI_i}{\sum_{i=1}^{24} E_{a_i}} \quad (5.8)$$

where GHI_i is the measured GHI at i^{th} hour and E_{a_i} is the extraterrestrial irradiation calculated for i^{th} hour. Next, the persistence (ψ) that is the average of the lag and lead of the clearness index can be calculated as follows,

$$\psi = \begin{cases} \frac{k_{t-1} + k_{t+1}}{2} & \text{sunrise} < t < \text{sunset} \\ k_{t+1} & t = \text{sunrise} \\ k_{t-1} & t = \text{sunset} \end{cases} \quad (5.9)$$

Apparent Solar Time (AST), also known as True Solar Time (TST), is derived from the Sun's motion and is based on the interval that it takes for the Sun to return to the local meridian [71]. This interval can be as large as 16 minutes and can be calculated using the equation of time (E_t) [71].

$$E_t = (0.000075 + 0.001868 \cos \Gamma - 0.032077 \sin \Gamma - 0.014615 \cos 2\Gamma - 0.04089 \sin 2\Gamma)(229.18) \quad (5.10)$$

where the unit for the first term is radians and is converted to minutes by the multiplier 229.18. Figure 5.5 illustrates the variation in E_t in a given year. Now, AST for every hour can be calculated as [71],

$$AST = h + TZ - \frac{\lambda}{15} + \frac{E_t}{60} \quad (5.11)$$

where h is the hour of the day. TZ is the time zone of the location with respect to UTC. λ is the standard longitude of the location and is divided by 15 to account for the difference between the local and standard meridians (longitude correction factor = 4 minutes for every degree) [71]. The equation of time is converted to degrees by dividing it by 60.

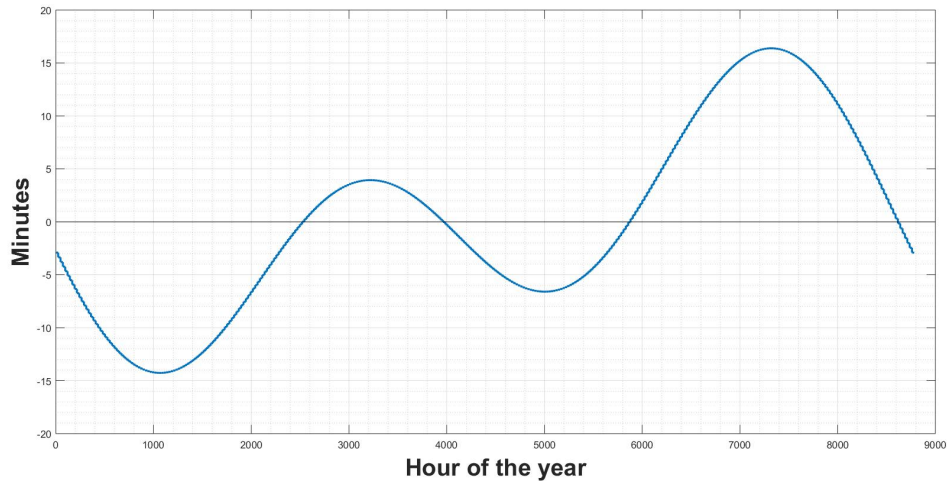


Figure 5.5: Annual variation of the equation of time (E_T).

Therefore, it can be seen that the BRL model only requires GHI as the measured parameter to predict the diffuse fraction. Although the number of input variables for the model is relatively higher, they can be computed easily as discussed above. Moreover, *Ridley et al.* had found that the model performs better than other conventional models for both hemispheres [82]. The performance of the model in comparison to the other five models studied in this work when implemented for The Netherlands is investigated and discussed in the next section.

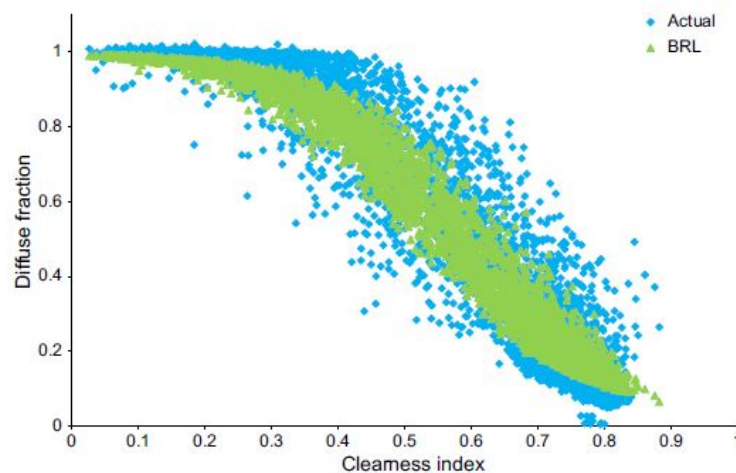


Figure 5.6: Measured data overlaid with results of BRL model for Adelaide, Australia [82].

5.5. Assessment of models

In this section, the performance of the six decomposition models is evaluated to determine the most suitable model for the case of The Netherlands. This was done by studying different statistical parameters explained in the following subsection.

5.5.1. Statistical indicators

The assessment of the models was carried out by studying four different statistical parameters namely, Mean Bias Difference (MBD), Composite Residual Sum of Squares (CRSS), %Relative Difference (%RD) and Root

Mean Square Error (RMSE). These indicators are given by the following equations.

$$MBD = \frac{\sum_{i=1}^n (M_i - C_i)}{n} \quad (5.12)$$

$$RD_i = \left| \frac{M_i - C_i}{M_i} \right| \times 100\% \quad (5.13)$$

$$CRSS = \sum_{i=1}^n [M_i - C_i]^2 \quad (5.14)$$

where M_i and C_i indicate the measured and computed diffuse fraction, respectively. n is the total number of samples. RMSE can be calculated in a similar fashion as explained in section 4.5. Here, the equations are re-written as,

$$RMSE = \sqrt{\frac{\sum_{i=1}^n (M_i - C_i)^2}{n}} \quad (5.15)$$

$$\%RMSE = \frac{RMSE}{\frac{1}{n} \sum_{i=1}^n M_i} \times 100\% \quad (5.16)$$

The RMSE and MBD values signify the goodness of the fitted model by providing a measure of how close the fitted values are to the measured points. However, it is not wise to draw conclusions based on these two indicators only. For an example, larger differences between the measured and fitted values for a few number of samples may increase the RMSE much more when compared with the MBD value. The lower value of MBD may be because the values might be overestimated or underestimated equally. Thus, the CRSS and %RD are also analyzed. CRSS indicates the total accumulated error of the model and a lower values of it is preferred.

5.5.2. Model comparison

In this section, the results obtained for all the six models are presented. Furthermore, the comparison of their performance relative to the measured values at Cabauw is analyzed by studying the above mentioned statistical indicators. As explained in section 5.2, the measured values shown here are after the removal of erroneous values for the period 2011-2016.

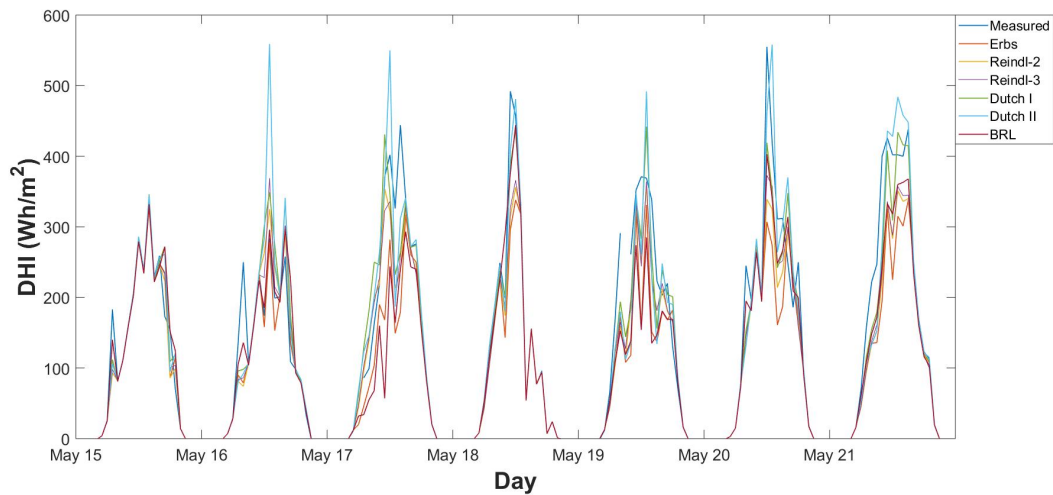


Figure 5.7: Measured and modeled DHI for a week in May 2012.

In figure 5.7, results for DHI pertaining to all the six models are compared with the measured values for 15th May-21st May, 2012. It can be observed that at lower values of DHI, all the models perform almost equally. At higher DHI values, Dutch-I, Dutch-II and BRL models perform better. However, the Dutch-II model was also seen to overestimate the value occasionally. The rest of the three models were found to be less accurate in this case with the deviation from measured values being much greater at higher values of DHI.

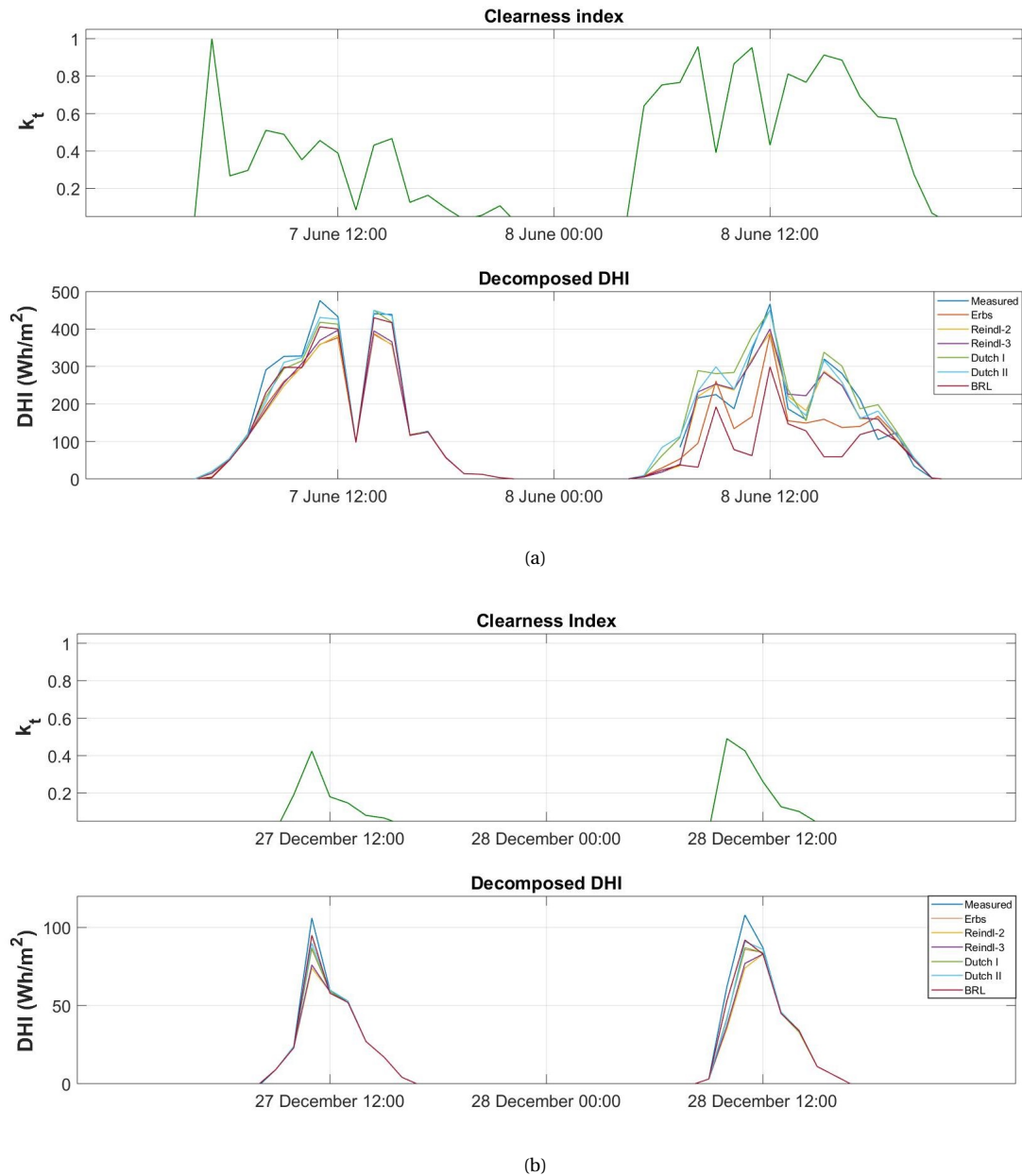


Figure 5.8: Clearness index and DHI for summer and winter days in 2012.

Next, the models were compared for two different days in June, 2012 and December, 2012, respectively to see the variations in results due to changing clearness index. The figures illustrate the clearness index calculated from measured GHI for the respective days along with the decomposed DHI value corresponding to it. It was observed that for cloudy times with low clearness index ($k_t < 0.4$), all the models performed almost equally with the BRL model being the most accurate. The BRL model performed the worst on clear sky conditions i.e. very high values of k_t ($k_t > 0.8$). The prediction from all the models was poor when the sky was partly cloudy. At clearness indices of 0.4-0.6, greater deviation between the measured and calculated DHI was observed. This can also be seen from the scatter plot presented below.

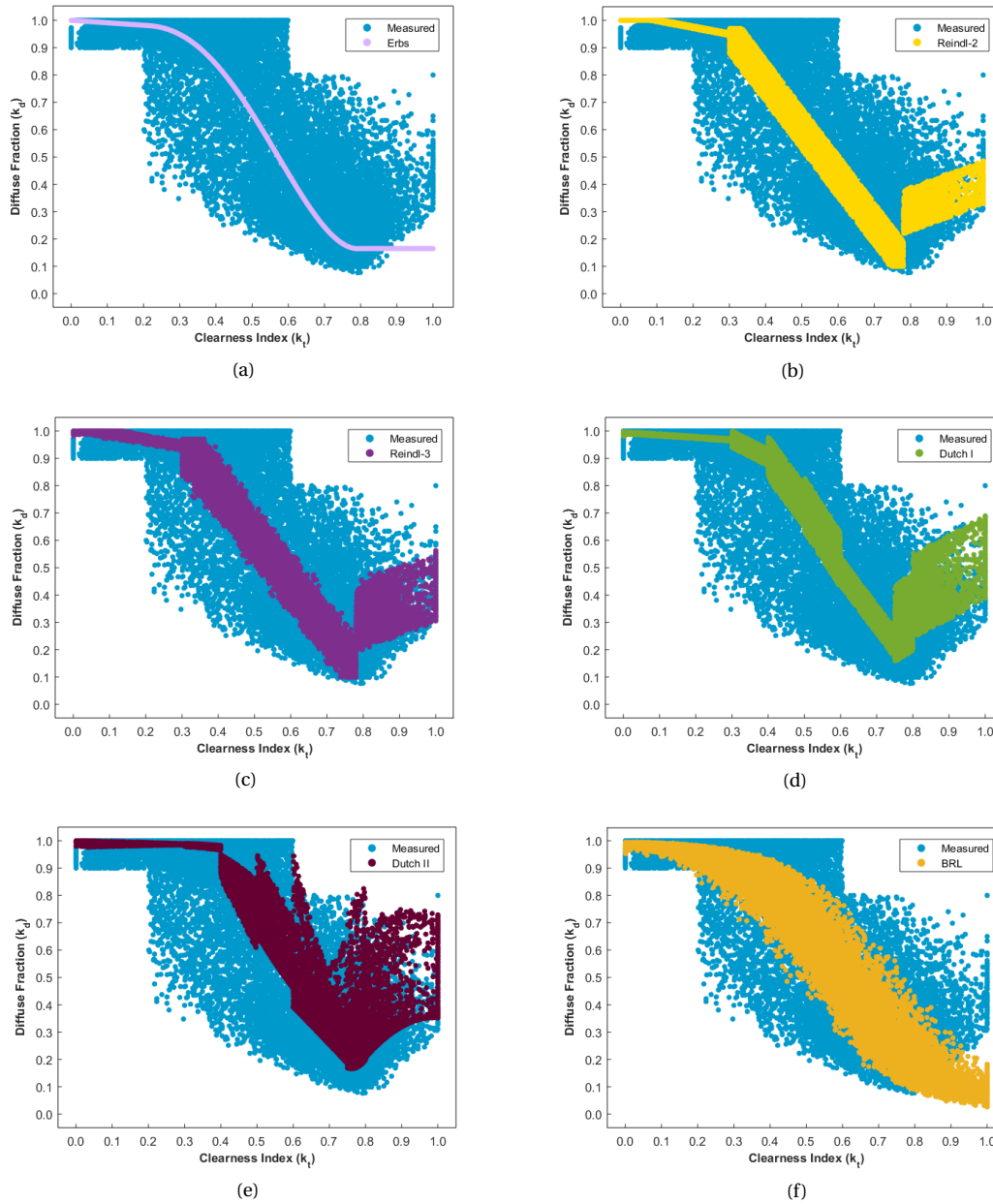


Figure 5.9: Comparison of clearness index and diffuse fraction for different decomposition models.

In the above figures, the blue region indicates the measured data points. Ideally, one would want to cover as much area of the measured value as possible using a decomposition model to achieve greater accuracy. It can be seen from the above figures that Erbs is an extremely basic model with high amount of errors when compared with the measured values. The Reindl-2 model improves it significantly by including the solar elevation along with the clearness index. The Reindl-3 model uses two more measured parameters than Reindl-2 to predict the diffuse fraction, however, it improves the results only slightly. The Dutch-I and Dutch-II models bring significant improvement in the results. Nevertheless, as can be seen from the figure, these two models have higher inaccuracies for low values of the clearness index. Finally, use of a logistic function makes the BRL model more accurate in lower and mid-range values of the clearness index. However, the deviation from measured values is greater than that for the other five models for very high clearness index. Evidently, none of the models are completely accurate in the prediction of diffuse fraction. This is because the value of DHI is dependent on a number of environmental factors such as cloud cover, cloud density, etc. and the models do not take all of these factors into consideration [83].

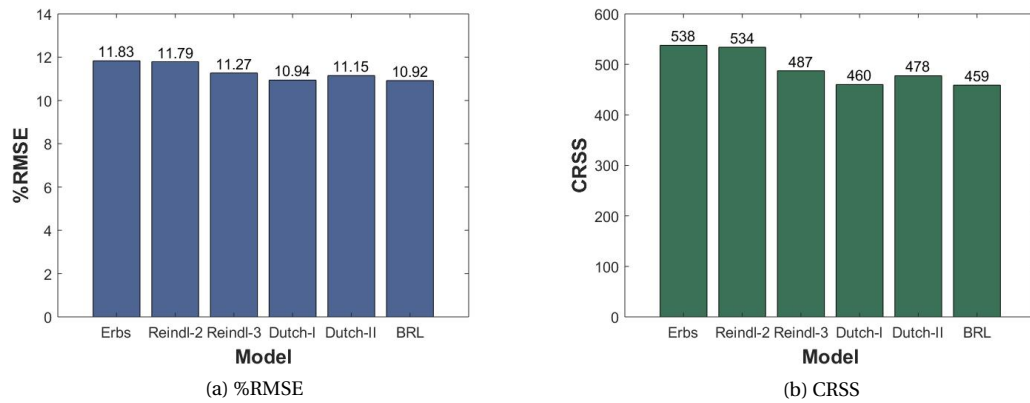


Figure 5.10: Model comparison based on %RMSE and CRSS.

Next, the different statistical indicators mentioned above were applied to each of the decomposition model. As shown in figure 5.10, the analysis of %RMSE illustrated that the BRL and Dutch-I models were the most accurate ones. Similar, conclusions were drawn from the CRSS analysis where the BRL and Dutch-I models indicated the least accumulated error. To get a further insight about the accuracy of these two models, the cumulative %RD was studied.

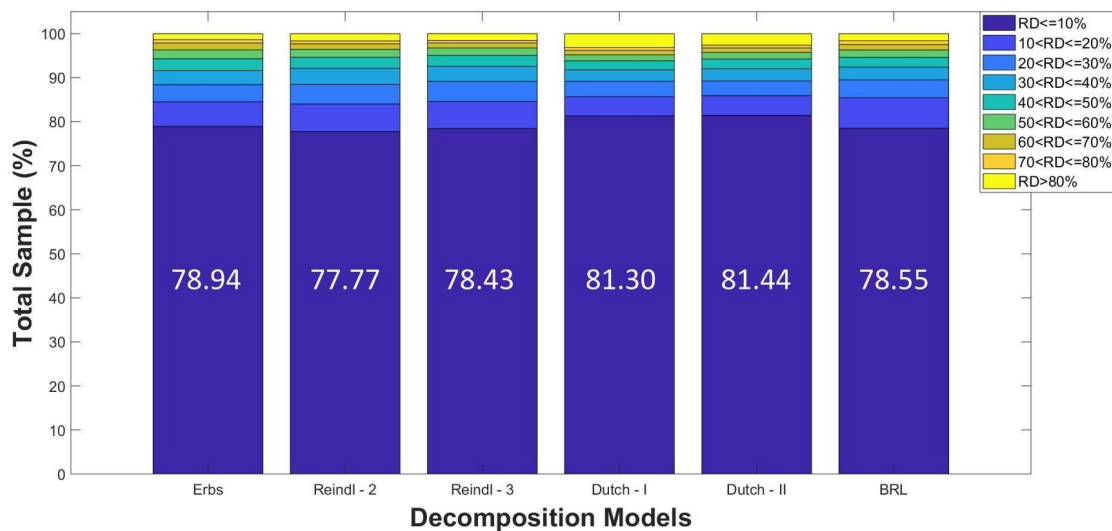


Figure 5.11: Comparison of decomposition models based on % RD.

In the above figure, the comparison for %RD for all the models is presented. The chart illustrates the percentage of samples with different ranges of %RD for each model. The lowermost box (dark blue) shows the percentage of sample where %RD was less than or equal to 10% whereas the topmost box (yellow) presents the percentage of samples with %RD greater than 80%. The most accurate model would have the highest percentage of samples in the lowermost box and least in the topmost box. Thus, based on the results obtained, it can be observed that the Dutch-II model had the most percentage of samples with %RD less than or equal to 10%, followed by Dutch-I and Erbs. However, it can also be seen that the percentage of samples with %RD greater than 80% was higher for Dutch-I and Dutch-II models (3.13% and 2.62%, respectively). This means that the models also overestimate or underestimate the diffuse fraction more than the other models. The BRL model had about 78.55% of the samples with %RD less than or equal to 10% and 1.59% percent of samples where the %RD was greater than 80%.

Hence, based on several analyses carried out, it was found that all the models perform equally on cloudy days ($k_t < 0.4$) with the BRL model being the most accurate. However, the deviation of predictions increased for partly cloudy skies for all the models. The BRL model was found to have the most error under clear sky conditions. Nevertheless, based on the study of different statistical parameters, it was found that the Dutch-I, Dutch-II and BRL models were the most suited decomposition models for The Netherlands where all the models had their own advantages and disadvantages.

In this thesis, to decompose the GHI values for the installation locations of different PV systems, the BRL model was used. The selection of the model was based on the facts that it was relatively more accurate for cloudy and partly cloudy conditions, it had the least %RMSE error among all the models and also that it is a tried and tested method known to present greater accuracies in all parts of the world [82]. In the next chapter, the irradiance data thus obtained from the BRL model is used to calculate the PR of several PV systems using a suitable irradiance transposition model.

6

Validation of Selection Map

The discussion presented based on the selection map and meteorological data suggests that CIGS technology is the optimal choice to design a PV system in The Netherlands. In this chapter, the practical relevance of this result is investigated. This is done by comparing the PR of various existing PV systems installed in The Netherlands. Thus, in this chapter, an introduction of different performance parameters is presented first. Next, a short explanation of the data used to calculate PR is demonstrated followed by a brief discussion on a suitable transposition model for The Netherlands to determine the POA irradiation. Finally, the PR of different PV systems is calculated and evaluated to examine the consistency of the selection map.

6.1. Performance parameters

Performance parameters enable designers to compare PV systems that may differ in design, may use different technologies or are installed in different geographic locations. The International Energy Agency-Photovoltaic Power Systems Programme (IEA-PVPS) have established parameters that delineate the energy quantities for a PV system and its components, and are presented in the IEC standard 61724 [11]. To study the overall performance of a PV system concerning the energy production, solar resource and the system losses, three of the parameters mentioned in IEC standard 61724 can be used and are as follows,

a) Final PV system yield:

The final PV system yield (Y_f) is the ratio of the net energy output of the system to the rated power of the PV array [85]. This parameter signifies the number of hours that the PV array would require to generate the same amount of energy when operated at its rated power. It is expressed in hours or kWh/kW_p, with the latter being the preferred unit since it exhibits the entities used to derive the parameter. Y_f makes it possible to compare energy produced by PV systems of varying size and can be expressed by the following equation [85],

$$Y_f = \frac{\sum_t P_{out}}{P_0} \quad (6.1)$$

where P_{out} is the power output of the PV array at a given instant (kW) and P_0 is the installed peak power of the PV array (kW_p).

b) Reference yield:

The reference yield (Y_r) is the ratio of the total in-plane irradiance to the PV's reference irradiance [85]. It signifies the number of hours equivalent to the reference irradiance. Thus, Y_r describes the quality of solar resource for the PV system. It is dependent on the system's location, PV array's orientation and the monthly as well as annual weather variability [85]. The unit for Y_r is hours.

$$Y_r = \frac{\sum_t G_{module}}{G_0} \quad (6.2)$$

where G_{module} is the irradiance incident at the plane of the PV array (kW/m²) and G_0 is the reference irradiance and is equal to 1 kW/m².

c) Performance Ratio:

The Performance Ratio (PR) is a dimensionless number and is given by the ratio of Y_f and Y_r . Since this parameter is normalized with respect to irradiance, it describes the overall effect on the peak power output due to losses such as non-absorption due to reflection from PV module surface, PV module temperature, mismatch due to partial shading, soiling, component failures as well as inverter inefficiency and cable losses [85]. This makes it possible to compare the performance of PV systems that may use different PV technologies or are installed in different geographic locations. Therefore, the parameter PR was chosen as a metric to distinguish various existing PV systems installed in The Netherlands.

$$PR = \frac{Y_f}{Y_r} = \frac{G_0}{P_0} \times \frac{\sum_t P_{out}}{\sum_t G_{module}} \quad (6.3)$$

6.2. PV systems data description

To analyze the coherence of the selection map, several PV systems currently installed in The Netherlands that are monitored by the Delft based company called Solar Monkey B.V. were studied. Figure 6.1 shows the location of these systems along with the PV module used by them.

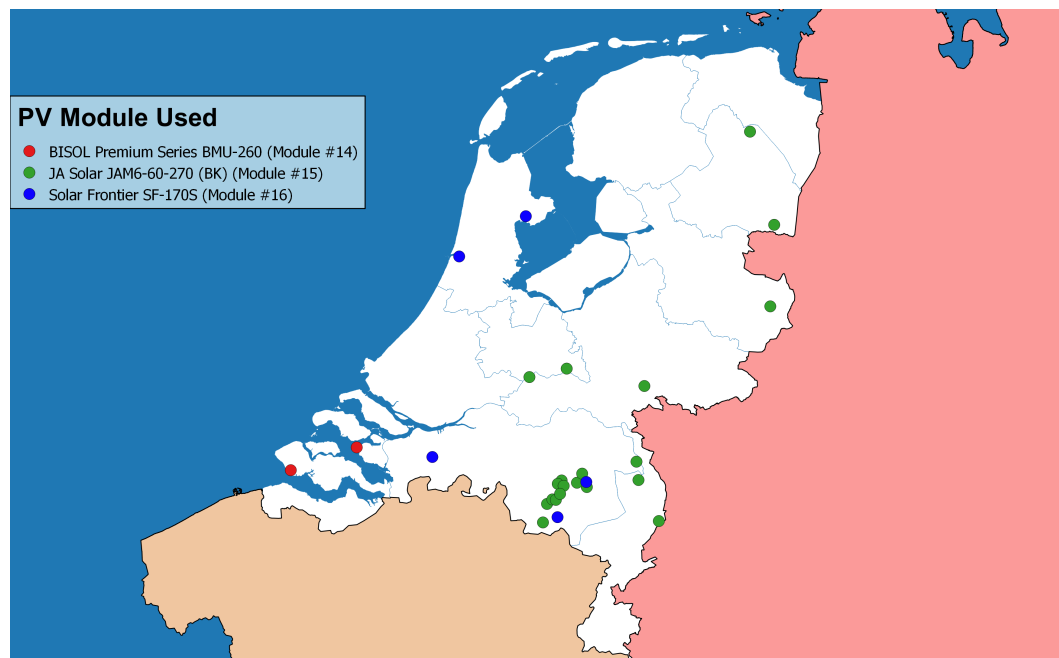


Figure 6.1: Location of PV systems studied in this chapter. The module number in the figure refer to the serial number of PV modules presented in Table 2.1.

For all of the 27 PV systems, a number of data such as latitude, longitude, module tilt, array orientation, PV module used, installed peak power, measured annual AC yield and the inverter used in the systems were provided by Solar Monkey B.V. The systems were monitored during different time periods, however, data pertaining to a period of one year was studied. Although this thesis is strictly concerned with the power output of the PV array and not the entire PV system, due to the lack of measured DC yield data, the PR was calculated for the AC output of the system. Along with the losses in the module level, this will also reflect the losses pertaining to DC to AC conversion of the system. However, since almost all of these systems use similar inverters by the same manufacturer, the ratio of the annual AC and DC yields of the systems can be alike making the AC performance ratio a comparable indicator for the PV module's performance. Table 6.1 presents the provided data in detail.

Table 6.1: Detailed specification along with measured annual AC yield of the PV systems. The numbers in parentheses following the tilt/orientation refer to the total number of PV modules in the array tilted/oriented at the given angle. The AC yield was measured for a period of one year within the years 2016 and 2017.

S. No.	Location	PV module	Installed peak power (kW _p)	Electrical configuration	Module tilt (°)	Module orientation (°)	Inverter	Measured AC yield (kWh/year)
1	Tholen	BISOL Premium Series BMU-260	4.42	10×1, 7×1	45	200(10), 207(7)	SolarEdge SE5K-3phase	4361.69
2	Vlissingen	BISOL Premium Series BMU-260	2.34	9×1	13	182	SolarEdge SE2200 1-phase HD-W	2012.48
3	Duiven	JA Solar JAM6-60-270 (BK)	3.78	14×1	35	116	SolarEdge SE3500	2947.63
4	Oldenzaal	JA Solar JAM6-60-270 (BK)	6.21	23×1	45	211	SolarEdge SE6000	5607.88
5	Son en Breugel	JA Solar JAM6-60-270 (BK)	7.29	27×1	35	161(17), 153(10)	SolarEdge SE7k 3-phase GSM	6821.37
6	Venray	JA Solar JAM6-60-270 (BK)	3.78	14×1	35	192	SolarEdge SE3500	3521.51
7	Eindhoven	JA Solar JAM6-60-270 (BK)	2.70	10×1	35	262	SolarEdge SE1400	2267.86
8	Veldhoven	JA Solar JAM6-60-270 (BK)	5.94	22×1	40	222	SolarEdge SE5000	5328.6
9	Boxmeer	JA Solar JAM6-60-270 (BK)	7.83	29×1	45	152(6), 242(23)	SolarEdge SE7k 3-phase GSM	6767.11
10	Helmond	JA Solar JAM6-60-270 (BK)	3.78	14×1	40	268	SolarEdge SE3500	2959.16
11	Veldhoven	JA Solar JAM6-60-270 (BK)	4.86	18×1	8(8), 40(4), 10(6)	155	SolarEdge SE5000	4309.65
12	Venlo	JA Solar JAM6-60-270 (BK)	3.24	12×1	35	231	SolarEdge SE3000	2863.33
13	Bergeijk	JA Solar JAM6-60-270 (BK)	3.78	14×1	35	244	SolarEdge SE3500	3051.75
14	Emmen	JA Solar JAM6-60-270 (BK)	5.94	22×1	35	231	SolarEdge SE5000	5210.41
15	Laarbeek	JA Solar JAM6-60-270 (BK)	11.07	41×1	35	228	SolarEdge SE10k 3-phase GSM	9137.70
16	Utrechtse Heuvelrug	JA Solar JAM6-60-270 (BK)	4.86	18×1	35	116	SolarEdge SE5000	4223.19
17	Zuidlaren	JA Solar JAM6-60-270 (BK)	5.40	20×1	10	163	SolarEdge SE5000	4773.92
18	Eindhoven	JA Solar JAM6-60-270 (BK)	3.78	14×1	35(7), 10(7)	166	SolarEdge SE3500	3076.93
19	Culemborg	JA Solar JAM6-60-270 (BK)	5.94	16×1, 6×1	35	95(16), 175(6)	SolarEdge SE5000	4949.40
20	Beek en Donk	JA Solar JAM6-60-270 (BK)	4.32	10×1, 6×1	10(6), 40(10)	236	SolarEdge SE4000	3714.68
21	Eindhoven	JA Solar JAM6-60-270 (BK)	3.51	13×1	15(2), 35(11)	91(5), 271(8)	SolarEdge SE3500	2595.68
22	Eindhoven	JA Solar JAM6-60-270 (BK)	2.16	8×1	29	152	SolarEdge SE2200 1-phase HD-W	1884.05
23	Laarbeek	Solar Frontier SF-170S	5.44	32×1	35	179	SolarEdge SE5K-3phase	4509.39
24	Boschenhoofd	Solar Frontier SF-170S	4.08	12×1, 12×1	37	192	Goodwe 4600DS, S	3664.40
25	Velsen-Zuid	Solar Frontier SF-170S	1.70	10×1	43	182	SolarEdge SE2200 1-phase	1869.53
26	Hoorn	Solar Frontier SF-170S	3.57	21×1	55	149	SolarEdge SE3000	3141.03
27	Valkenswaard	Solar Frontier SF-170S	4.08	24×1	10(10), 55(14)	204(10), 207(14)	SolarEdge SE4000	3804.86

Furthermore, to compute the *PR* of the systems, it is important to estimate the POA irradiation. To do so, it is first necessary to calculate the solar irradiation data for all the locations. Therefore, the interpolation and irradiance techniques discussed in the previous chapters were utilized here. For each location, hourly GHI data measured by weather stations within 50 kms was first interpolated using IDW method. The GHI value thus obtained was then decomposed into DNI and DHI using the BRL model. The data was calculated for a period of one year beginning from the date of starting of the systems. An example of it is shown in the figure below.

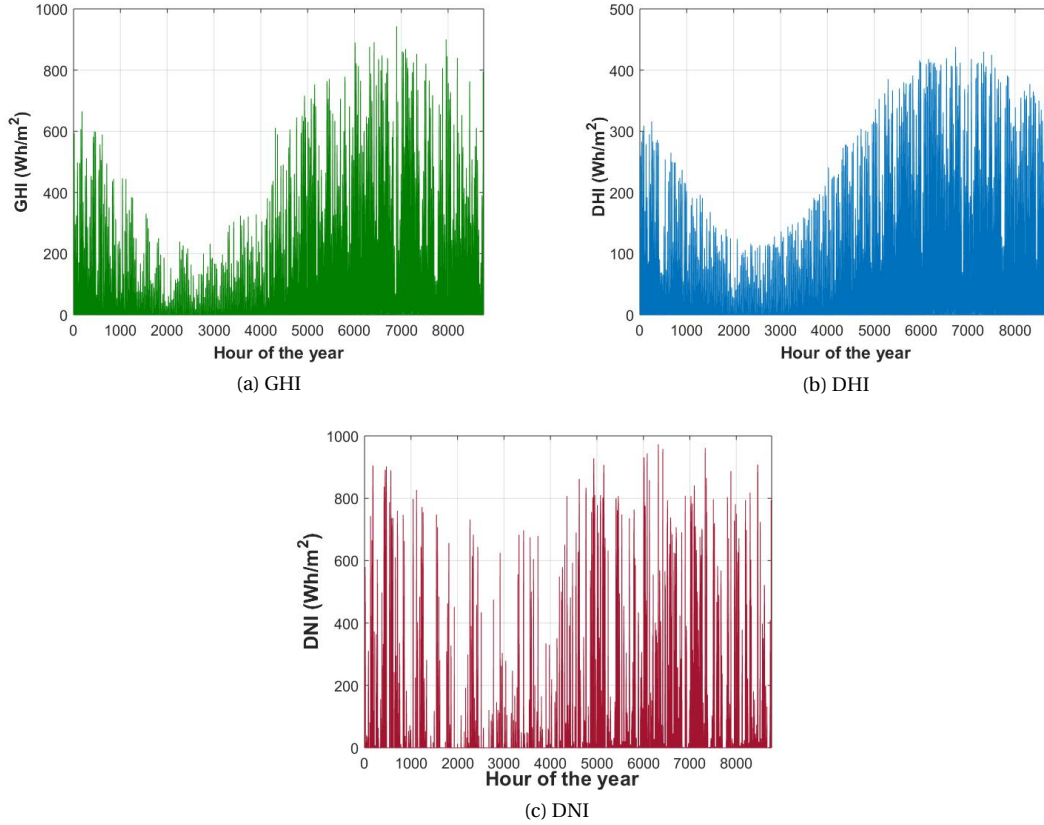


Figure 6.2: Decomposed DNI and DHI along with interpolated GHI values for a PV system installed in Eindhoven (PV system #7), The Netherlands (51.49 °N, 5.45 °E) from 10/09/2016 to 09/09/2017.

However, the irradiation estimate shown in the figure above will only be received by a PV array if the skyline is free of obstacles. Generally, this is not the case for rooftop installations. Therefore, the skyline profile of all of the systems was also analyzed to calculate the shading factor (SF). Figure 6.3 shows a binary image of the surrounding obstacles for one of the systems.

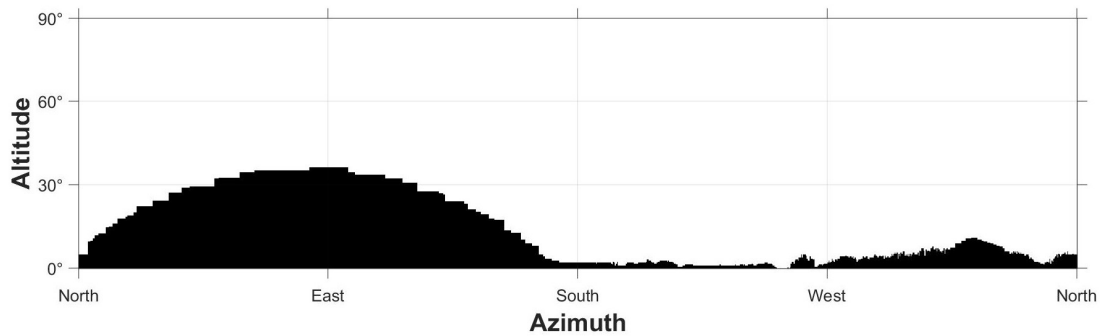


Figure 6.3: Skyline profile for the PV system installed in Eindhoven, The Netherlands (PV system #7).

SF was calculated by estimating the position of the Sun for every hour throughout the year. On every instance when the Sun position overlapped with an obstacle, SF is set to zero. Otherwise, it is equal to one. Then, the DNI value was multiplied with SF and the GHI was set equal to DHI for instances where SF was zero. To calculate the Sun position, the altitude was calculated using the method explained in 4.3.1. Similarly, the azimuth of the Sun was calculated using the following equation [6],

$$\tan(A_S) = \frac{-\sin(\theta_L) \cdot \cos(\lambda_S) + \cos(\theta_L) \cdot \cos(\epsilon) \cdot \sin(\lambda_S)}{-\sin(\phi_0) \cdot \cos(\theta_L) \cdot \cos(\lambda_S) - [\sin(\phi_0) \cdot \sin(\theta_L) \cdot \cos(\epsilon) - \cos(\phi_0) \cdot \sin(\epsilon)] \cdot \sin \lambda_S} \quad (6.4)$$

where A_S represents the azimuth of the Sun in degrees. The value of A_S ranges from 0° - 360° where 0° represents North. Now, the effective GHI, DNI and DHI received by the PV array can be easily calculated using the Shading Factor. Figure 6.4 shows the calculation of the hourly SF taking the skyline profile and the analemma of the Sun for every hour into account.¹

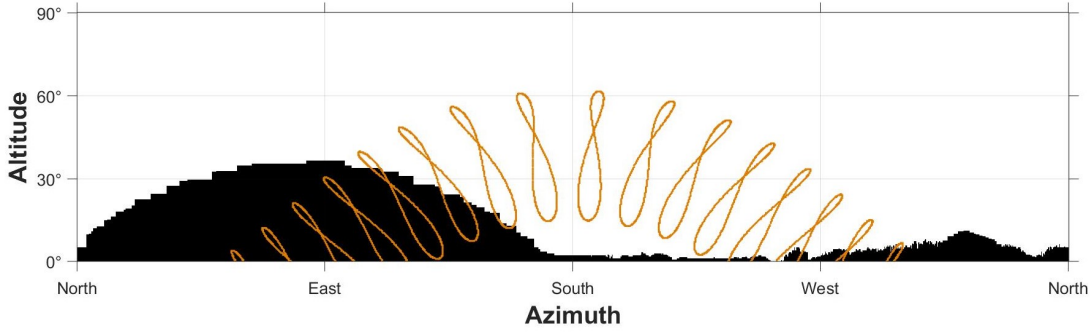


Figure 6.4: Calculation of hourly SF for the PV system installed in Eindhoven, The Netherlands (PV system #7).

6.3. Modeling of irradiance on a tilted surface

The in-plane irradiance (G_{POA}) received by a tilted surface constitutes of three different components. It can be expressed analytically as,

$$G_{POA} = G_{dir} + G_{dif} + G_{ground} \quad (6.5)$$

where G_{dir} (W/m^2) is the direct irradiance on the surface. G_{dif} (W/m^2) represents the diffuse component. Finally, G_{ground} (W/m^2) is the component of irradiance received by the surface that is reflected from the ground or surrounding obstacles.

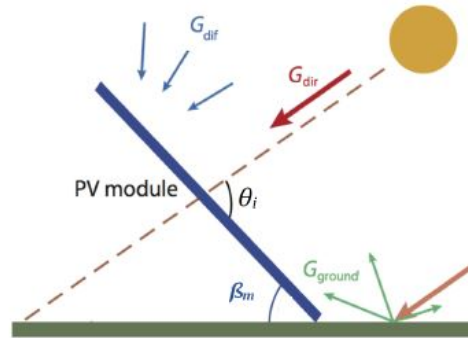


Figure 6.5: The three components of irradiance on a tilted surface [6].

6.3.1. Direct beam component

The direct beam component received by a tilted surface depends on the tilt and azimuth angles of the tilted surface as well as the altitude and azimuth of the Sun. It can be calculated using the following equation [6],

$$G_{dir} = DNI \times [\cos(a_M) \cdot \cos(a_S) \cdot \cos(A_M - A_S) + \sin(a_M) \cdot \sin(a_S)] \quad (6.6)$$

where a_S and A_S represent the altitude and azimuth angles of the Sun. A_M is the azimuth angle of the tilted surface. a_M is the angle between the projection of the normal of the tilted surface onto the horizontal plane and due North. It can be calculated as,

$$a_M = 90^\circ - \beta_M \quad (6.7)$$

¹Analemma is a plot that reflects the variation in the Sun's position in the sky for a given time over a year with respect to its altitude and azimuth.

where β_M is the angle at which the surface is tilted from the horizontal plane. In equation 6.6, the term within the parentheses represents the cosine of the Angle of Incidence (AOI).² Moreover, equation 6.6 is only valid when $\alpha_S > 0$ and A_S is within $\pm 90^\circ$ of A_M . G_{dir} is set to zero in all the other cases.

6.3.2. Diffuse component

The diffuse component of the irradiance on a tilted surface is dependent on various factors such as cloud cover, cloud movement, etc. due to which the spatial distribution of the diffuse component is random and unknown [86]. Hence, because of this randomness in its spatial distribution as well as its time dependency, it is quite difficult to model it [86]. Modeling of the diffuse irradiance makes use of its three sub-components: circumsolar, horizon brightening and isotropic diffuse irradiance. However, the number of the sub-components taken into consideration depends on the model used. Figure 6.6 illustrates these sub-components of the diffuse irradiance that are explained in the following paragraph.

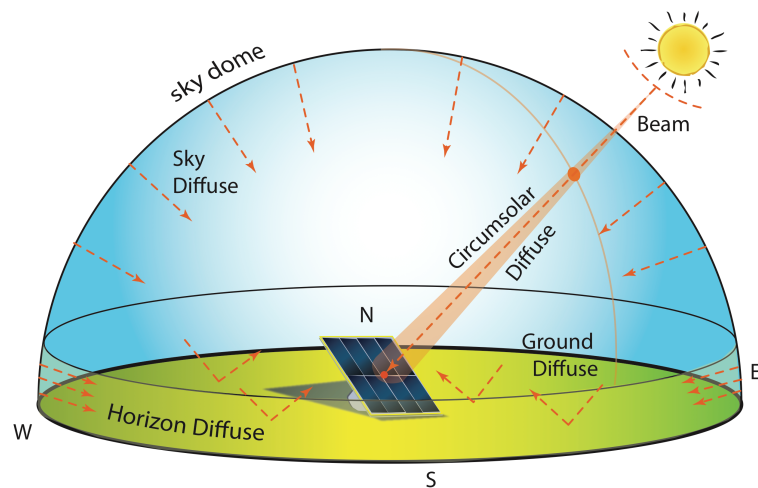


Figure 6.6: Sub-components of diffuse irradiance [87].

Circumsolar irradiance is the forward scattering of the beam irradiance due to the aerosols present in the atmosphere. Moreover, as a result of multiple internal reflections within the Earth's atmosphere as well as the scattering of a substantial portion of the incident irradiance due to the longer path length of atmosphere near the horizon, there is an increase in diffuse irradiance near the horizon during sunset or sunrise [86]. This is known as horizon brightening. In the above figure, this is referred as horizon diffuse. The isotropic sub-component refers to the rest of the diffuse irradiance that is assumed to be uniformly distributed over the sky dome. It is referred as sky diffuse in the above figure.

Irradiance transposition models mostly use these sub-components to estimate the diffuse component of the POA irradiance. The simplest of these models is the isotropic model that only considers the isotropic sub-component assuming that the diffuse irradiance is uniformly distributed over the sky dome [86]. This model is more accurate for cloudy skies, however, it leads to more errors for clear skies as the effects of circumsolar and horizon brightening sub-components increase. *Hay and Davies* further extended this model by introducing an 'anisotropy index' that weighs part of the diffuse irradiance as circumsolar and the rest of it as isotropic [88]. Furthermore, *Reindl et al.* included an additional term to account for the horizon brightening that has a dominant effect during sunset and sunrise [86]. The Perez model is a computationally intensive model that uses empirically derived coefficients to perform a detailed analysis of the isotropic, circumsolar and horizon brightening sub-components [89]. The Sandia model includes an empirically derived term for the circumsolar and horizon brightening to the isotropic model [90]. Finally, *Olmo et al.* had introduced a model to calculate the POA irradiance using measured GHI values, clearness index and solar elevation [91]. In this model, one does not need to decompose the GHI values to DNI and DHI or model the three components of POA irradiance separately.

²AOI is the angle between the surface normal and the incident direction of the sunlight.

In this thesis, it was not possible to analyze the validity of these models due to the lack of measured POA irradiance data. Therefore, an optimal model for The Netherlands was chosen based on results provided in literature. *van Sark et al.* had used the Olmo model to predict the POA irradiance for The Netherlands citing that the error between the experimental and predicted values were less for this model [92]. However, no concrete error analysis of the model was presented. *Jamodkar* had compared five different transposition models for an e-bike charging station in Delft, The Netherlands and found that Reindl and Hay/Davies methods were best suited for the climate of The Netherlands [83]. Among these two models, Reindl model is often found to perform better and therefore, it was selected to estimate the diffuse component of the POA irradiance for all of the 27 locations [86, 93, 94]. Calculation of the diffuse component using Reindl model is explained next.

Reindl Model:

As discussed previously, the Reindl model considers all three sub-components of the diffuse irradiance. It incorporates a correction factor for the horizon brightening diffuse irradiance with the isotropic term of the Hay/Davies model. The mathematical expression for the Hay/Davies model is first presented where the first term represents the isotropic sub-component and the second term signifies the contribution of circumsolar diffuse irradiance [88].

$$G_{dif,H} = G_{dif,iso} + G_{dif,cs} = DHI \times \left[(1 - A_I) \times SVF + A_I \cdot R_b \right] \quad (6.8)$$

where A_I is the anisotropy index, SVF is the Sky View Factor and R_b is the geometric factor. A_I helps define the isotropic and circumsolar components of the diffuse irradiance. It can be calculated using the following two equations [88],

$$I_b = GHI - DHI \quad (6.9)$$

$$A_I = \frac{I_b}{E_a} \quad (6.10)$$

where I_b is the direct horizontal irradiance and E_a is the extraterrestrial irradiance outside the Earth's atmosphere. Next, SVF is the fraction of sky visible from the tilted surface. It is a function of the tilt angle of the surface (β_M) [6].

$$SVF = \frac{1 + \cos(\beta_M)}{2} \quad (6.11)$$

The geometric factor (R_b) is the ratio of the direct beam component (G_{dir}) on the tilted surface and DNI [88].

$$R_b = \frac{G_{dir}}{DNI} \quad (6.12)$$

Equation 6.13 represents the Reindl model that includes an additional term for horizon brightening correction applied to the isotropic term [86].

$$G_{dif,Re} = DHI \times \left[(1 - A_I) \times SVF \times \left(1 + f \cdot \sin^3 \left(\frac{\beta_M}{2} \right) \right) + A_I \cdot R_b \right] \quad (6.13)$$

where f is the modulating function that is used to define the isotropic diffuse irradiance corrected to horizon brightening. It is given by the following equation [86],

$$f = \sqrt{\frac{I_b}{GHI}} \quad (6.14)$$

In equation 6.13, the first term represents the isotropic sub-component corrected to horizon brightening whereas the second term represents the circumsolar diffuse irradiance. From equations 6.10 and 6.14, it can be seen that under cloudy conditions, A_I and f reduce to zero since I_b is zero. This reverts the Reindl model to the isotropic transposition model. The anisotropy index and the modulating function are non-zero for partly cloudy or clear skies.

6.3.3. Ground reflected component

This component of the POA irradiance is heavily influenced by the reflectivity of ground, immediate surrounding of the tilted surface and the tilt angle. The contribution of the ground reflected component becomes more profound when the surrounding objects are highly reflective such as snow or glass covered buildings. It is generally calculated by assuming a free horizon and the forefront of the field of view of the tilted surface as a diffuse reflector [86]. The general equation for it is given by [6],

$$G_{ground} = GHI \times \rho \times (1 - SVF) = GHI \times \rho \times \left(\frac{1 - \cos(\beta_M)}{2} \right) \quad (6.15)$$

where ρ is the albedo of the ground. It is the ratio of the ground reflected irradiance to the GHI [95]. In this work, it was not possible to determine the albedo value of the ground for every PV system. Since, the PV systems being studied are rooftop installations, it was assumed that the surface on which the systems were mounted consisted of roof tiles that generally have an albedo range of 0.10-0.35 [95]. Therefore, the value of ρ was taken as 0.2 for every system. Moreover, the contribution of the irradiance reflected from the nearby surrounding was not investigated and therefore, it is not included in the calculation of the POA irradiance.

Now, the hourly POA irradiation can be estimated by substituting the values obtained for equations 6.6, 6.13 and 6.15 for every hour in equation 6.5. Finally, the annual POA irradiation in kWh/m² can be estimated by summing the hourly values for G_{POA} . Figure below shows the hourly POA irradiation calculated for PV system #7 from Table 6.1 where the annual POA irradiation was found to be 941 kWh/m². The same method was carried out for the rest of the PV systems as well.

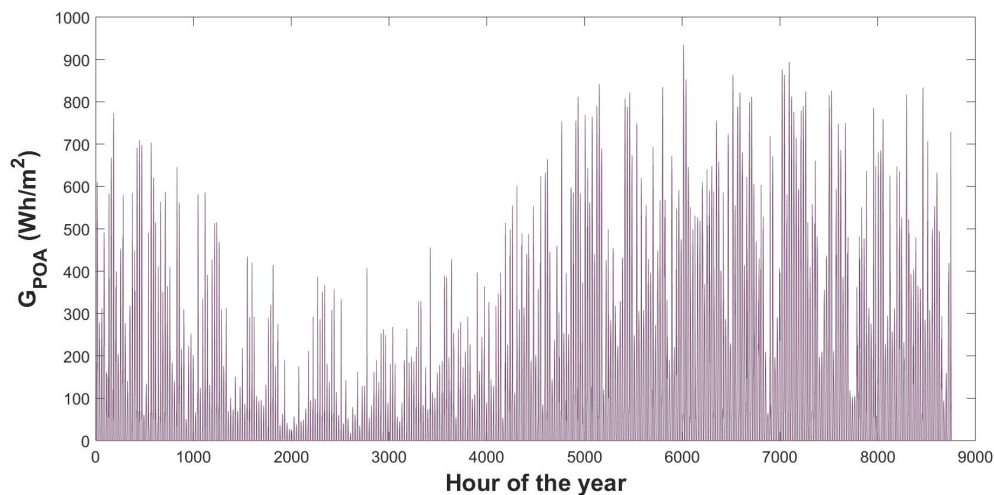


Figure 6.7: Estimated hourly POA irradiance for the PV system installed in Eindhoven, The Netherlands (PV system #7).

6.4. Evaluation of PV systems

As discussed previously, performance parameters such as PR make it possible to distinguish the performance of PV systems that are installed in different locations as well as have different specifications. Therefore, in this section the annual AC performance ratio of the 27 PV systems shown in Table 6.1 is evaluated and compared. This was done by applying equation 6.3 to all of the PV systems. The parameters P_0 and annual AC yield of these systems are mentioned in Table 6.1. The annual POA irradiation received by the PV array was estimated by the approach described in the previous section. Figure below shows the estimated annual AC performance ratio of the 27 PV systems.

As can be seen from figure 6.8, it was found that there was significant variation in the performance ratio of the PV systems. A few of the PV systems (System #8, #16, #23, #25 and #27) showed unusually high AC performance ratios. Although performance ratios of greater than 0.90 can be achieved, the values obtained for the above systems were quite unrealistic for today's technology [3]. One of the reasons for it could be the underestimation of the POA irradiation due to the uncertainties involved with the different models used in every step of the process. Moreover, inaccuracy in the skyline profile can further aggravate it. The high AC

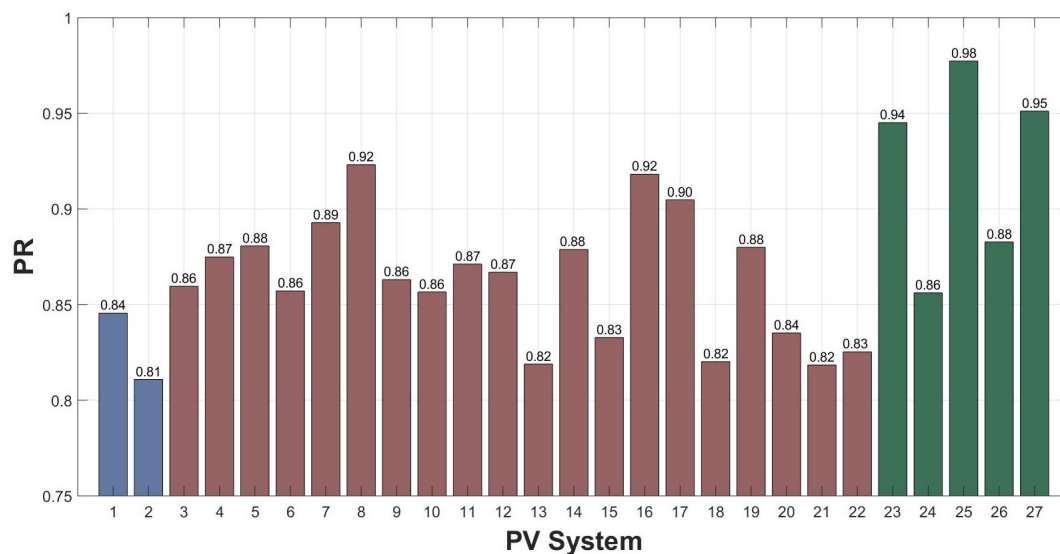


Figure 6.8: Performance ratio of PV systems. The x-ticks in the figure denote the serial number of the PV systems as presented in Table 6.1. Bars with the same color indicate that the systems use same PV module/technology (blue = poly c-Si, red = mono c-Si and green = CIS).

performance ratio could also be due to inaccuracies involved with the measurement of the yield of the system. PV system #25 had a surprisingly high value of final PV system yield (Y_f) at 1099.72 kWh/kW_p. Nevertheless, the average AC performance ratio for systems using poly c-Si (Module #14), mono c-Si (Module #15) and CIS (Module #16) technologies was found to be 0.83, 0.86 and 0.92, respectively.

6.5. Coherence of selection map

As initially suggested by the PV selection map, it was found that among the PV systems studied, the systems using CIGS technology presented the highest performance ratio on an average. Moreover, since the number of systems using poly c-Si module was much less, it was not possible to precisely compare the PV systems. However, it is expected that the performance of a poly c-Si module would be similar to that of a mono c-Si module due to their comparable values for ST and γ .

Based on the results obtained, it cannot be firmly concluded that the CIGS technology will always perform the best in The Netherlands. This is mainly due to the uncertainties involved with the modeling of the POA irradiation as well as the measurement of the actual yield. The estimation of the POA irradiation was carried out in three different steps namely, interpolation, decomposition and transposition of solar irradiation data which may have resulted in high amount of error for some systems. As stated previously, the PR of a few systems was found to be unusually high which could be due to underestimation of the POA irradiation. Furthermore, there could be instances where the POA irradiation is overestimated, however, such cases are harder to detect since the lower value of PR could also be due to the system performing poorly.

In summary, the results obtained showed that the PV systems using CIGS technology resulted in higher performance ratios on an average. The foundation of the PV selection map is based on probability theories and keeping the results obtained in mind, it can be said that CIGS technology would probably lead to higher performance ratios in The Netherlands when compared to other PV technologies. Similar analysis performed with measured solar irradiation data would lead to precise outcomes to draw a definite conclusion. Moreover, estimation of DC performance ratio using measured DC yield would help provide a more accurate picture for the performance of different PV technologies in The Netherlands.

Conclusions & Recommendations

7.1. Conclusions

In this thesis, a number of research questions were formulated and investigated with the aim of creating a PV selection map for the design of a PV system. Several experiments were carried out to study the influence of ambient temperature on Shading Tolerability (ST). Consequently, a selection map for the installation of PV modules was presented based on ST and temperature coefficient for maximum power of different PV modules. Furthermore, using a suitable interpolation technique, the optimal PV technology for PV systems installed in The Netherlands was determined with reference to the PV selection map. Finally, different irradiance decomposition and transposition models were studied to assess the validity of the selection map by analyzing the performance of different existing PV systems installed in The Netherlands. A brief summary of the conclusions derived by resolving the research questions that were instigated in the first chapter are discussed in this section.

1. Is the parameter Shading Tolerability an intrinsic property of a PV module?

It was found that %ST exhibited a slightly increasing trend with ambient temperature. This was mainly due to the decreased temperature effect on a PV module's power output during partial shading. Nevertheless, the change in ST was negligible with an average increment of 0.07 %ST/°C for the four different PV modules that were tested. Therefore, the parameter ST was found to be almost independent of the ambient temperature which enables us to treat it as an intrinsic property of a PV module.

2. Can PV modules be categorized for certain climatic conditions based on their Shading Tolerability and temperature coefficient for maximum power (γ)?

Yes, PV modules can be classified for a given climatic condition simply by knowing their technical specifications. First, three different shade classes namely, sunny, partly cloudy and cloudy, were introduced by applying LSVM algorithm to the results obtained for the measurement of ST for 16 different PV modules. Again, three different temperature classes namely, hot, mild and cold, were established by studying the distribution of the temperature coefficient for maximum power of 50 different PV modules that are currently available in the market. These classes were then used as an integral attribute of the PV selection map.

3. Among the existing interpolation techniques, which is the best suited method to get detailed information of the meteorological conditions of The Netherlands?

Three different interpolation techniques: IDW, OK and RK were deemed to be the most suitable for the interpolation of temperature, cloud cover and GHI for The Netherlands based on studies carried out by several authors. The RK method that couples regression with kriged residuals was found to be the most accurate. However, since this thesis was restricted with the interpolation of annual average values, the IDW method was adopted since the involved %RMSE was less than 2.5% as well as due to the simplistic nature of the method. Nevertheless, the RK method is suggested for accurate interpolation of hourly data.

4. What are the most suitable irradiance decomposition and transposition models to accurately calculate the Plane of Array (POA) irradiance for The Netherlands?

For the estimation of the POA irradiance, six different existing irradiance decomposition models were studied first. The Dutch-I and BRL models were found to be the most accurate using the meteorological data measured by CESAR, Cabauw, The Netherlands. During this research work, the BRL model was implemented since it had the least %RMSE among the models studied as well as due to its greater accuracy under lower clearness indices. For the transposition of solar irradiance to a tilted plane, the Reindl model was found to be the most suitable model for The Netherlands based on the review of several literature studies.

5. Does the established selection map help improve the energy yield and performance ratio of a PV system?

The results obtained for the interpolation of meteorological data for The Netherlands suggested that the temperature and cloudiness conditions of the country can be classified as mild and cloudy, respectively based on the suggested meteorological classifications. As per the selection map, this would suggest that the CIGS technology is the most optimal PV technology to be installed in The Netherlands to achieve greater system performance. Hence, to verify this interpretation, a number of existing PV systems using three different PV technologies: poly c-Si, mono c-Si and CIS were studied. It was found that the CIS technology indeed presented a higher performance ratio on an average among the PV systems analyzed. Therefore, since the concept of Shading Tolerability is based on probability laws, it can be said that the selection map can help to select the optimal PV module that would most probably lead to higher energy yield and performance ratio.

Therefore, it can finally be concluded that based on the findings of this thesis, the selection map for PV installation based on Shading Tolerability and temperature coefficient can help system designers to select an optimal PV module to achieve greater system performance and energy yield. Together with careful design of a PV system, the optimal choice of a PV module can lead to higher specific energy yield and lower cost of electricity which may further accelerate the growth of the PV industry.

7.2. Recommendations

In spite of the comprehensive research carried out, there are a few improvements that can be considered to further improve the selection map. Moreover, several findings of this research work could be useful for the design of PV systems as well as future projects at the Photovoltaic Materials and Devices (PVMD) group, TU Delft. Some of these recommendations are:

- Inclusion of ST in a PV module's datasheet.
- Injection of data into the PV selection map by testing more PV modules/technologies for ST to achieve further detail in the map.
- Determination of performance ratios of existing PV systems using measured DC yield and POA irradiance to validate the selection map even more accurately.
- Extension of the validation of selection map to climate conditions other than that of The Netherlands.
- Application of Regression Kriging as an interpolation method and the BRL model as an irradiance decomposition model in the Dutch PV Portal developed by PVMD, TU Delft.
- Implementation of ST to accurately predict the energy yield of a PV system.

Bibliography

- [1] International Renewable Energy Agency, “IRENA Cost and Competitiveness Indicators: Rooftop Solar PV,” *International Renewable Energy Agency, Abu Dhabi*, 2017.
- [2] Fraunhofer Institute for Solar Energy Systems (ISE), “Photovoltaics Report,” Tech. Rep. February, 2018. [Online]. Available: www.ise.fraunhofer.de
- [3] W. van Sark, N. Reich, B. Müller, A. Armbruster, K. Kiefer, and C. Reise, “Review of PV Performance Ratio Development,” *World Renewable Energy Forum (WREF) Congress XII*, no. 6, pp. 1–6, 2012.
- [4] K. P. Bhandari, J. M. Collier, R. J. Ellingson, and D. S. Apul, “Energy payback time (EPBT) and energy return on energy invested (EROI) of solar photovoltaic systems: A systematic review and meta-analysis,” *Renewable and Sustainable Energy Reviews*, vol. 47, pp. 133–141, 2015. [Online]. Available: <http://dx.doi.org/10.1016/j.rser.2015.02.057>
- [5] M. A. Green, “General temperature dependence of solar cell performance and implications for device modelling,” *Progress in Photovoltaics: Research and Applications*, vol. 11, no. 5, pp. 333–340, 2003.
- [6] A. Smets, O. Isabella, K. Jäger, R. A. C. M. M. van Swaaij, and M. Zeman, *Solar Energy: The Physics and Engineering of Photovoltaic Conversion, Technologies and Systems*. UIT Cambridge, 2016.
- [7] O. Dupré, R. Vaillon, and M. A. Green, *Thermal Behavior of Photovoltaic Devices*. Springer, 2017. [Online]. Available: <http://link.springer.com/10.1007/978-3-319-49457-9>
- [8] T. Sarver, A. Al-Qaraghuli, and L. L. Kazmerski, “A comprehensive review of the impact of dust on the use of solar energy: History, investigations, results, literature, and mitigation approaches,” *Renewable and Sustainable Energy Reviews*, vol. 22, pp. 698–733, 2013. [Online]. Available: <http://dx.doi.org/10.1016/j.rser.2012.12.065>
- [9] M. Mani and R. Pillai, “Impact of dust on solar photovoltaic (PV) performance: Research status, challenges and recommendations,” *Renewable and Sustainable Energy Reviews*, vol. 14, no. 9, pp. 3124–3131, 2010. [Online]. Available: <http://dx.doi.org/10.1016/j.rser.2010.07.065>
- [10] M. R. Maghami, H. Hizam, C. Gomes, M. A. Radzi, M. I. Rezadad, and S. Hajighorbani, “Power loss due to soiling on solar panel: A review,” *Renewable and Sustainable Energy Reviews*, vol. 59, pp. 1307–1316, 2016. [Online]. Available: <http://dx.doi.org/10.1016/j.rser.2016.01.044>
- [11] International Electrotechnical Commission (IEC), “Photovoltaic System Performance Monitoring - Guidelines for Measurement, Data Exchange, and Analysis, IEC Standard 61724,” 1998.
- [12] First Solar Inc., Universidade Federal de Santa Catarina, and Instituto para o Desenvolvimento das Energias Alternativas na América Latina (IDEAL), “Thin-Film CdTe Photovoltaic Technology Scientific Review,” Tech. Rep., 2015. [Online]. Available: https://issuu.com/idealeco/_logicas/docs/thin-film{}_cdte{}_photovoltaic{}_technol
- [13] D. Quansah, M. Adaramola, G. Takyi, and I. Edwin, “Reliability and Degradation of Solar PV Modules—Case Study of 19-Year-Old Polycrystalline Modules in Ghana,” *Technologies*, vol. 5, no. 2, p. 22, 2017. [Online]. Available: <http://www.mdpi.com/2227-7080/5/2/22>
- [14] K. Lappalainen and S. Valkealahti, “Analysis of shading periods caused by moving clouds,” *Solar Energy*, vol. 135, pp. 188–196, 2016. [Online]. Available: <http://dx.doi.org/10.1016/j.solener.2016.05.050>
- [15] Y. J. Wang and P. C. Hsu, “An investigation on partial shading of PV modules with different connection configurations of PV cells,” *Energy*, vol. 36, no. 5, pp. 3069–3078, 2011. [Online]. Available: <http://dx.doi.org/10.1016/j.energy.2011.02.052>

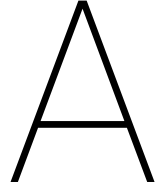
- [16] C. Crowell, "Aurora Solar remote shading assessment tool now allowed over on-site inspection by Connecticut Green Bank," 2018. [Online]. Available: <https://solarbuildermag.com/news/aurora-solar-remote-shading-assessment-tool-now-allowed-over-on-site-inspection-by-connecticut-green-bank/>
- [17] G. Reysa, "PV Power Loss Due to Snow On Panels," 2010. [Online]. Available: <https://www.builditsolar.com/Projects/PV/EnphasePV/SnowOnPV.htm>
- [18] K. Zipp, "Ultracapacitor Storage Can Help Build A Reliable Solar Grid," 2014. [Online]. Available: <https://www.solarpowerworldonline.com/2014/01/ultracapacitors-grid-scale-solar-smoothing/>
- [19] F. Lu, S. Guo, T. M. Walsh, and A. G. Aberle, "Improved PV module performance under partial shading conditions," *Energy Procedia*, vol. 33, pp. 248–255, 2013. [Online]. Available: <http://dx.doi.org/10.1016/j.egypro.2013.05.065>
- [20] P. Bauwens and J. Doutreligne, "NMOS-Based Integrated Modular Bypass for Use in Solar Systems (NIMBUS): Intelligent Bypass for Reducing Partial Shading Power Loss in Solar Panel Applications," *Energies*, vol. 9, no. 6, p. 450, 2016. [Online]. Available: <http://www.mdpi.com/1996-1073/9/6/450>
- [21] G. S. Spagnolo, P. Del Vecchio, G. Makary, D. Papalillo, and A. Martocchia, "A review of IR thermography applied to PV systems," *2012 11th International Conference on Environment and Electrical Engineering, EEEIC 2012 - Conference Proceedings*, pp. 879–884, 2012.
- [22] M. A. Munoz, M. C. Alonso-García, N. Vela, and F. Chenlo, "Early degradation of silicon PV modules and guaranty conditions," *Solar Energy*, vol. 85, no. 9, pp. 2264–2274, 2011.
- [23] A. E. Brooks, D. Cormode, A. D. Cronin, and E. Kam-Lum, "PV system power loss and module damage due to partial shade and bypass diode failure depend on cell behavior in reverse bias," *2015 IEEE 42nd Photovoltaic Specialist Conference, PVSC 2015*, 2015.
- [24] T. J. Silverman, L. Mansfield, I. Repins, and S. Kurtz, "Damage in Monolithic Thin-Film Photovoltaic Modules Due to Partial Shade," *IEEE Journal of Photovoltaics*, vol. 6, no. 5, pp. 1333–1338, 2016.
- [25] E. D. Dunlop, "Lifetime Performance of Crystalline Silicon Pv Modules," *Photovoltaic Energy Conversion, 2003. Proceedings of 3rd World Conference on*, no. Vol. 3, pp. 2927–2930, 2003. [Online]. Available: http://ieeexplore.ieee.org/xpls/abs/_all.jsp?arnumber=1305192%5Cnhttp://ieeexplore.ieee.org/stamp/stamp.jsp?tp=&arnumber=1305192&isnumber=28988
- [26] H. Ziar, M. Nouri, B. Asaei, and S. Farhangi, "Analysis of overcurrent occurrence in photovoltaic modules with overlapped by-pass diodes at partial shading," *IEEE Journal of Photovoltaics*, vol. 4, no. 2, pp. 713–721, 2014.
- [27] A. Henemann, "BIPV: Built-in solar energy," *Renewable Energy Focus*, vol. 9, no. 6 SUPPL., pp. 14,16–19, 2008. [Online]. Available: [http://dx.doi.org/10.1016/S1471-0846\(08\)70179-3](http://dx.doi.org/10.1016/S1471-0846(08)70179-3)
- [28] A. Shekhar, S. Klerks, P. Bauer, and V. Prasanth, "Solar road operating efficiency and energy yield - An integrated approach towards inductive power transfer," *Proceedings of the 31st European Photovoltaic Solar Energy Conference and Exhibition, Hamburg, 14-18 Sept., 2015; Authors version*, no. January, 2015. [Online]. Available: <https://repository.tudelft.nl/islandora/object/uuid%7B3Ab74a7682-1559-4c81-9a11-f77d1c5ac9e8>
- [29] H. S. Rauschenbach, "Electrical output of shadowed solar arrays," *IEEE Transactions on Electron Devices*, vol. 18, no. 8, pp. 483–490, 1971.
- [30] J. Feldman, S. Singer, and A. Braunstein, "Solar Cell Interconnections and The Shadow Problem," *Solar Energy*, vol. 26, pp. 419–428, 1981.
- [31] SolarEdge, "Technical Note SolarEdge Fixed String Voltage , Concept of Operation," pp. 7–9, 2012.
- [32] E. Suryanto Hasyim, S. R. Wenham, and M. A. Green, "Shadow tolerance of modules incorporating integral bypass diode solar cells," *Solar Cells*, vol. 19, no. 2, pp. 109–122, 1986.
- [33] G. Acciari, D. Graci, and A. La Scala, "Higher PV module efficiency by a novel CBS bypass," *IEEE Transactions on Power Electronics*, vol. 26, no. 5, pp. 1333–1336, 2011.

- [34] BP Solar, "IntegraBus increases reliability of new BP Solar module," *Photovoltaics Bulletin*, vol. 2003, no. 11, p. 6, 2003. [Online]. Available: <http://www.sciencedirect.com/science/article/pii/S1473832503011180>
- [35] Global Solar Energy Inc., "Hanergy PowerFLEX™ BIPV - 90/100/185/200/275/300W."
- [36] First Solar Inc., "First Solar Series 6™ - Next Generation Thin Film Solar Technology," p. 2, 2017. [Online]. Available: <http://www.firstsolar.com/>
- [37] United Solar Ovonic, "Uni-Solar PowerBond ePVL - Technical Datasheet," 2011.
- [38] Stion Corporation, "CIGS Thin-Film Solar Modules - STN-135 / STN-140 / STN-145 / STN-150 Solar Modules," 2012.
- [39] H. Ziar, B. Asaei, S. Farhangi, M. Korevaar, O. Isabella, and M. Zeman, "Quantification of Shading Tolerability for Photovoltaic Modules," *IEEE Journal of Photovoltaics*, vol. 7, no. 5, pp. 1–10, 2017.
- [40] G. Parmigiani and L. Inoue, *Decision Theory: Principles and Approaches*. Wiley, 2009. [Online]. Available: <http://books.google.com/books?id=mnjGCYqWj7EC&pgis=1>
- [41] S. Silvestre, A. Boronat, and A. Chouder, "Study of bypass diodes configuration on PV modules," *Applied Energy*, vol. 86, no. 9, pp. 1632–1640, 2009. [Online]. Available: <http://dx.doi.org/10.1016/j.apenergy.2009.01.020>
- [42] R. Gottschalg, T. R. Betts, A. Eeles, S. R. Williams, and J. Zhu, "Influences on the energy delivery of thin film photovoltaic modules," *Solar Energy Materials and Solar Cells*, vol. 119, pp. 169–180, 2013.
- [43] Energies Nouvelles (EDF), "Centrale photovoltaïque BA 136 Toul-Rosières une construction exemplaire," Tech. Rep., 2011.
- [44] Power Technology, "Templin Solar Power Plant," 2018. [Online]. Available: <https://www.power-technology.com/projects/templin-solar-power-plant/>
- [45] World Weather Organization, "Definition of Oktas," 2018. [Online]. Available: <https://worldweather.wmo.int/oktas.htm>
- [46] M. Belda, E. Holtanová, T. Halenka, and J. Kalvová, "Climate classification revisited: From Köppen to Trewartha," *Climate Research*, vol. 59, no. 1, pp. 1–13, 2014.
- [47] E. C. Gouvêa, P. M. Sobrinho, and T. M. Souza, "Spectral Response of Polycrystalline Silicon Photovoltaic Cells under Real-Use Conditions," *Energies*, vol. 10, no. 8, p. 1178, 2017. [Online]. Available: <http://www.mdpi.com/1996-1073/10/8/1178>
- [48] R. Gottschalg, D. G. Infield, and M. J. Kearney, "Experimental study of variations of the solar spectrum of relevance to thin film solar cells," *Solar Energy Materials and Solar Cells*, vol. 79, no. 4, pp. 527–537, 2003.
- [49] R. Gottschalg, T. R. Betts, D. G. Infield, and M. J. Kearney, "The effect of spectral variations on the performance parameters of single and double junction amorphous silicon solar cells," *Solar Energy Materials and Solar Cells*, vol. 85, no. 3, pp. 415–428, 2005.
- [50] KNMI, "KNMI DataCentrum," 2018. [Online]. Available: <https://data.knmi.nl/datasets>
- [51] DWD, "Climate Data Center (CDC)," 2018. [Online]. Available: https://www.dwd.de/EN/climate/_environment/cdc/cdc_node.html
- [52] KMI, "Climate Data," 2018.
- [53] R. E. Huschke, *Glossary of Meteorology: Cloud Cover*. American Meteorological Society, 1970. [Online]. Available: http://glossary.ametsoc.org/wiki/Cloud_cover
- [54] C. Simolo, M. Brunetti, M. Maugeri, and T. Nanni, "Improving estimation of missing values in daily precipitation series by a probability density function-preserving approach," *International Journal of Climatology*, vol. 30, no. 10, pp. 1564–1576, 2010.

- [55] A. di Piazza, F. L. Conti, L. V. Noto, F. Viola, and G. La Loggia, "Comparative analysis of different techniques for spatial interpolation of rainfall data to create a serially complete monthly time series of precipitation for Sicily, Italy," *International Journal of Applied Earth Observation and Geoinformation*, vol. 13, no. 3, pp. 396–408, 2011. [Online]. Available: <http://dx.doi.org/10.1016/j.jag.2011.01.005>
- [56] W. Y. Tang, A. H. M. Kassim, and S. H. Abubakar, "Comparative studies of various missing data treatment methods - Malaysian experience," *Atmospheric Research*, vol. 42, no. 14, pp. 247–262, 1996.
- [57] D. Joly, T. Brossard, H. Cardot, J. Cavailles, M. Hilal, and P. Wavresky, "Temperature interpolation based on local information: The example of France," *International Journal of Climatology*, vol. 31, no. 14, pp. 2141–2153, 2011.
- [58] ESRI, "How inverse distance weighted interpolation works," 2012. [Online]. Available: <http://desktop.arcgis.com/en/arcmap/10.3/tools/3d-analyst-toolbox/idw.htm>
- [59] D. F. Watson and G. M. Philip, "A refinement of inverse distance weighted interpolation," *Geo-Processing* 2, pp. 315–327, 1985.
- [60] ESRI, "How Kriging works," 2012. [Online]. Available: <http://desktop.arcgis.com/en/arcmap/10.3/tools/3d-analyst-toolbox/how-kriging-works.htm>
- [61] H. Chai, W. Cheng, C. Zhou, X. Chen, X. Ma, and S. Zhao, "Analysis and comparison of spatial interpolation methods for temperature data in Xinjiang Uygur Autonomous Region, China," *Natural Science*, vol. 3, no. 12, pp. 999–1010, 2011.
- [62] P. A. Bostan, G. B. Heuvelink, and S. Z. Akyurek, "Comparison of regression and kriging techniques for mapping the average annual precipitation of Turkey," *International Journal of Applied Earth Observation and Geoinformation*, vol. 19, no. 1, pp. 115–126, 2012. [Online]. Available: <http://dx.doi.org/10.1016/j.jag.2012.04.010>
- [63] The World Factbook, "Country Comparison: Area," 2018. [Online]. Available: <https://www.cia.gov/library/publications/the-world-factbook/rankorder/2147rank.html>
- [64] Adviesdienst Geo-informatie en ICT Rijkswaterstaat, "Actueel Hoogtebestand Nederland (AHN) met relief-schaduwwerking," 2018. [Online]. Available: <http://i.imgur.com/ErTzE.jpg>
- [65] V. Schepel, "The Dutch PV Portal 2.0," MSc. thesis, TU Delft, 2018.
- [66] C. Veness, "Calculate distance, bearing and more between Latitude/Longitude points," 2012. [Online]. Available: <https://www.movable-type.co.uk/scripts/latlong.html>
- [67] Z. Jin, W. Yezheng, and Y. Gang, "General formula for estimation of monthly average daily global solar radiation in China," *Energy Conversion and Management*, vol. 46, no. 2, pp. 257–268, 2005.
- [68] B. Utsaoglu, H. K. Cigizoglu, and M. Karaca, "Forecast of daily mean, maximum and minimum temperature time series by three artificial neural network methods," *Meteorological Applications*, vol. 114, no. July, pp. 103–114, 2008.
- [69] Renewable Resource Atlas, "Solar Resource Concepts," 2018. [Online]. Available: <https://rratlas.energy.gov.sa/RRMMPublicPortal/sites/default/files/HowtoReadLiveGraph.htm>
- [70] Kipp & Zonen, "What is a Solar Monitoring Station?" 2014. [Online]. Available: <http://www.kippzonen.com/News/489/What-is-a-Solar-Monitoring-Station{#}.Ws6sX4jFKUk>
- [71] M. Iqbal, *An Introduction to Solar Radiation*. Academic Press, 1983.
- [72] T. E. Boukelia, M. S. Mecibah, and I. E. Meliche, "Estimation the DNI from global and diffuse horizontal irradiance for Algeria," *3rd International Symposium on Environment Friendly Energies and Applications, EFEA 2014*, 2014.
- [73] WRMC-BSRN, "World Radiation Monitoring Center - Baseline Surface Radiation Network," 2018. [Online]. Available: <http://bsrn.awi.de/>

- [74] D. Reindl, W. Beckman, and J. Duffie, "Diffuse fraction correlations," *Solar Energy*, vol. 45, no. 1, pp. 1–7, 1990.
- [75] A. Skartveit, J. A. Olseth, and M. E. Tuft, "An hourly diffuse fraction model with correction for variability and surface albedo," *Solar Energy*, vol. 63, no. 3, pp. 173–183, 1998.
- [76] S. Dervishi and A. Mahdavi, "Computing diffuse fraction of global horizontal solar radiation: A model comparison," *Solar Energy*, vol. 86, no. 6, pp. 1796–1802, 2012. [Online]. Available: <http://dx.doi.org/10.1016/j.solener.2012.03.008>
- [77] D. G. Erbs, S. A. Klein, and J. A. Duffie, "Estimation of the diffuse radiation fraction for hourly, daily and monthly-average global radiation," *Solar Energy*, vol. 28, no. 4, pp. 293–302, 1982.
- [78] B. Y. Liu and R. C. Jordan, "The interrelationship and characteristic distribution of direct, diffuse and total solar radiation," *Solar Energy*, vol. 4, no. 3, pp. 1–19, 1960.
- [79] J. F. Orgill and K. G. T. Hollands, "Correlation equation for hourly diffuse radiation on a horizontal surface," *Solar Energy*, vol. 19, no. 4, pp. 357–359, 1977.
- [80] A. Skartveit and J. A. Olseth, "A model for the diffuse fraction of hourly global radiation," *Solar Energy*, vol. 38, no. 4, pp. 271–274, 1987.
- [81] E. L. Maxwell, "A quasi-physical model for converting hourly global to direct normal insolation," *Solar Energy Research Institute, USA*, no. SERI/TR-215-3087, pp. 35–46, 1987. [Online]. Available: <http://rredc.nrel.gov/solar/pubs/PDFs/TR-215-3087.pdf>
- [82] B. Ridley, J. Boland, and P. Lauret, "Modelling of diffuse solar fraction with multiple predictors," *Renewable Energy*, vol. 35, no. 2, pp. 478–483, 2010. [Online]. Available: <http://dx.doi.org/10.1016/j.renene.2009.07.018>
- [83] A. Jamodkar, "Energy Yield Prediction of Solar Powered E-Bike Charging Station," MSc. thesis, Delft University of Technology, 2017.
- [84] J. Boland, B. Ridley, and B. Brown, "Models of diffuse solar fraction," *Modeling Solar Radiation at the Earth's Surface: Recent Advances*, vol. 33, pp. 193–219, 2008.
- [85] B. Marion, J. Adelstein, K. Boyle, H. Hayden, B. Hammond, T. Fletcher, B. Canada, D. Narang, A. Kimber, L. Mitchell, G. Rich, and T. Townsend, "Performance parameters for grid-connected PV systems," *31st IEEE Photovoltaics Specialists Conference and Exhibition*, pp. 1601–1606, 2005. [Online]. Available: http://ieeexplore.ieee.org/xpls/abs/_all.jsp?arnumber=1488451
- [86] D. T. Reindl, W. A. Beckman, and J. A. Duffie, "Evaluation of hourly tilted surface radiation models," *Solar Energy*, vol. 45, no. 1, pp. 9–17, 1990.
- [87] J. R. Brownson, "Empirical correlation for estimating components of light," 2018. [Online]. Available: <https://www.e-education.psu.edu/eme810/node/683>
- [88] J. Hay and J. A. Davies, "Calculation of the solar radiation incident on an inclined surface," *Proceedings of the First Canadian Solar Radiation Data Workshop*, pp. 59–72, 1980.
- [89] R. Perez, R. Seals, P. Ineichen, R. Stewart, and D. Menicucci, "A new simplified version of the perez diffuse irradiance model for tilted surfaces," *Solar Energy*, vol. 39, no. 3, pp. 221–231, 1987.
- [90] D. L. King, W. E. Boyson, and J. A. Kratochvil, "Photovoltaic array performance model," *Sandia Report No. 2004-3535*, vol. 8, no. December, pp. 1–19, 2004. [Online]. Available: http://www.osti.gov/bridge/product.biblio.jsp?osti_id=919131
- [91] F. J. Olmo, J. Vida, I. Foyo, Y. Castro-Diez, and L. Alados-Arboledas, "Prediction of global irradiance on inclined surfaces from horizontal global irradiance," *Energy*, vol. 24, no. 8, pp. 689–704, 1999.
- [92] W. van Sark, S. Hart, M. de Jong, P. de Rijk, P. Moraitis, B. B. Kausika, and H. van der Velde, "'Counting the Sun' – a Dutch Public Awareness Campaign on PV Performance," *29th European Photovoltaic Solar Energy Conference and Exhibition*, vol. 2014, pp. 3545–3548, 2014.

-
- [93] P. G. Loutzenhiser, H. Manz, C. Felsmann, P. A. Strachan, T. Frank, and G. M. Maxwell, "Empirical validation of models to compute solar irradiance on inclined surfaces for building energy simulation," *Solar Energy*, vol. 81, no. 2, pp. 254–267, 2007.
- [94] P. Ineichen, "Global irradiance on tilted and oriented planes: model validations," *University of Geneva*, no. February, 2011.
- [95] Y. Kotak, M. Gul, T. Muneer, and S. M. Ivanova, "Investigating the Impact of Ground Albedo on the Performance of PV Systems," *CIBSE Technical Symposium*, 2015.



General Equation for Shading Tolerability

An ideal PV cell can be modeled by a current source with an anti-parallel diode. At a constant temperature, the output power of a PV cell is almost linearly proportional to the incident irradiance where each cell provides P_{cell} W at 1000 W/m^2 . Now, considering a hypothetical PV module with two PV cells connected in series and assuming that the irradiance received at each PV cell's surface has two possible values only i.e. either 0 or 1000 W/m^2 , there will be four different working conditions of the PV module as shown in figure A.1 (a).

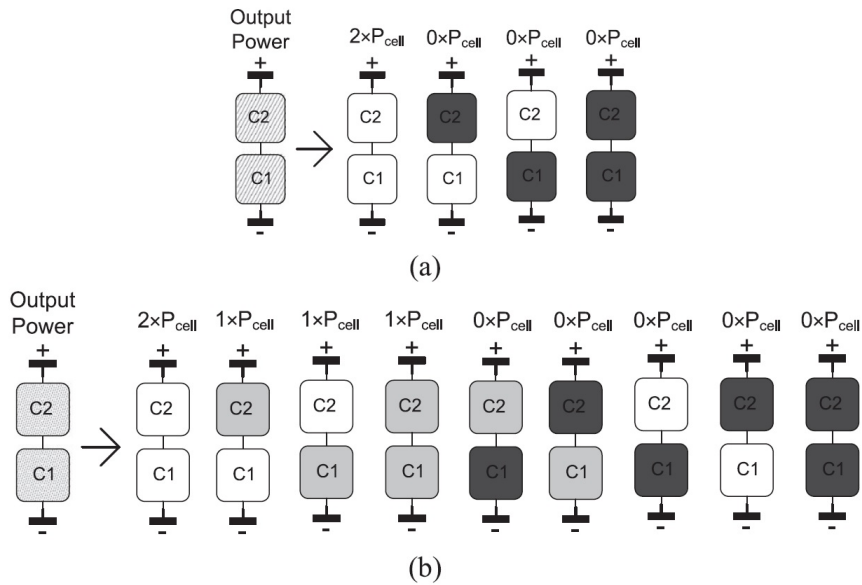


Figure A.1: Demonstration of formulation of ST: (a) PV module with two series-connected cells and two possible irradiance levels (0 and 1000 W/m^2) that leads to 2^2 working conditions. (b) PV module with two series-connected cells and three possible irradiance levels (0 , 500 and 1000 W/m^2) that results in 3^2 working conditions. The figure also shows the output power of the PV module at each working condition [39].

Since, the PV cells are modeled as ideal current source and that they are connected in series, the power output of the PV module is determined by the output of the cell that receives the lowest level of irradiance. Thus, the power output of the PV module during the four different working conditions will be $2 \times P_{cell}$, $0 \times P_{cell}$, $0 \times P_{cell}$ and $0 \times P_{cell}$. Therefore, the ST value of the PV module is given by,

$$ST_{(i=2,c=2)} = \left(\frac{1}{2^2 \times P_{cell}} \right) (2 + 0 + 0 + 0) \times P_{cell} \quad (\text{A.1})$$

Similarly, extending the above concept by increasing the irradiance levels to three (0, 500 and 1000 W/m²) while keeping the number of cells constant at two, the ST of the PV module in such a case is given by [see figure A.1 (b)],

$$ST_{(i=3,c=2)} = \left(\frac{1}{3^2 \times P_{cell}} \right) (2 + 1 + 1 + 1 + 0 + 0 + 0 + 0 + 0) \times P_{cell} \quad (A.2)$$

Hence, by following this trend, the formula for ST of a PV module with two series-connected cells is obtained as [39],

$$ST_{(i,c=2)} = \left(\frac{1}{2 \times P_{cell}} \right) \left(\frac{1}{i^2} \right) P_{cell} \left[\sum_{k=1}^j \left(\frac{2}{j} \right) k + \sum_{a=1}^{j-1} 2 \left(\frac{j-a}{j} \right) 2a \right] \quad (A.3)$$

where c is the total number of PV cells in the module and $j = i - 1$.

Now, one can obtain the formula for a PV module with three-series connected cells by following the same procedure as [39],

$$ST_{(i,c=3)} = \left(\frac{1}{3 \times P_{cell}} \right) \left(\frac{1}{i^3} \right) P_{cell} \left[\sum_{k=1}^j \left(\frac{3}{j} \right) k + \sum_{a=1}^{j-1} 3 \left(\frac{j-a}{j} \right) (3a^2 + 3a) \right] \quad (A.4)$$

or extend it further to a PV module with four cells connected in series [39],

$$ST_{(i,c=4)} = \left(\frac{1}{4 \times P_{cell}} \right) \left(\frac{1}{i^4} \right) P_{cell} \left[\sum_{k=1}^j \left(\frac{4}{j} \right) k + \sum_{a=1}^{j-1} 4 \left(\frac{j-a}{j} \right) (4a^3 + 6a^2 + 4a) \right] \quad (A.5)$$

Hence, considering equations A.3 - A.5, a general equation with the number of cells as a parameter can be derived as [39],

$$ST_{(i,c)} = \left(\frac{1}{n} \right) \left(\frac{1}{i^n} \right) \left[\sum_{k=1}^j \left(\frac{n}{j} \right) k + \sum_{a=1}^{j-1} n \left(\frac{j-a}{j} \right) \sum_{b=1}^{n-1} \binom{n}{b} a^{n-b} \right] \quad (A.6)$$

where n is the number of cells connected in series and the PV module consists of only one string of series connected cells. Now, the above equation can be extended for a PV module with more than one string by considering m number of parallel strings ($c = n \times m$). Since, the expected value of m identical probability trials is equal to m times the expected value of each trial, the general equation for ST is obtained as [39],

$$ST_{(i,c)} = \left(\frac{m}{n \times m} \right) \left(\frac{1}{i^n} \right) \left[\sum_{k=1}^j \left(\frac{n}{j} \right) k + \sum_{a=1}^{j-1} n \left(\frac{j-a}{j} \right) \sum_{b=1}^{n-1} \binom{n}{b} a^{n-b} \right] \quad (A.7)$$

Substituting $n \times m$ by c in equation A.7, the general equation for ST can be re-written as,

$$ST_{(i,c)} = \left(\frac{m}{c} \right) \left(\frac{1}{i^n} \right) \left[\sum_{k=1}^j \left(\frac{n}{j} \right) k + \sum_{a=1}^{j-1} n \left(\frac{j-a}{j} \right) \sum_{b=1}^{n-1} \binom{n}{b} a^{n-b} \right] \quad (A.8)$$

B

Decomposition Models

In each of the irradiance decomposition models discussed in chapter 5, the diffuse fraction (k_d) is first determined using piecewise correlations or logistic functions. The DHI can then be obtained as,

$$DHI = k_d \times GHI \quad (B.1)$$

The DNI can then be easily estimated using equation B.2.

$$DNI = \frac{GHI - DHI}{\cos(\theta_z)} \quad (B.2)$$

Erbs Model:

The Erbs model was developed using DNI and GHI data from five stations in the USA [77]. The model uses piecewise correlation with higher order polynomials to estimate the diffuse fraction from the clearness index (k_t) [77].

$$k_d = \begin{cases} 1 - 0.09k_t & k_t \leq 0.22 \\ 0.9511 - 0.1604k_t + 4.39(k_t)^2 - 16.64(k_t)^3 + 12.34(k_t)^4 & 0.22 < k_t \leq 0.8 \\ 0.165 & k_t > 0.8 \end{cases} \quad (B.3)$$

Reindl Model:

Reindl et al. had studied measured data from six locations in the USA and Europe [74]. They had determined several predictor variables that may affect the diffuse fraction and introduced three different models using the most influential predictor variables. The first model expresses the diffuse fraction as a function of the clearness index only whereas the second model includes the Sun altitude in addition to it. The third model uses two more predictor variables namely, ambient temperature (T_a) and relative humidity (RH). In this thesis, only the second and third models introduced by *Reindl et al.* were evaluated and the piecewise correlations used are as follows [74],

(a) Reindl-2 Model:

$$k_d = \begin{cases} 1.020 - 0.254k_t + 0.0123 \sin(a_S) & k_t \leq 0.3, k_d \leq 1.0 \\ 1.400 - 1.749k_t + 0.177 \sin(a_S) & 0.3 < k_t < 0.78 \\ 0.486k_t - 0.182 \sin(a_S) & k_t \geq 0.78, k_d \geq 0.1 \end{cases} \quad (B.4)$$

(b) Reindl-3 Model:

$$k_d = \begin{cases} 1.000 - 0.232k_t + 0.0239 \sin(a_S) - 0.000682 T_a + 0.019 RH & k_t \leq 0.3, k_d \leq 1.0 \\ 1.329 - 1.716k_t + 0.267 \sin(a_S) - 0.00357 T_a + 0.106 RH & 0.3 < k_t < 0.78, k_d \geq 0.1 \\ 0.426k_t - 0.256 \sin(a_S) + 0.00349 T_a + 0.0734 RH & k_t \geq 0.78, k_d \geq 0.1 \end{cases} \quad (B.5)$$

Dutch Model:

Jamodkar had developed two different decomposition models based on measured data from CESAR, Cabauw, The Netherlands [83]. The models use greater number of piecewise intervals than the models discussed earlier. Both models use the clearness index and solar zenith angle (θ_z) as the predictor variables. The first model uses linear correlations whereas the second model uses quadratic correlations [83].

(a) Dutch-I Model:

$$k_d = c_1 + c_2 k_t + c_3 \cos(\theta_z) \quad (\text{B.6})$$

Table B.1: List of coefficients for Dutch I model.

Range of clearness index	c_1	c_2	c_3
$k_t \leq 0.30$	0.99	-0.09	0.01
$0.30 < k_t \leq 0.40$	1.14	-0.67	0.07
$0.40 < k_t \leq 0.50$	1.54	-1.79	0.18
$0.50 < k_t \leq 0.60$	1.65	-2.04	0.23
$0.60 < k_t \leq 0.75$	1.49	-1.76	0.12
$0.75 < k_t \leq 0.80$	-0.17	0.81	-0.32
$k_t > 0.80$	0.00	0.69	-0.35

(b) Dutch-II Model:

$$k_d = f_1 + f_2 k_t + f_3 \cos(\theta_z) + f_4 k_t \cos(\theta_z) + f_5 (k_t)^2 + f_6 \cos(\theta_z)^2 \quad (\text{B.7})$$

Table B.2: List of coefficients for Dutch II model.

Range of clearness index	f_1	f_2	f_3	f_4	f_5	f_6
$k_t \leq 0.30$	1.00	-0.02	-0.02	0.08	-0.06	-0.01
$0.30 < k_t \leq 0.40$	0.93	0.37	0.05	-0.08	-0.61	-0.04
$0.40 < k_t \leq 0.50$	1.36	-0.16	-0.53	1.96	-2.76	-0.17
$0.50 < k_t \leq 0.60$	2.36	-4.63	0.07	-0.69	2.56	0.67
$0.60 < k_t \leq 0.75$	2.75	-7.75	3.03	-6.20	6.60	1.41
$0.75 < k_t \leq 0.80$	12.57	-31.99	-0.65	-1.45	21.68	1.25
$k_t > 0.80$	-2.45	6.97	-1.81	0.76	-3.79	0.73

C

Glossary

C.1. Acronyms

AC	Alternating Current
AST	Apparent Solar Time
BIPV	Building Integrated Photovoltaic
BSRN	Baseline Surface Radiation Network
CBS	Cool Bypass Switch
CESAR	Cabauw Experimental Site for Atmospheric Research
CIGS	Cadmium Indium Gallium Selenide
CRSS	Composite Residual Sum of Squares
DC	Direct Current
DHI	Diffuse Horizontal Irradiance
DISC	Direct Insolation Simulation Code
DNI	Direct Normal Irradiance
DWD	Deutscher Wetterdienst
EPBT	Energy Payback Time
EROI	Energy Return On Energy Invested
FF	Fill Factor
GHI	Global Horizontal Irradiance
GMST	Greenwich Mean Sidereal Time
IDW	Inverse Distance Weighted
IEA	International Energy Agency
IEC	International Electrotechnical Commission
LASS	Large Area Steady State Solar Simulator
LCOE	Levelized Cost Of Electricity
LSVM	Linear Support Vector Machine
KMI	Koninklijk Meteorologisch Instituut van België

KNMI	Koninklijk Nederlands Meteorologisch Instituut
MAPE	Mean Absolute Percentage Error
MBD	Mean Bias Difference
MPP	Maximum Power Point
MPPT	Maximum Power Point Tracking
MLR	Multiple Linear Regression
O&M	Operation & Maintenance
OC	Open Circuit
OK	Ordinary Kriging
POA	Plane Of Array
PR	Performance Ratio
PTC	Positive Temperature Coefficient
PV	Photovoltaic
PVMD	Photovoltaic Material and Devices
PVPS	Photovoltaic Power System
RD	Relative Difference
RMSE	Root Mean Square Error
SC	Short Circuit
SF	Shading Factor
SK	Simple Kriging
SR	Soiling Ratio
ST	Shading Tolerability
STC	Standard Test Condition
SVF	Sky View Factor
TLR	Temperature Lapse Rate
TST	True Solar Time
UTC	Coordinated Universal Time
UTS	Universal Thermal Scale
WCRP	World Climate Research Programme
WGS84	World Geodetic System 1984

C.2. List of Symbols

α	Temperature coefficient for short-circuit current
β	Temperature coefficient for open-circuit voltage
γ	Temperature coefficient for maximum power
V_{oc}	Open-circuit voltage
I_{sc}	Short-circuit current

P_{MPP}	Maximum power
J_0	Saturation current density
E_g	Bandgap
J_{SC}	Short-circuit current density
ϕ_0	Latitude of observer
λ_0	Longitude of observer
θ_z	Solar zenith angle
α_S	Altitude of the Sun
A_S	Azimuth of the Sun
k_t	Clearness index
k_d	Diffuse fraction
ψ	Persistence
K_t	Daily clearness index
Y_f	Final PV system yield
Y_r	Reference yield
β_M	Tilt angle of PV module
I_b	Direct horizontal irradiance
ρ	Albedo

Abstract Number: 723
Last Modified: January 22 2018

Submitted By: Hesam Ziar

The Need for a New Parameter on PV Modules Datasheet: Shading Tolerability

Hesam Ziar, Sandeep Mishra, Olindo Isabella, Miro Zeman

Delft University of Technology, Delft, Netherlands

Applications of PV modules are increasing sharply in urban areas. The tremendous increase of Building Integrated PV (BIPV) systems and solar roads makes it practically impossible to eliminate the source of static shading (buildings, trees, etc.). Besides, there will always be dynamic shading (clouds, birds, etc.). In this context, the proper selection of PV modules is of dominant importance in the PV system design. The right choice is made more challenging when the location of the installation is prone to shading. In modules datasheet, the ability of the modules to oppose shading effects is normally expressed qualitatively. General statements such as: *better shading response, outstanding low light behavior, patented bypass circuit, and shade tolerant* may not help the designer to select the most suitable module for a specific location. On the other hand, a quantified parameter, a number, which classifies PV modules in terms of shading tolerability, can be more meaningful. This research work, suggests a measurable parameter, the so-called Shading Tolerability (ST), to be added on PV modules datasheet. The parameter is extracted based on mathematical and probability analysis, then measured using a Large Area Steady State Solar (LASSS) simulator. Outdoor measurements proved a correlation between ST and Performance Ratio (PR) of PV modules.

For each tested PV module, ST was determined in less than 6 hours. Consequently, it is industrially feasible to perform ST test on a single or couple of modules which are randomly selected from an identical group of modules. In this way, for a small amount of energy consumed within six hours, a huge extra energy will be extracted from the sun during the PV system lifetime by selecting correct PV modules. Therefore, it is suggested to add ST on photovoltaic modules datasheet as a benchmark to distinguish and classify PV modules regarding shading tolerability.

Area: Sub-Area 8.1: Module Materials, Design, Manufacture, and Production

The Need for a New Parameter on PV Modules Datasheet: Shading Tolerability

Hesan Ziar, Sandeep Mishra, Olindo Isabella, and Miro Zeman

Delft University of Technology, PVMD Laboratory, EKL, P.O. Box 5053, 2600 GB Delft, the Netherlands
(Contacts: h.ziar@tudelft.nl, o.isabella@tudelft.nl)

Abstract — This paper suggests a measurable parameter, the so-called Shading Tolerability (ST), to be added on PV modules datasheet. Using this parameter, PV modules can be compared and classified regarding the ability to oppose shading effects. The parameter is extracted based on mathematical and probability analysis, then measured using a Large Area Steady State Solar (LASSS) simulator. Outdoor measurements proved a correlation between ST and Performance Ratio (PR) of PV modules.

I. INTRODUCTION

As the goal of the PV industry is to push forward the mindset of the energy society to the concept of “PV everywhere” [1], PV modules are going to be installed more and more in urban areas. In such a situation, PV modules will be more frequently subjected to shades projected by any possible object such as side trees, chimneys, flying birds, and of course there always be clouds moving above. How can a PV designer or installer company distinguish the better performing PV module under non-uniform irradiation condition?

Most PV module manufacturer claim the superior performance of their products in shading condition by qualitative terms. Terms such as: better shading response [2], outstanding low light behavior [3], etc., are being used in PV modules datasheet. However, these general qualitative terms may not help the designer or installer to select the most suitable module for a specific location. On the other hand, a quantified parameter, a number, which classifies PV modules in terms of shading tolerability (ST), can be more meaningful. Therefore, the authors believe that there is a need for a new parameter on PV modules datasheet to address this issue. The establishment of such a parameter is the goal of this contribution.

II. THEORETICAL DEFINITION OF SHADING TOLERABILITY

Although there has been decades of research on PV systems [4], random nature of shading profile on PV systems, has been the major obstacle in quantification of shading tolerability. Therefore, in a framework of probability laws, the following formula is suggested for PV module shading tolerability [5]:

$$ST_{(i,c)} = \frac{1}{P_{mod_mpp}} \sum_{k=1}^{k=i^c} P_k \left(\frac{1}{i^c} \right) \quad (1)$$

where $ST_{(i,c)}$ stands for shading tolerability. c and i are the total number of PV cells (within the module) and irradiation levels, respectively. P_k corresponds to the MPP at each shading profile (in W), while P_{mod_mpp} is the maximum power of PV module (in W). P_{mod_mpp} normalizes the value of mathematical expectation and makes it possible to compare PV modules with different rated powers. Mathematically, the PV module which gains higher value from (1), acts better at shading.

One of the remarkable outcomes of this analysis is that ST of a PV module is inversely proportional to the factor of $(n+1)$, where n is the number of series connected PV cells in a module. Besides, the shading vulnerability is independent from number of PV cell parallel strings within the module. Results can also be extended to array level.

III. EXPERIMENTAL RESULTS

To evaluate our theoretical study, long-term experiments were accomplished in two sections, indoors and outdoors. To cover a wide range of PV markets, various PV modules were selected and tested indoor using an EternalSun Large Area Steady State Solar (LASSS) AAA-class simulator. As shown in Fig. 1, each module was tested under 64 shading profiles. Studies proved that these 64 shading profiles are decent representatives of all possible shading conditions. Thirteen PV modules have been tested so far in the PVMD laboratory. Table I shows the results of indoor test and corresponding measured ST values and suggested shading classes. Results also showed that the number of bypass diodes, cells size and shape, and technology of a module are not always a valid measure for shading tolerability comparison.

PV modules #3, #6, and #10 from Table I were evaluated outdoor (different ST classes). Modules were separated into two identical groups and installed on two locations as close as possible. One location was mostly sunny during day-time while the other one was frequently shaded by side objects. Performance Ratio (PR) of the modules were measured for 12 days. Results showed that modules which had performed better at indoor ST test kept on providing higher output at on-field outdoor measurements. Moreover, the ratio of differences of the measured outdoor PR values are surprisingly close to the ratio of differences of the obtained indoor ST values.

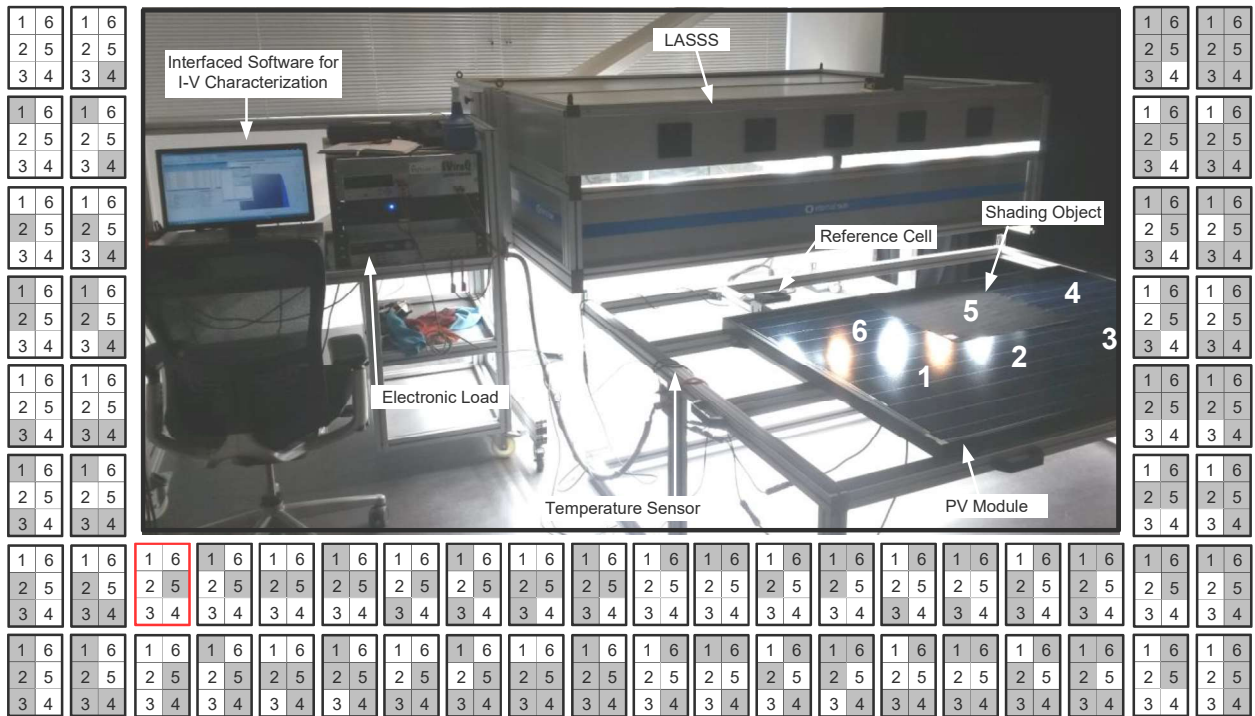


Fig. 1. Indoor experimental setup for testing shading tolerability along with 64 shading profile codes from 000000 to 111111. The depicted module under test (#4, see Table I) has 54 cells and is divided into 6 sections. The 010000 shading profile code is shown in the picture. In this respect, sections 1, 2, 3, 4, and 6 are about to receive rated irradiation (1000 W/m^2) while section 5 is shaded and receives 250 W/m^2 . The shading object for this specific module shades simultaneously 9 cells [5].

III. DISCUSSION ON THE SIGNIFICANCE OF THE SHADING TOLERABILITY PARAMETER

The defined shading tolerability, ST could be very useful in PV engineering. The previously published paper of the authors [5], theoretically and experimentally proved that the indoor measurement of ST is enough to know and compare the performance of modules in outdoor shading conditions. Therefore, the randomness of the shade and its profiles is not an issue anymore and module manufacturers can have their modules tested using this explained measurement procedure. For each tested PV module, shading tolerability was determined in less than 6 hours. Consequently, it is industrially feasible to perform ST test on a single or couple of modules which are randomly selected from an identical group of modules. In this way, for a small amount of energy consumed within six hours, a huge extra energy will be extracted from the sun during the PV system lifetime by selecting correct PV modules. Therefore, it is suggested to add ST on photovoltaic modules datasheet as a benchmark to distinguish PV modules regarding shading tolerability.

Also it has been mathematically and experimentally proven that the new defined parameter, ST, is independent from measurement temperature. In other words, ST and temperature coefficient (T_C) are independent and this makes it possible to categorize PV modules in a ST- T_C map for appropriate selection. ST, together with T_C of the PV modules, will significantly help the designer to select the best module for different installation locations.

IV. SUMMARY

PV modules are being installed everywhere and are prone to shading more frequently. Currently, there is no quantitative way to compare PV modules in terms of shading tolerability. Therefore, the authors suggest ST which is a new measurable parameter for photovoltaic modules datasheet and has the potential to be industrially applicable. Using this parameter, PV modules can be compared and rated based on their performance at shading.

DISCLAIMER

Results presented in this work strictly concern the individual photovoltaic modules available and tested in the PV Laboratory of the PVMD group of TU Delft. The performance of such modules might not reflect that of similar or updated modules from the same brand and/or under different circumstances.

REFERENCES

- [1] A. Smets, Closing session speech at EUPVSEC, Amsterdam, the Netherlands, 2017.
- [2] "First solar technology advantage brochure," First Solar, Tempe, AZ, USA, 2015, pp. 1–7.
- [3] "Multisol P6-54 series datasheet," Scheuten, The Netherlands, 2010, pp. 1–2.
- [4] G.K. Singh, "Solar power generation by PV (photovoltaic) technology: A review," *Energy*, 53 pp. 1-13, 2013.
- [5] H. Ziar, et. al., "Quantification of Shading Tolerability for Photovoltaic Modules." *IEEE J. Photovolt.*, vol. 7, no. 5, pp. 1390–1399, Sep. 2017.

TABLE I
DETAILED SPECIFICATION OF TESTED PV MODULES AND CORRESPONDING MEASUREMENT RESULTS

	Company/ Commercial Name	Technology	Electrical specification	Mechanical size Weight Flexibility	Notes on module's datasheet regarding shading tolerance	Measured <i>ST</i> ^(#)	Percentage value of <i>ST</i> ^(#)	Suggested Shading Class Symbol
1	Neste Module PV A12	a-Si	MPP=7.5 W Voc=22 V Vmpp=15 V Isc=0.6 A Impp=0.5 A Bypass diodes: None Total 29 cells-one string	614×309×22 mm ³ 3.0 kg (Rigid)	None	0.36	58%	 Partly-cloudy
2	Victron Energy SPM30-12	Mono c-Si	MPP= 30 W Voc= 22.5 V Vmpp= 18 V Isc=2 A Impp=1.67 A Bypass: One silicon p-n diode Total 36 cells-one string	450×540×25 mm ³ 2.5 kg (Rigid)	None	0.24	38%	 Sunny
3	Würth Solar GeneCIS module 80W	CIS	MPP=80 W Voc=44 V Vmpp=35 V Isc=2.5 A Impp=2.29 A Bypass: One silicon p-n diode Total 132 cells- two parallel strings	605×1205×35 mm ³ 12.7 kg (Rigid)	<i>Optimum energy yield through outstanding temperature and low light behavior</i>	0.57	91%	 Cloudy
4	Scheuten Multisol P6-54 series 200	Poly c-Si	MPP=200 W Voc=33 V Vmpp=25.9 V Isc=8.22 A Impp=7.71 A Bypass: Three Schottky diodes Total 54 cells-one string	1500×1000×42 mm ³ 20.0 kg (Rigid)	<i>Junction box with patented connection system and 3 bypass diodes</i>	0.22	35%	 Sunny
5	Calyxo CX3-77 Thin film solar module	CdTe/CdS	MPP=77.5 W Voc=62.5 V Vmpp=46.7 V Isc=1.98 A Impp=1.68 A Bypass diodes: None Total 156 cells-two parallel strings	1200×600×6.9 mm ³ 12.0 kg (Rigid)	None	0.39	63%	 Partly-cloudy
6	SunPower SPR X20 327-BLK	Mono c-Si	MPP=327 W Voc=67.6 V Vmpp=57.3 V Isc=6.07 A Impp=5.71 A Bypass: Three silicon p-n diodes Total 96 cells-one string	1559×1046×46 mm ³ 18.6 kg (Rigid)	<i>Designed to deliver the most energy in partial shade and hot rooftop temperatures</i>	0.21	33%	 Sunny
7	Masdar PV MPV-T	Tandem a-Si/a-Si	MPP=109.81 W Voc=137.54 V Vmpp=107.03 V Isc=1.21 A Impp=1.02 A Bypass: One silicon p-n diode Total 636 cells-three parallel strings	1300×100×7 mm ³ 29.5 kg (Rigid)	<i>Excellent energy output even during diffuse or low light conditions</i>	0.25	40%	 Sunny
8	IKS Photovoltaik STA14 10W SolarTrainer	Poly c-Si	MPP=10 W Voc=22 V Vmpp=17 V Isc=0.72 A Impp=0.52 A Bypass: One silicon p-n diode Total 36 cells-one string	345×294×23 mm ³ Not specified (Rigid)	None	0.25	40%	 Sunny
9	Solland SunWeb module 235 W _p	Poly c-Si	MPP=235 W Voc=36.97 V Vmpp=30.05 V Isc=8.44 A Impp=7.82 A Bypass: Three Schottky diodes Total 60 cells- one string	1613×984×35 mm ³ 22 kg (Rigid)	None	0.24	39%	 Sunny
10	Hanergy PowerFlex 90W	CIGS	MPP=90 W Voc=22 V Vmpp=16.5 V Isc=6.3 A Impp=5.4 A Bypass: Diodes at each cell; one at j- box. Total 36 cells-one string	2017×494×3 mm ³ 3.3 kg (Flexible)	<i>Shade tolerant</i>	0.31	50%	 Partly-cloudy
11	Uni-Solar PowerBond ePVL	Multi- junction a- Si	MPP=27.4 W Voc=10.44 V Vmpp=7.8 V Isc=4.28 A Impp=3.52 A Bypass: Diodes at each cell Total 5 cells-one string	1325×373×3 mm ³ 1.8kg (Flexible)	<i>Excellent performance even when partially shaded</i>	0.37	59%	 Partly-cloudy
12	BenQ SunForte PM096B00-335	Mono c-Si	MPP=335 W Voc=64.9 V Vmpp=54.7 V Isc=6.62 A Impp=6.13 A Bypass: Three diodes Total 96 cells-one string	1559×1046×46 mm ³ 18.6 kg Rigid	None	0.30	49%	 Sunny
13	AERspire Deluxe 60	Mono c-Si	MPP=250 W Voc=38.3 V Vmpp=30.8 V Isc=8.62 A Impp=8.08 A Bypass: Three diodes Total 60 cells-one string	1720×1035×40 mm ³ 24 kg Rigid	None	0.30	48%	 Sunny

(#) *ST* and %*ST* values are rounded to the closest integer. To obtain %*ST*, defined as the percentage value of *ST*, measured *ST* is divided by the maximum theoretical value of *ST* (for the measurement criteria).